

Diese Dissertation haben begutachtet:

Dr. Catalina Oana Curceanu

Prof. Dr. Peter Krizan

DISSERTATION

**Optimization Studies and Performance Simulations
for the Time-of-Flight System of PANDA**

Ausgeführt zum Zwecke der Erlangung des akademischen Grades eines Doktors der
technischen Wissenschaften unter Leitung von

Priv.-Doz. Dr. Johann Marton

Stefan-Meyer-Institut für subatomare Physik
der Österreichischen Akademie der Wissenschaften
und Atominstitut der Technischen Universität Wien

eingereicht an der Technischen Universität Wien Fakultät für Physik

von

Dipl.Ing. Dominik Steinschaden

Matr.-Nr. 00627761 Guntherstraße 13/17, 1150 Wien

Ort, Datum

Unterschrift

Kurzfassung

Das $\bar{\text{PANDA}}$ Experiment befindet sich aktuell in der Planungs- und Konstruktionsphase und wird als Teil der “Facility for Antiproton and Ion Research” (FAIR) in Darmstadt, Deutschland errichtet. Das Ziel des Experiments ist die Erforschung grundlegender, offener Fragen in der Teilchen-, Hadronen- und Nuklearphysik über die Wechselwirkung von Antiprotonen mit Atomkernen. Dafür liefert der “High Energy Storage Ring” einen Antiprotonenstrahl mit einem Impuls zwischen 1.5 – 15 GeV/c, welcher mit einer durchschnittlichen Kollisionsrate von 20 MHz mit dem feststehenden “Target” im Experiment wechselwirkt. Diese hohe Ereignisrate macht eine Reduktion des gemessenen Datenvolumens vor dem Speichern um das 100 – 1000-fache notwendig. Da das $\bar{\text{PANDA}}$ Experiment dafür keinen herkömmlichen Hardwaretrigger verwendet, sondern die Daten ungefiltert und kontinuierlich auslesen wird, ist eine spezialisierte und fortschrittliche Analyseverfahren notwendig, welche direkt und schnell über den Wert der aktuell gemessenen Daten entscheidet. Das Fehlen eines dedizierten Ereignisstartzeitdetektors (t_0), die hohe Interaktionsrate, und die Signale und Daten der einzelnen Ereignisse, welche sich in den Detektorsystemen zum Teil zeitlich und räumlich überlappen, erschweren die Aufgabe dieses Selektionsalgorithmus weiter.

Der Barrel Time-of-Flight Detektor (Barrel TOF) von $\bar{\text{PANDA}}$ wird in Wien am Stefan-Meyer-Institut entwickelt. Er ist einer der Schlüsseldetektoren um den zeitlichen Ursprung von gemessenen Teilchen, Spuren und Signalen zu bestimmen. Dies ermöglicht eine Zuordnung der jeweiligen Signale zu den einzelnen Ereignissen und eine Bestimmung der Kollisionszeiten t_0 von Antiproton und Target. Des Weiteren spielt der Barrel TOF eine wichtige Rolle in der genauen Identifizierung der gemessenen Teilchenart und ergänzt hierbei die Informationen des Cherenkov Detektors, speziell für Teilchen mit Impulsen unter dessen Einsatzbereich von ca. 700MeV/c. Um all diese Aufgaben zu erfüllen ist eine Zeitauflösung des Detektorsystems von unter 100 ps notwendig. Dies wird durch eine Ausführung als szintillatorbasiertes Hodoskop erreicht, welches im Zentrum des Experiments installiert wird. Der Barrel TOF hat einen Durchmesser von 1 m, eine Länge von 2 m und eine sensitive Fläche von 6 m². Er besteht aus 1920 einzelnen Szintillatoren mit einer Größe von ca. 90 × 30 × 5 mm³, welche jeweils von 8 Silicon

Photomultipliers (SiPMs), 4 pro Ende, ausgelesen werden. Die Signalübertragung erfolgt über eine PCB Platte, welche gleichzeitig den mechanischen Rahmen für die Installation bildet, um das Materialbudget möglichst gering zu halten. Während Teststrahlzeiten wurden mit ersten Prototypen bereits Zeitauflösungen um die 55 ps erreicht.

Eine wichtige Aufgabe war die Implementierung des Barrel TOF in das Simulationssystem von $\bar{\text{PANDA}}$, PandaRoot. Dies ermöglichte die Optimierung der Detektorgeometrie basierend auf Monte Carlo Simulationen sowie eine Bestimmung der Anforderungen an die Ausleseelektronik. Dies bestärkte unter anderem das finale Detektordesign, beschrieben in dieser Arbeit. Anschließend wurde der Einfluss und die Leistung des Barrel TOF für das $\bar{\text{PANDA}}$ Experiment in zahlreichen Simulationen bestimmt und optimiert. Algorithmen basierend auf dem Barrel TOF bzw. dessen gemessenen Daten wurden entwickelt und in PandaRoot implementiert, z.B. für die Ereignistriggerung, Daten- und Ereignissortierung, Startzeitrekonstruktion und Teilchenidentifizierung. Unter anderem ermöglichte diese Arbeit die Fertigstellung und Einreichung des “Technical Design Report” für den Barrel TOF. Dieser wurde im Februar 2017 an FAIR Council übermittelt und akzeptiert. In der Zwischenzeit wurden die entwickelten und eingebauten Algorithmen sowie das gesammelte Wissen und die Erfahrung genutzt um die Online-Datenrekonstruktion von $\bar{\text{PANDA}}$ weiter zu entwickeln. Gemeinsam mit internationalen Kollegen wurden erste Versionen und Tests eines “dynamical tracking and event reconstruction” Algorithmus realisiert, welcher die Signale mehrere $\bar{\text{PANDA}}$ -Detektorsysteme kombiniert.

Abstract

The $\bar{\text{P}}\text{ANDA}$ experiment, currently under construction at the Facility for Antiproton and Ion Research (FAIR) in Darmstadt, Germany, addresses fundamental questions in hadron and nuclear physics via interactions of antiprotons with nucleus / nuclei. The High Energy Storage Ring will provide an antiproton beam with a momentum range of 1.5 – 15 GeV/c and an average collision rate of 20 MHz on a fixed target. Due to a missing hardware trigger and a continuous data acquisition in the $\bar{\text{P}}\text{ANDA}$ experiment, a highly advanced online analysis is needed to achieve an online data reduction of a factor 100 – 1000 before storage. A missing collision time (t_0), high interaction rates and overlapping event data in the sub detector systems further increases the difficulty of the event reconstruction.

The Barrel Time-of-Flight detector (Barrel TOF) for $\bar{\text{P}}\text{ANDA}$, being developed at the Stefan Meyer Institute, will be one of the key components in $\bar{\text{P}}\text{ANDA}$ to determine the origin time of particle tracks, to ensure a disentanglement of overlapped hits from neighbouring collisions and to provide information about t_0 . Another important task of the Barrel TOF is to provide particle identification (PID) for charged particles together with the Cherenkov-based PID detectors, which is especially important for particle momenta below 700 MeV. In order to achieve a time resolution of < 100 ps, required for the mentioned disentanglement of the data, while keeping a minimal material budget, the detector will be realized as a barrel-shaped scintillator tile hodoscope. It covers the central region of the detector with a diameter of about 1 m and a length of about 2 m. The sensitive area of about 6 m² consists of 1920 scintillating tiles with a dimension of $90 \times 30 \times 5$ mm³ each, readout by 8 Silicon Photomultipliers (SiPMs), with 4 on each end connected in series. The signal transmission lines are embedded in a multilayer PCB backplane. It also serves as the mechanical frame to minimize the material budget. During beam tests a single tile time resolution of $\sigma = 55$ ps has been achieved.

It was a crucial and challenging task to implement the Barrel TOF in the simulation framework, PandaRoot. This allowed the optimization of the detector geometry using Monte Carlo simulations and the investigation of the requirements for the readout electronics and led to the described design. In the second phase

the performance of the Barrel TOF was evaluated and optimized for the entire experiment. For this purpose software algorithms based on the Barrel TOF system were developed and implemented in PandaRoot, i.e. triggering, event sorting, start time reconstruction and particle identification. Among other work this allowed the submission of the Technical Design Report for the Barrel TOF in February 2017 to FAIR, which has been accepted. After this the developed and implemented algorithms as well as the acquired knowledge were used to advance the general PANDA reconstruction chain. Together with our international collaborators the first steps towards a dynamical tracking and event reconstruction algorithm, which combines the signal of all sub detector systems of $\bar{\text{PANDA}}$, were developed.

Acknowledgement

I want to thank my supervisor Dr. Johann Marton for giving me the opportunity to do my PhD at the Stefan Meyer Institute. He supported me not only during my scientific work, but also helped with the organization of conferences participations, introduced me to interesting research groups and supported me to find for my future way in science. I also want to thank Dr. Catalina Oana Curceanu and Prof. Dr. Peter Krizan for reviewing this thesis and participating in the final examination. I also acknowledge the funding of the Austrian Science Fund FWF under the Doctoral Program W1252-N27 Particles and Interactions.

I express a great thankfulness to Dr. Ken Suzuki, who was not only my group leader, but became also a second supervisor. He was not only enthusiastic about guiding me to good research results but also took care about my creature comforts. Exploring various excellent restaurants in various cities and countries together was always one of the highlights abroad! Many thanks also for his careful and repeatedly prove reading of various documents including this thesis.

A special thanks goes to my colleagues Sebastian, Andreas, Manfred and Bernadette with whom i could not only discuss work related topics for hours and ask for help at any point, but who were willing to discuss on any topic especially in myriads of lunch breaks, during traveling, and various evenings and nights. I also want to thank all my other colleagues for enabling the common Nintendo 64 evenings and other activities, which I always enjoyed a lot! At that point I also want to thank Julia, Peter and all the other staff members, who helped me a lot during the last years.

I was fortunate to have also great colleagues abroad i.e Karin, Michael, Walter, Jenny . . . , who supported not only my work during a research stay in Sweden and above, but also become good friends. Here I also want to note Aila, Stefan and Sabrina, who spent a lot of time to support my family during that time.

Last but not least I want to thank my wife, Iris. She was not only very patient and sympathetic when I wanted to talk about work, had to stay longer at the institute or went abroad for a conference. She took care of our two children, Kilian and

Arthur, who were born both in these years and supported my career in every situation. And she still found enough reserves to organize wonderful holidays, entertaining card and board game evenings, or just relaxing family time!
I love you.

Contents

Kurzfassung

Abstract

Acknowledgement

1	Introduction	1
2	The $\bar{\text{PANDA}}$ Experiment	5
2.1	Physics Program	5
2.1.1	Hadron Spectroscopy	6
2.1.2	Electromagnetic Form Factors in the Time-like Region	6
2.1.3	Hadrons in Matter	6
2.1.4	Hypernuclei	7
2.2	Facility for Antiproton and Ion Research	7
2.2.1	Main Experiments at FAIR	7
2.2.2	High Energy Storage Ring	9
2.3	The $\bar{\text{PANDA}}$ Spectrometer	10
2.3.1	Target System	11
2.3.2	Magnet System	13
2.3.3	Tracking Detectors	14
2.3.4	Particle Identification	16
2.3.5	Electromagnetic Calorimetry	20
2.3.6	Luminosity Detector	20
2.3.7	Hypernuclear Detector Extension	21
2.3.8	DAQ	21
3	PandaRoot	23
3.1	Root	23
3.2	FairRoot	25
3.3	PandaRoot	25
3.3.1	Generators	26
3.3.2	Detector Simulation	27

3.3.3	Digitization	28
3.3.4	Reconstruction	29
3.3.5	PID	29
3.4	Analysis	30
4	PANDA Barrel Time-of-Flight detector	31
4.1	Capabilities	32
4.1.1	Particle Identification	32
4.1.2	Software Trigger	33
4.1.3	Event Sorting	33
4.1.4	Pattern Matching	34
4.1.5	EMC Preshower Detection	35
4.2	Requirements	36
4.2.1	Time Resolution	36
4.2.2	Position Resolution	37
4.2.3	Mechanical Requirements	38
4.3	Design	38
5	Barrel TOF optimization studies	43
5.1	Implementation of the Barrel TOF	43
5.2	Barrel TOF efficiency studies	50
5.2.1	Geometrical Efficiency	50
5.2.2	DAQ Efficiency	52
5.2.3	Combined Efficiency	55
6	Barrel TOF performance simulations	59
6.1	Event Building	59
6.1.1	Event Structure	61
6.1.2	Event Determination Algorithm	69
6.1.3	Performance Study	73
6.1.4	Ghost Reduction	74
6.1.5	Summary	76
6.2	T_0 Reconstruction	77
6.2.1	Typical Time-of-Flight	78
6.2.2	Suppressing Slow Particles	80
6.2.3	T_0 Reconstruction Performance	82
6.2.4	Conclusion	85
6.3	Relative Time-of-Flight	87
6.3.1	Relative Time-of-Flight Algorithm	87
6.3.2	Relative Time-of-Flight Performance	89
6.3.3	Algorithm Enhancements	91

6.3.4	Relative Time-of-Flight Based PID	92
6.4	TOF based particle identification (PID)	93
6.4.1	Basic concept	93
6.4.2	Time-of-Flight Resolution	94
6.4.3	TOF Separation Power	100
7	Time Based Event Reconstruction	103
7.1	Preparation	103
7.1.1	PndBranchBurstBuilder	104
7.1.2	STTCellTrackFinder	105
7.2	First Time Based Track Reconstruction	106
8	Summary and Outlook	111
	List of Tables	i
	List of Figures	iii
	Bibliography	v
	Curriculum vitae	ix

1 Introduction

The standard model, whose last missing piece - Brout-Englert-Higgs boson - has been discovered in 2012, is one of the most precisely and thoroughly tested theory. New experiments were built and are still being built to search for a tiny crack of the standard model (Beyond Standard Model = BSM) without apparent success.

Computer simulations nowadays play an indispensable role in the development of these new experiments, detector hardware and the reconstruction methods of experimental data. Due to the fast evolution of the available computing power, new experiments can perform more and more sophisticated processing, even on the raw data rate. Therefore new generation experiments in particle physics can achieve very high detection and reconstruction efficiencies, while at the same time increasing the luminosity in their detector systems to the cutting-edge.

One of such next generation experiments will be the $\bar{\text{P}}\text{ANDA}$ experiment which will be built at FAIR (cf. section 2.2). The $\bar{\text{P}}\text{ANDA}$ experiment will study $\bar{\text{p}}\text{p}$ and $\bar{\text{p}}$ -nucleus reactions to investigate topics including the weak and strong forces, exotic states of matter and the structure of hadrons. As distinguishing feature from other modern hadron physics experiments, which are using e^+e^- colliders, the $\bar{\text{P}}\text{ANDA}$ experiment will not be limited to initial spin-parities of $J^{PC} = 1^{--}$. Due to broad physics program of $\bar{\text{P}}\text{ANDA}$ and in order to maximize the detection rate of processes with expected low cross section $\bar{\text{P}}\text{ANDA}$ will perform a novel approach of data acquisition. Instead of a common hardware trigger a fully software based system is used. The signals of the detector will be continuously streamed to the processing computing nodes. Online reconstruction algorithms will provide the information on the event topology for a software filter, which decides on whether storing or discarding the data in a matter of μs to keep track with the average interaction rate of 20 MHz. An important piece for this kind of DAQ is a very precise time measurement to disentangle signals of overlapping events especially at high event rates. A key component for this task will be the Barrel Time-of-Flight detector, which is currently being developed by the Barrel-TOF group, an international collaboration. The Stefan-Meyer-Institute is the leading institute and is responsible for its R&D, construction and operation.

The objective of this work was the development and optimization of the mentioned Barrel Time-of-Flight detector for the $\overline{\text{PANDA}}$ experiment and the results became a part of the Technical Design Report for this system. The focus of my work was on the software development and implementation of this Barrel TOF system in the simulation framework of $\overline{\text{PANDA}}$, called PandaRoot. First various design options were simulated in order to determine their detection efficiencies. The final design was implemented in PandaRoot, including electronics behaviors as realistic as it is known at this stage of the development. Not only PID algorithms based on standard time-of-flight methods were implemented, but also novel algorithms were developed to deal with the specific detector setup of $\overline{\text{PANDA}}$, such as the missing start time detector. As mentioned the Barrel TOF will play an important role for the DAQ, which is a non-trivial task due to the continuous read out combined with the high luminosity of $\overline{\text{PANDA}}$ and the potential event mixing. Therefore a major objective was a proof of principle for a event determination and event sorting algorithms based on this detector. After the submission of the Technical Design Report in spring 2017, the focus moved to the online reconstruction of $\overline{\text{PANDA}}$. The work in this field was going beyond the scope of the Barrel TOF detector and included other subdetector systems as well as tracking and reconstruction algorithms, currently under development by the $\overline{\text{PANDA}}$ collaboration.

The work of this thesis is presented in the following way. In chapter 2 an overview of the $\overline{\text{PANDA}}$ experiment is presented. It starts with a selection of the planned diverse physics program of the experiment. After that the future FAIR facility, which will host the $\overline{\text{PANDA}}$ experiment is described. Beside the other main experiments at FAIR also the accelerator complex, important for $\overline{\text{PANDA}}$, are presented. The last section actually explains the planned $\overline{\text{PANDA}}$ spectrometer including the subdetector and the DAQ systems.

Chapter 3 presents the software framework of $\overline{\text{PANDA}}$ called PandaRoot. It starts with a short description of the frameworks it is based on, before the general work flow is discussed in detail. This includes not only the detector simulation but also the data reconstruction and finally the physics analysis which is completely included in the software and will be used in the same way on the real data, once these are available.

The Barrel Time-of-Flight detector, which was the main focus of this work is explained in chapter 4. Firstly a motivation for the detector is given and its demanded capabilities. Then the derived requirements for the detector performance and layout are discussed followed by the latest design of the detector. This design describes the status of the development at the end of my thesis. Also an intermediate design is briefly presented in chapter 5 and discussed in more detail

in [1].

The second part of the thesis focuses on the performed simulation studies and the developed new reconstruction algorithms which have been implemented in PandaRoot.

Chapter 5 describes the simulation studies in order to evaluate and optimize the detector design of the Barrel TOF. This includes the implementation of the sub-detector system in the overall software framework and studies on the detection and DAQ efficiency for possible detector layouts.

Chapter 6 discusses algorithms developed during this work for various reconstruction stages of the $\bar{\text{PANDA}}$ experiment with a strong focus on the Barrel TOF. Namely the performance of the developed event sorting, t_0 reconstruction and relative time-of-flight based PID algorithms were studied. Also the performance of a conventional time-of-flight based PID was investigated and is presented in the last section.

Chapter 7 describes the last part of my work which goes slightly beyond the Barrel TOF detector and was partly carried out at the Department of Physics and Astronomy of the Uppsala University. I performed the first track reconstruction on the continuous data stream of the $\bar{\text{PANDA}}$ experiment.

The last chapter 8 finally summarizes the results and presents a short outlook.

2 The $\bar{\text{P}}\text{ANDA}$ Experiment

The $\bar{\text{P}}\text{ANDA}$ experiment (Antiproton **A**nnihilation at **D**armstadt) will be one of the major experiments of the future international **F**acility for **A**ntiproton and **I**on **R**esearch (FAIR), currently under construction at Darmstadt, Germany. It will be located at the High Energy Storage Ring (HESR) and allow new access to fundamental questions of hadron and nuclear physics. The scientific program includes charmonium and open-charm spectroscopy, searches and investigations of exotic states, e.g. multi quark states, hybrids and glueballs, the study of modifications of hadrons in nuclear matter, hyperon physics and γ -ray spectroscopy of hypernuclei. To manage this challenging physics program, the experiment needs to record the tracks of all reaction products and their decay products. Therefore the $\bar{\text{P}}\text{ANDA}$ experiment covers the full solid angle and is capable of measuring the energy and momentum of all charged particles and photons as well as identifying all particle types over the full momentum range. The experiment will perform a trigger less continuous read-out. Total data rate from FEEs to Data Concentrator will reach data rates of about 200 GB/s. This DAQ provides the necessary flexibility for the complex physics program of $\bar{\text{P}}\text{ANDA}$, which will study a diverse range of channels with cross sections varying by many order of magnitudes.

2.1 Physics Program

A small overview about some physics disciplines researched by $\bar{\text{P}}\text{ANDA}$ are presented in the following section. However, the focus of this thesis was on hardware and software development, so a full, in-depth description of the planned physics program of $\bar{\text{P}}\text{ANDA}$ can be found in [2].

2.1.1 Hadron Spectroscopy

Modern hadron physics experiments mainly use e^+e^- interactions for the production of charmonium and open-charm states. Therefore these experiments are primarily restricted to initial spin-parities of $J^{PC} = 1^{--}$. Most of these accelerators are also optimized to certain initial resonances and have therefore a fixed energy. This limits the possibility to precisely scan and investigate resonances in formation reactions. The availability of $\bar{p}p$ annihilation with an adjustable primary momentum in the \bar{P} ANDA experiment overcomes these limitations.

Charmonium and Open Charm Spectroscopy

The high average luminosity of \bar{P} ANDA allows the production of several thousands of $c\bar{c}$ states per day. This gives the possibility to perform a fine scan on the resonances and achieve a precision in the order of 100 keV and below (cf. section 2.2.2). \bar{P} ANDA will explore the energy region below and above the open charm threshold, to study the underlying mechanisms.

2.1.2 Electromagnetic Form Factors in the Time-like Region

As part of the nucleon structure program, \bar{P} ANDA will extract the time-like form factors of the proton from electron-positron final states coming from $\bar{p}p \rightarrow e^+e^-$. In \bar{P} ANDA, it will be possible to determine the form factors from threshold to 20 GeV^2/c^4 . Due to the high statistics and full angular coverage it will be possible to significantly improve the existing results and to measure $|GM|$ and $|GE|$ separately.

2.1.3 Hadrons in Matter

The origin of hadron masses as a consequence of chiral symmetry breaking in QCD as well as its partial restoration in a hadronic environment can be studied in modifications of hadron properties, which are embedded in hadronic matter. Unlike previous experiments, which focused on the light quark sector, the high-intensity \bar{p} beam of up to 15 GeV/c will allow an extension of this program to the charm sector both for hadrons with hidden and open charm.

2.1.4 Hypernuclei

By replacing an up or down quark with a strange quark in a proton or a neutron, strangeness can be implemented into nuclei. Due to its strangeness, the particle is not restricted by the Pauli principle. In contrast to the neutrons and protons it can populate all states in the nucleus. This way a new third axis is added to the nuclear chart. With the \bar{p} beam of the HESR, \bar{P} ANDA will be able to form double-hypernuclei with reasonable statistics. The experimental setup at and around the target will be changed for these measurements as described in section 2.3.7

2.2 Facility for Antiproton and Ion Research

The Facility for Antiproton and Ion Research [3][4], is a new international accelerator facility for the research with antiprotons and ions. It is supported by an international cooperation and will be built near Darmstadt, Germany. FAIR will host laboratories for basic research for about 3000 scientists from about 50 countries and provide research facilities for the investigation of cosmic matter in the laboratory. A sophisticated accelerator complex will offer diverse beams, including antiprotons, stable ions, and exotic nuclei. A schematic of the future FAIR facility is shown in figure 2.1.

2.2.1 Main Experiments at FAIR

Beside \bar{P} ANDA 3 other main experiments will be performed at FAIR. This major pillars of the FAIR physics program will be introduced briefly, whereas further information on these and other experiments can be found in further publications [4].

APPA

Atomic, Plasma Physics and Applications (APPA) is an umbrella for several collaborations. They share installations and experimental techniques and deal with atomic, bio, and plasma physics as well as material science.

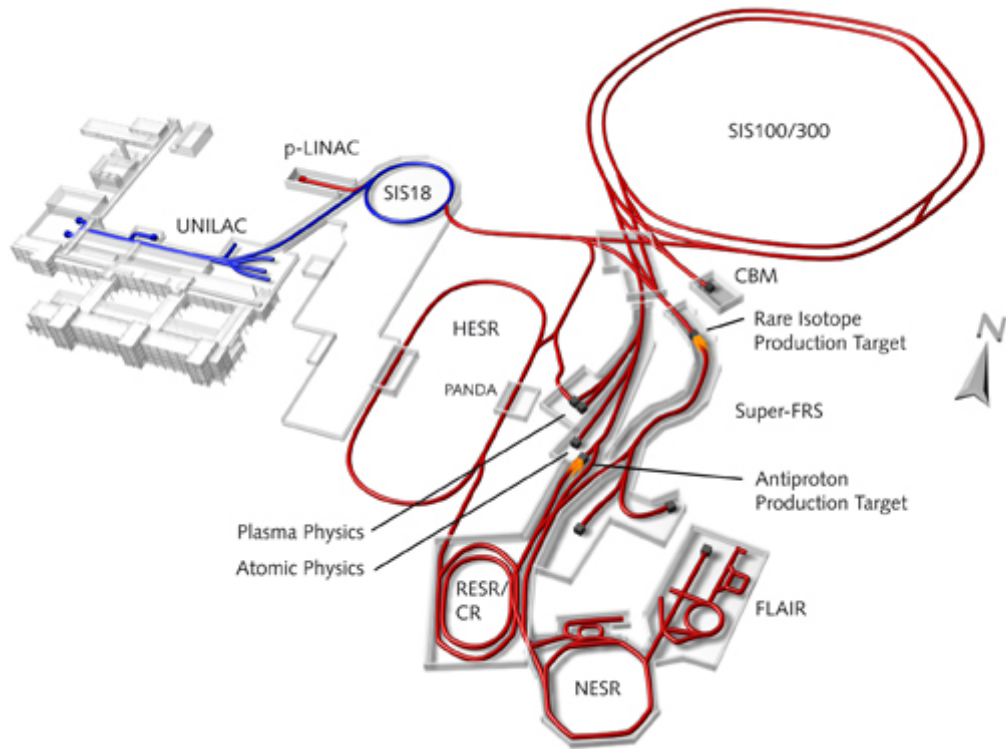


Figure 2.1: Schematic of the future FAIR layout incorporating the current GSI facilities (blue) in the future installations (red). The SIS 100 synchrotron, the storage and cooler ring complex, including CR and HESR, and the Super FRS experiment being some of the new parts. \bar{P} ANDA will be positioned right in the center of the image at the HESR.

CBM

The goal of the Compressed Baryonic Matter experiment (CBM) research program is to explore the QCD phase diagram in the region of high baryon densities. It creates highest baryon densities in nucleus-nucleus collisions, presumably beyond the chiral phase boundary and the confinement phase. Therefore unsolved questions in QCD, like confinement, chiral symmetry breaking and restoration, and baryonic matter in neutron star-like properties are part of the experimental program.

NUSTAR

The NUclear STructure, Astrophysics, and Reactions (NUSTAR) is a collaboration of more than 700 scientists. They will perform a collection of experiments to study the properties of light to heavy nuclei, from stable to the neutron and proton driplines and in other extreme conditions. The research interest of the NUSTAR collaboration is focused on the use of secondary beams from projectile fragmentation reactions separated and identified by the Superconducting FRagment Separator (Super-FRS), which is the central element of all NUSTAR experiments. The physics programs include the understanding of the inner structure of nuclei, as well as connected astrophysical topics.

2.2.2 High Energy Storage Ring

The $\bar{\text{P}}\text{ANDA}$ experiment will be located at the High Energy Storage Ring (HESR) [5] (cf. figures 2.1 and 2.2, which is a crucial device for the success of the experiment). $\bar{\text{P}}\text{ANDA}$ aims at both, high reaction rates and high momentum resolution in order to be able to study rare production processes and small branching ratios and to perform precise spectroscopic methods. To support the demanded high $\bar{p}p$ annihilation rate of $2 \cdot 10^7 \text{ s}^{-1}$ the HESR can store 10^{11} antiprotons with beam momenta from $1.5 \text{ GeV}/c$ to $15 \text{ GeV}/c$. For the production of antiprotons a combination of existing GSI accelerators like the UNILAC and SIS18 and new facility parts like the SIS100 synchrotron and a nickel, iridium or copper target are used [6]. The stored \bar{p} are freely coasting except for a 10% to 20% bunch structure allocated to a barrier bucket for compensation of energy losses. Two complementary operating modes are planned, named *high luminosity* and *high resolution* mode, respectively. The high luminosity mode with $\Delta p/p = 10^{-4}$, stochastic cooling and a target thickness of $4 \cdot 10^{15} \text{ cm}^{-2}$ will have an average luminosity of up to $L = 2 \cdot 10^{32} \text{ cm}^{-2}\text{s}^{-1}$. For

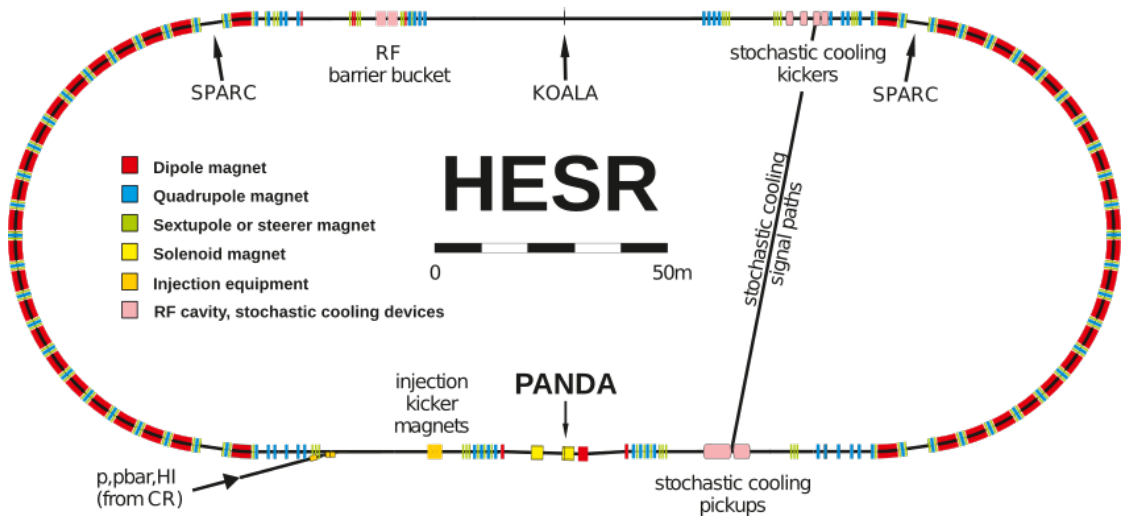


Figure 2.2: The High-Energy Storage Ring is the main facility to accumulate, store and accelerate or decelerate the antiprotons for the $\overline{\text{PANDA}}$ experiment.

the high resolution mode $\Delta p/p = 5 \cdot 10^{-5}$ will be achieved with electron cooling for momenta up to $p = 8.9 \text{ GeV}/c$. Operation will mainly be in conjunction with a cluster-jet target which will not impose a time structure onto the event rate. The cycle-averaged luminosity is expected to be $L = 2 \cdot 10^{31} \text{ cm}^{-2}\text{s}^{-1}$.

2.3 The $\overline{\text{PANDA}}$ Spectrometer

$\overline{\text{PANDA}}$ will be located at the High Energy Storage Ring (HESR) and is designed as a fixed target experiment. As discussed, it aims for a broad and challenging physics program. To measure and study the $\overline{p}p$ reactions comprehensively, a simultaneous measurement of all produced leptons, hadrons as well as photons is required. Therefore the $\overline{\text{PANDA}}$ experiment covers the full solid angle. It is capable of measuring the energy and momentum of all charged reaction products and photons as well as identifying their particle species over a wide momentum range. Figure 2.3 shows the full $\overline{\text{PANDA}}$ detector which consists of the Target Spectrometer, covering the interaction point with polar angles θ from 5 degrees to 140 degrees and the Forward Spectrometer, with a maximum angular acceptance of 10 degrees horizontally and 5 degrees vertically in beam direction. A cluster-jet or pellet target system can be operated to scatter the \overline{p} with an interaction rate of up to $2 \times 10^7 \text{ Hz}$. The tracking is realized by a combination of detector systems and supported by the magnet system. The particle identification is provided

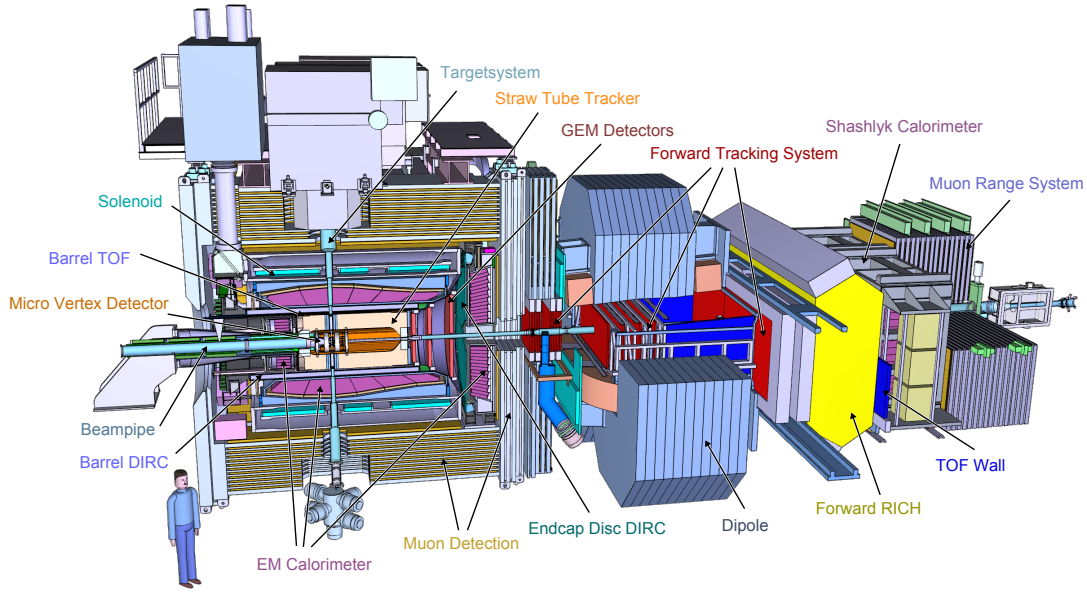


Figure 2.3: The \bar{P} ANDA Spectrometer

by various independent detector systems to ensure the full coverage in space and momentum as well as a necessary redundancy. The data acquisition (DAQ) of \bar{P} ANDA will pursue new ways. In this section the main subdetectors systems are briefly introduced.

2.3.1 Target System

To achieve the design luminosity of $2 \times 10^{32} \text{cm}^{-2} \text{s}^{-1}$, needed to support the broad physics program of \bar{P} ANDA, a target density of about 4×10^{15} hydrogen atoms per cm^2 is necessary. The \bar{P} ANDA target spectrometer allows the installation of two different target systems [7]. Left side of figure 2.4 shows a drawing of the beam line and the target beam tube. Both target installations breaks the vacuum pipe, inducing 10^{15} particles per cm^2 continuously. The worsens vacuum needs to be compensated by a series of turbo pumps.

Cluster Target

A cluster-jet beam is typically realized by expanding a pre-cooled gas through a nozzles into vacuum. The gas cools down and under appropriate conditions,

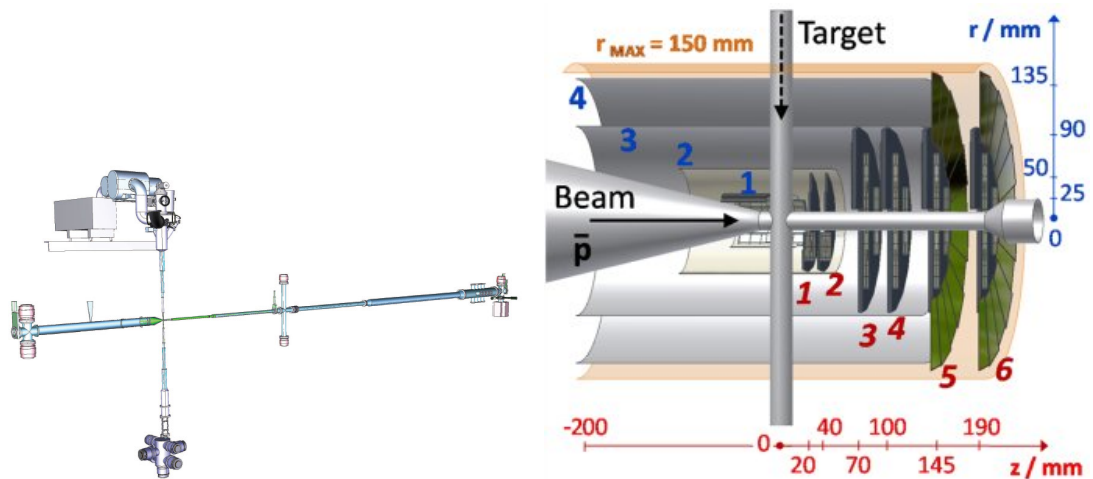


Figure 2.4: The left figure shows a drawing of the beam line crossing the target tube in the \bar{P} ANDA experiment. On the right side the \bar{P} ANDA Micro-Vertex-Detector surrounding the $\bar{p}p$ interaction point is shown. Pictures taken from [8].

condensation takes place. The created nano-particles are called clusters and have a typical size of $10^3 - 10^5$ atoms per cluster. Features of a cluster-jet beam are a homogeneous density distribution and sharp boundaries. Hence, it can provide a continuous target density and therefore luminosity without any time structure. With this system the luminosity can also easily be adjusted, by changing the target density during operation. Currently a prototype of the \bar{P} ANDA Cluster target is operated at University of Münster and already allows 8×10^{14} atoms/cm²

Pellet Target

The pellet target is realized by a stream of frozen Hydrogen microspheres (pellets), dropping through the beam. The pellet size can vary between 20 and 40 μm and the pellet stream has a low angular divergence of about ± 1 mm. The flow rate is in the order of 10^5 pellets per second falling with 60 m/s. A first prototype, developed in Uppsala achieved an average thickness of 10^{16} atoms/cm² and would force about 100 interactions per pellet. A new iteration is available at Forschungszentrum Jülich which can also produce Nitrogen and Argon pellets. Finally also other materials like Deuterium and heavy noble gases are planned for the pellet production.

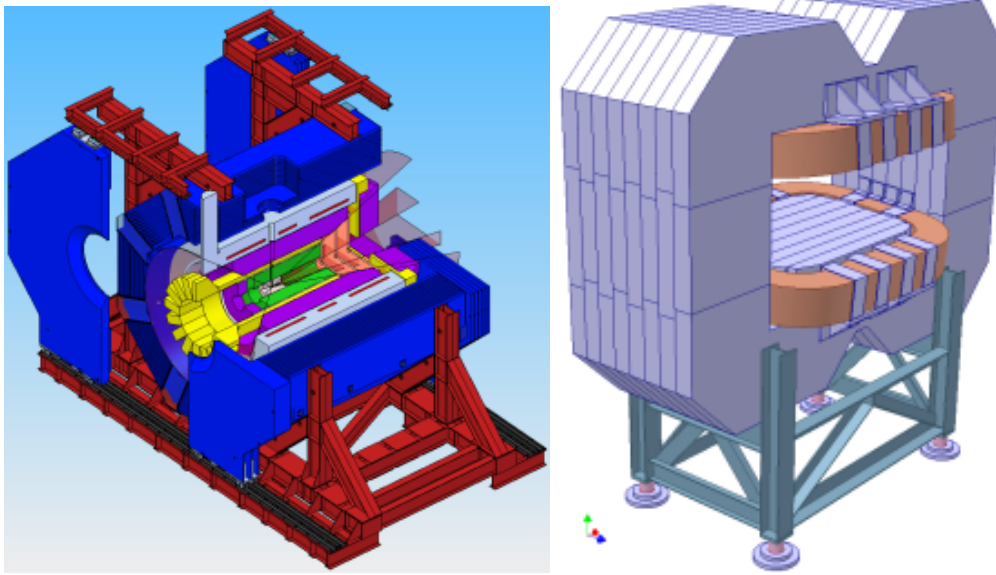


Figure 2.5: The figures show the solenoid magnet surrounding the detectors of the target spectrometer on the left side, and the dipole magnet located in the forward spectrometer on the right side. Pictures taken from [8].

2.3.2 Magnet System

To ensure a proper tracking, momentum reconstruction and particle identification appropriate magnetic fields are indispensable. In \bar{P} ANDA two magnets provide the ideal combination(cf. figure 2.5). A 2 T solenoid magnetic field will be installed in the target spectrometer, whereas a 1 T dipole field covers the forward region [9].

Solenoid Magnet

The magnetic field of 2 T in the target spectrometer is generated by a superconducting solenoid. It has a length of 4 m and a diameter of 1.9 m with the inner area completely free for subdetector placement. The magnet weighs more than 300 tons. It permits some space for a vertical target pipe and parts of it serve as the mounting point for inner detectors. The whole system will be placed on a movable platform to move it out of the beam line for commissioning and maintenance.

Dipole Magnet

Forward going particles will be reconstructed by the forward spectrometer with an excellent momentum resolution below 1%. To achieve this the particles will experience a field integral of 2 Tm generated by a large-aperture dipole magnet. The magnet weighs 220 tons and is complemented by additional detectors which are mounted also on a movable platform further downstream. It can be operated fully synchronous with the HESR to support the required ramping capabilities.

2.3.3 Tracking Detectors

A very accurate track and momentum reconstruction is crucial for the success of the broad and difficult physics program. For an efficient coverage of all solid angles and the exploitation of the two different magnetic fields in the target and forward spectrometer, in total 4 tracking sub-systems are planned in $\overline{\text{PANDA}}$, i.e. the Micro Vertex Detector (MVD), Straw Tube Tracker (STT), Gas Electron Multiplier Stations (GEM), Forward Tracking System (FTS).

MVD

The Micro-Vertex-Detector (MVD) [10] of $\overline{\text{PANDA}}$ is the inner most sub-detector system, surrounding the $\overline{\text{p}}\text{p}$ interaction point. The MVD is a very precise tracking device, with a focus on the vertex reconstruction. This is not only important for primary interaction vertices, but especially for displaced secondary decay vertices related to short-lived particles like hyperons or other particles including strangeness and charm. The MVD is composed of four barrel layers and six disks which are realized in a half-shell structure to fit the target pipe. (c.f. figure 2.4). The inner barrel layers 1 and 2 as well as the disks 1 to 4 are equipped with pixel sensors to deal with the high track densities, while the other layers are realized using double silicon strip detectors. A vertex resolution of about 5 mm is achieved.

STT

The Straw Tube Tracker (STT) [11] is the core tracking device in the target spectrometer of $\overline{\text{PANDA}}$. It surrounds the MVD and consists of 27 layers of straw tubes. A straw tube is a single channel drift tube filled with an optimized gas

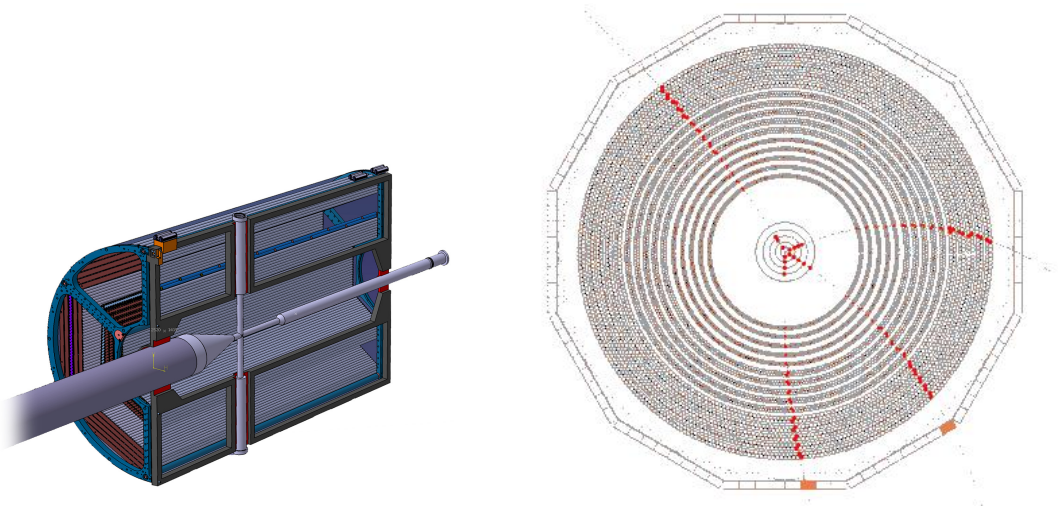


Figure 2.6: Left picture shows a 3D drawing of the Straw Tube Tracker (STT) of PANDA. The right picture shows a x-y profile of the STT with some marked tubes indicating a collected signal in red. The radius of the marked circles correspond to the drift radius of the produced charge inside the single tubes. Pictures taken from [8].

mixture which minimize the material budget to reduce scattering and electromagnetic showers, while offering good spatial resolution. One tube of the STT has a length of about 150 cm and a diameter of 1 cm. Figure 2.6 shows a drawing of the STT. Particles crossing one tube form electrons by ionizing processes. These electrons are accelerated by the electric field towards the wire in the center of the tube and form an avalanche which amplifies the signal before detection. A good time measurement of the particles is needed to extract the correct drift radius of the detected signals, while the collected charge is proportional to the energy loss of the particles.

GEM

Three or four disks of Gas Electron Multiplier Stations (GEM) [2] will close the gap in the acceptance between the STT and the Forward Tracking System. The discs cover a polar angle of 3° up to 20° and are placed at 81, 117, 153 and 189 cm in forward direction around the beam line (c.f. figure 2.7). Each disc consists of a double-sided read-out pad plane and a stack of three GEM foils for electron amplification on each side. A cathode and a window foil per side finish the setup. The GEM detectors provide a position resolution below $100 \mu\text{m}$.

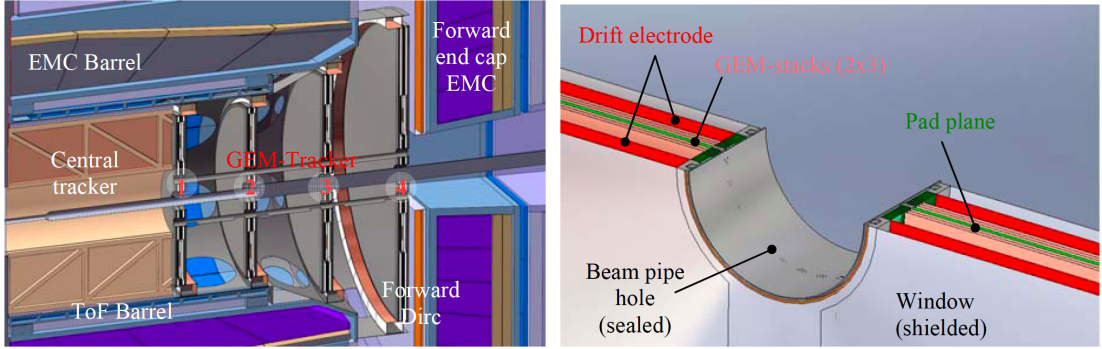


Figure 2.7: The left picture shows the area of the target spectrometer holding the GEM disks following the STT (Central tracker, CT) in beam direction. On the right picture the structure of a single GEM disk is shown. Pictures taken from [8].

FTS

The Forward Tracker System (FTS) [2] is responsible for the momentum reconstruction in the forward spectrometer. The working principle is based on the same technology as for the STT in the target spectrometer. The FTS consists of 13000 straw tubes forming six tracking stations of four straw tube double-layers. As shown in figure 2.8, the stations 1 and 2 are placed before the dipole, 3 and 4 in the dipole field and 5 and 6 afterwards. With this setup, achieving a position resolution of $100 \mu\text{m}$ per detection layer, a momentum resolution below 1% is expected.

2.3.4 Particle Identification

An important requirement of hadron physics experiments is the precise identification of charged and neutral particles. Therefore various dedicated particle identification (PID) systems will be realized in $\bar{\text{PANDA}}$ to support the physics program it is aiming for. These systems cover the majority of the solid angle as well as kinematic range of the produced particles.



Figure 2.8: The forward spectrometer with indications for the six FTS planes is shown. Pictures taken from [8].

DIRC

The $\bar{\text{PANDA}}$ DIRC detectors [12] are divided into two sub-detectors, using the Detection of Internally Reflected Cherenkov light (DIRC). They will be installed in the target spectrometer and provide efficient and clean PID. The barrel DIRC detector is located outside of the STT in a distance of about 48 cm from the interaction point and covers a polar angle of 22° to 140° . The gap between the barrel DirC and the forward spectrometer is closed by the End-cap Disc DIRC with an acceptance range of 5° to 22° . The basic principle for both detector system is the measurement of Cherenkov light produced by a charged particle in a medium with an array of photo detectors, and determining the Cherenkov angle to define the velocity of the transversing particle. Combining the informations of the tracking system with the DIRC detectors the particle species can be determined. Figure 2.9 shows drawing of the two DirC systems and indicates their positioning within the $\bar{\text{PANDA}}$ detector. Both detectors are build up by fused silica either in form of a thin slab like for the barrel DIRC or in form of a disc like for the End-Cap Disc DIRC. One drawback of Cherenkov detectors is the requirement of a minimum velocity of the particles to emit Cherenkov light. However particles below the threshold are covered by other detector systems.

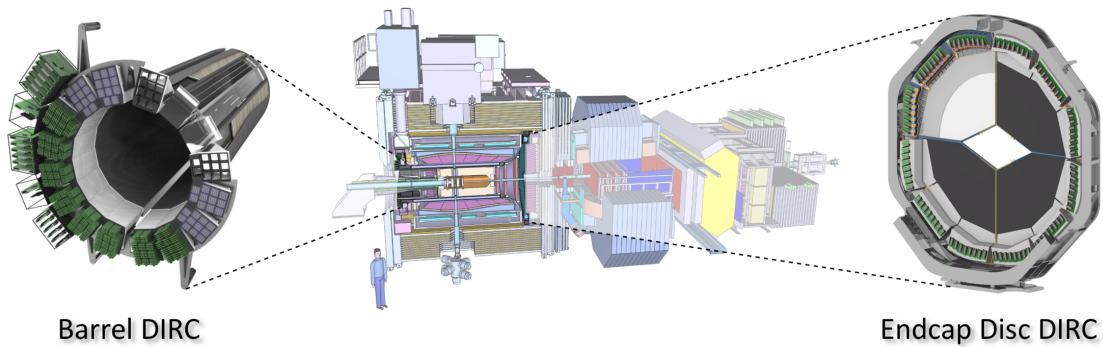


Figure 2.9: Drawing of the Barrel (left) and Endcap Disc DIRC (right) and their positions within the \bar{P} ANDA spectrometer. Pictures taken from [8].

TOF Systems

The \bar{P} ANDA Time-of-Flight system (TOF) consists of the Barrel TOF detector (BTOF) [13] and the Forward TOF Wall (FTOF) [2]. The BTOF will be installed in the target spectrometer between the Barrel DIRC detector and the EMC and is realized as a scintillator tile hodoscope. It is based on plastic scintillator tiles of size $90 \times 30 \times 5 \text{ mm}^3$, read out by silicon photomultiplier (SiPM) on both sides. Although many restrictions concerning space, material budget, magnet field and radiation hardness must be overcome, the setup allows a time resolution in the order of 50 ps. The BTOF is described more in detail in chapter 4. The FTOF is placed in the forward spectrometer in a distance of about 7 m from the interaction point. It uses a similar structure with larger scintillator plates of size $1400 \times 50 \times 25 \text{ mm}^3$, read out by photomultiplier tubes (PMTs) on both ends. The expected time resolution is in the same order as for the BTOF. The minimum requirement for the TOF detectors is a time resolution $\sigma \leq 100 \text{ ps}$. This allows, in combination with the informations of the tracking system, the identification of charged particles via the measured time of flight. Induced by this algorithm the separation power increases for slow particles and complement the PID information for particles below the Cherenkov threshold of about 700 MeV/c (c.f. section 6.4). Providing this precise time resolution, the TOF detectors are also very important for the trigger and event sorting algorithms, as discussed in chapter 6.

Muon Identification System

Some parts of the \bar{P} ANDA physics program have very small cross sections compared to background events and have mainly muons as final state particles. Therefore

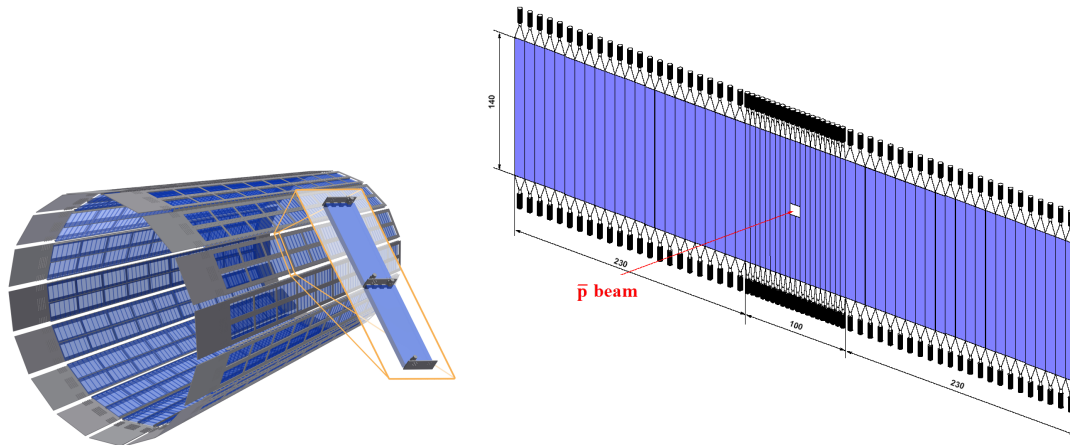


Figure 2.10: Drawing of the Barrel TOF (left) and the FTOF detector (right).

a very good muon identification is crucial for the background suppression. The muon identification is realized as a combination of PID systems like the calorimetry for the dE/dx measurement, scintillator counters for time-of-flight and Cherenkov counters. In addition a Muon Range System [14] will be installed in \bar{P} ANDA. The Muon System in the target spectrometer is split into two parts, i.e. the Barrel System and the End Cap System. The Barrel consists of 13 sensitive layers, each 3 cm thick, alternating with 3 cm thick iron absorber layers. Due to the higher momenta in forward direction more material is needed in the End Cap. Six detection layers will be placed around five iron layers of 6 cm each. The detection layers are realized using Mini Drift Tubes (MDTs). Another part of the muon system is located at the end of the forward spectrometer about 9 m from the interaction point and is composed similar to the barrel muon system. Figure 2.11 shows a drawing of the Muon System including some other \bar{P} ANDA detector system for orientation.

RICH Detector

The Ring Imaging Cherenkov Counter (RICH) [2] will be placed in the forward spectrometer. It uses an aerogel radiator material with a refractive index of about 1.02 to provide PID also at the highest momenta between 2 GeV/c and 15 GeV/c especially optimized for π/K separation. Mirrors will be used to reflect the Cherenkov photons onto photomultiplier or hybrid photon detectors outside of the magnetic field region.

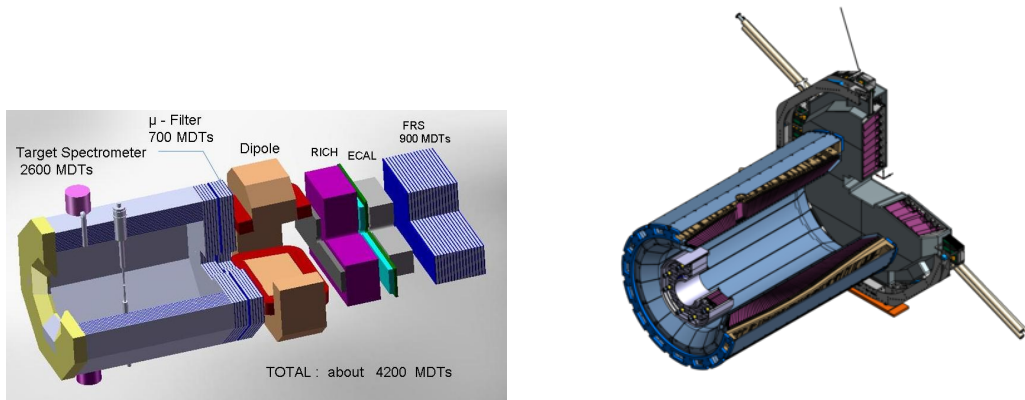


Figure 2.11: On the left side the Barrel, End Cap and Forward Muon System is indicated together with some other \bar{P} ANDA systems for orientation. The right picture shows a technical drawing of the barrel EMC located in the target spectrometer of \bar{P} ANDA. Pictures taken from [8].

2.3.5 Electromagnetic Calorimetry

Electromagnetic calorimeters (EMC) [15] are located in the target spectrometer as well as in the forward spectrometer. In the target spectrometer it is realized as a barrel with two end caps, while the forward part is a shashlik type sampling calorimeter. The barrel EMC with a radius of 57 cm consists of 11360 crystals of 20 cm length, and the backward end cap EMC of 524 crystals. They are read out by large area avalanche photo diodes (APDs), which are specifically developed for this purpose. The calorimeter will be operated at $-25\text{ }^{\circ}\text{C}$ to gain an additional factor four in light yield. The expected energy resolution for the barrel EMC is below 2% for particle energies in the order of 1 GeV. The good intrinsic time resolution below 1 ns can also provide additional information for event trigger and sorting algorithms. The Shashlyk EMC in the forward spectrometer is located at about 7.5 m from the interaction point. It is based on alternating layers of lead and scintillators. It is read out with wavelength shifting fibers coupled to PMTs. An energy resolution of 4% will be achieved with this type of calorimeter.

2.3.6 Luminosity Detector

Antiprotons have a well-known angular distribution and cross section for elastic scattering. A luminosity detector [2] located at the end of the forward spectrometer about 12 m from the interaction point, will measure scattered \bar{p} . Although only

covering a very small polar angle from about 0.17° to 0.45° , the absolute luminosity in the $\bar{\text{PANDA}}$ spectrometer can be deduced from the informations provided by this detector.

2.3.7 Hypernuclear Detector Extension

To perform the hypernuclear physics program of $\bar{\text{PANDA}}$, the spectrometer can be modified with a dedicated hypernuclear target as well as detector [2]. This extension is inserted at the place of the MVD and End Cap EMC and allows the measurement of hyperons embedded in nuclei. Therefore a dedicated secondary target of 25 to 30 mm thickness absorbs hyperons to form double hypernuclei. Layers of silicon strip detectors and arrays of germanium detectors are used for a high precision γ -spectroscopy.

2.3.8 DAQ

$\bar{\text{PANDA}}$ will utilize a novel approach for its Data Acquisition System (DAQ) [16]. The $\bar{\text{PANDA}}$ DAQ design does not use fixed hardware based triggers but features a continuously sampling system where all subsystems are synchronized with a precision time stamp distribution system. Event selection is based on real-time “feature extraction” of the event topology, filtering and high level correlations. The final trigger decision is done at computer nodes utilize the fully reconstructed event data. The main advantage of this concept is the high flexibility, e.g. in the choice of trigger algorithms.

The data flow and processing is spatially separated into the Front End Electronics (FEE) part located on the actual detector subsystems and the Data Acquisition (DAQ), located off-detector. Each subsystem and the respective FEE is configured as an autonomous self-triggering unit, also responsible for data preprocessing at the read-out stage, including zero suppression and intelligent data reduction by clustering or signal shape analysis. Nevertheless, operating the $\bar{\text{PANDA}}$ detector at interaction rates of 2×10^7 the typical event sizes of 4–20 kB still lead to mean throughput of about 200 GB/s. A data rate reduction of about a factor 1000 is envisaged in order to write event data of interest to permanent storage. High peaking rates above the average data rate and consequential increased pile-up rate may occur due to a \bar{p} beam time structure, target thickness fluctuations (in case of pellet target) and luminosity variations during the HESR operation cycle. The main elements of the $\bar{\text{PANDA}}$ DAQ are the data concentrators, the compute nodes

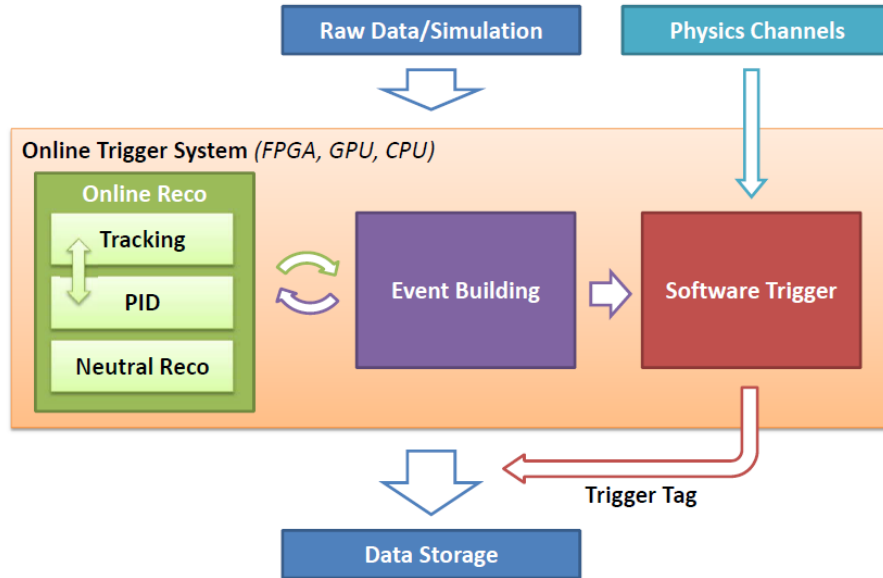


Figure 2.12: Scheme of the online reconstruction and trigger system for the continuous, time based read out of \bar{P} ANDA.

and high speed interconnecting networks. The data concentrators aggregate data via point-to-point links from the FEE. The compute nodes provide the feature extraction, event building and physics driven event selection. This online data processing is done in an iterative process. The event wise sorting of the data sent by the FEE, called event building, followed by a fast track reconstruction and particle identification is processed. The obtained information will be used to enhance the event building and tracking further to a level where the software filter can decide whether to discard or store the respective data [17]. Figure 2.12 shows an outline of the planned execution.

3 PandaRoot

PandaRoot [18][19] is the software framework for the $\bar{\text{P}}\text{ANDA}$ experiment. It provides a framework for full simulations of the particle transport, detector interaction and response, reconstruction and PID as well as analysis tools for the planned physics studies of $\bar{\text{P}}\text{ANDA}$. PandaRoot is implemented in the FairRoot [20] framework which is the common computing structure for the future FAIR experiments. FairRoot is based on ROOT [21] and Virtual MonteCarlo [22] (VMC) packages and contains a collection of software and tools for the description of the detectors and the simulation of physical reactions. Detector specific geometry, reconstruction and particle identification code are developed within PandaRoot. Figure 3.1 describes the dependencies of the different packages. The software is supported by various C++ compilers and several Linux distributions as well as macOS. In this section the packages of PandaRoot will be briefly introduced and the basic simulation workflow will be explained.

3.1 Root

Root is a modular, object-oriented (OO) scientific software framework, which provides all the functionalities needed to deal with big data processing, statistical analysis, visualization and storage [24]. “ROOT written in C++, contains, among others, an efficient hierarchical OO database, a C++ interpreter, advanced statistical analysis (multi-dimensional histogramming, fitting, minimization, cluster finding algorithms) and visualization tools. The user interacts with ROOT via a graphical user interface, the command line or batch scripts. The command and scripting language is C++ (using the interpreter) and large scripts can be compiled and dynamically linked in. The OO database design has been optimized for parallel access (reading as well as writing) by multiple processes” [25]

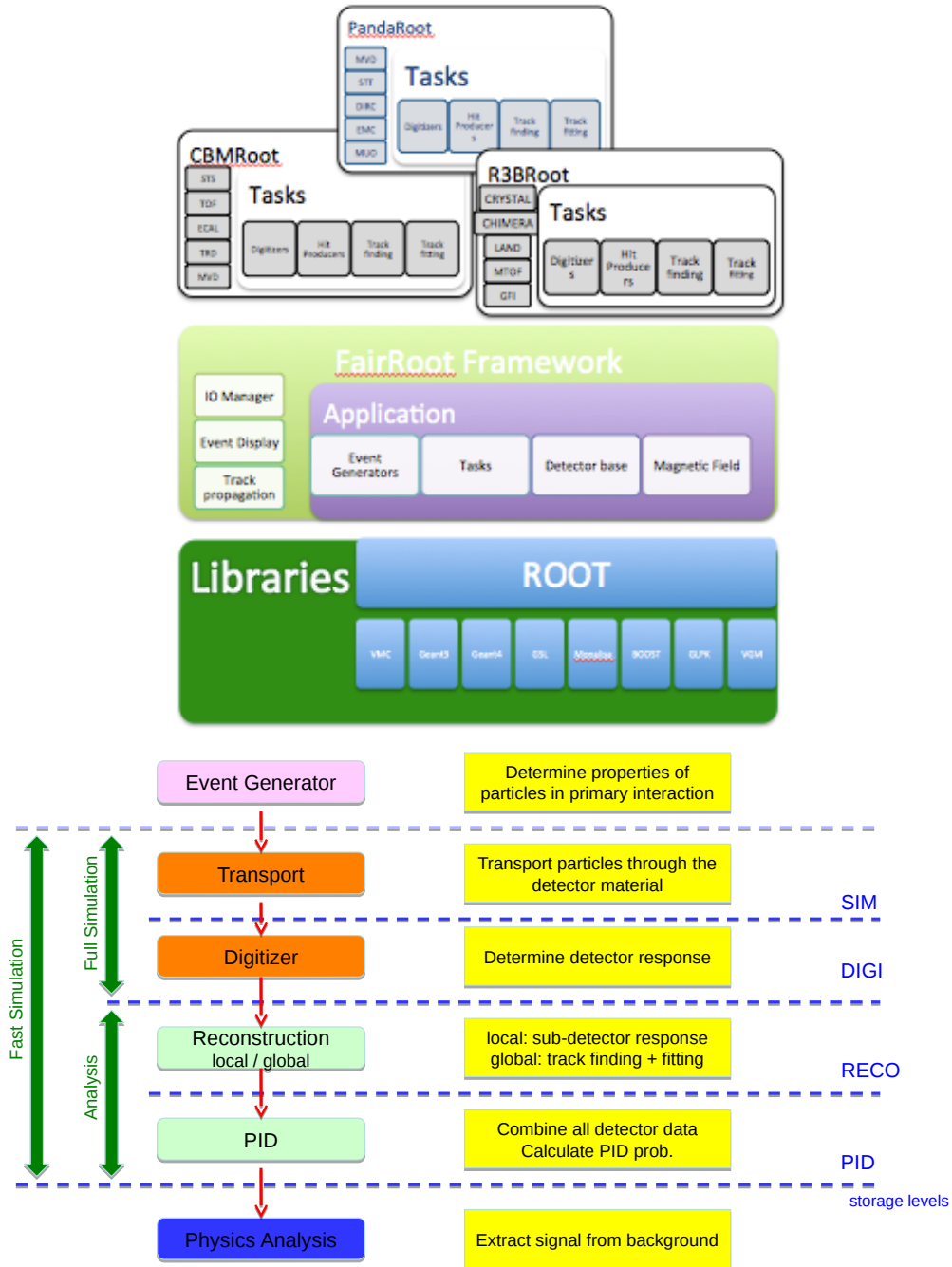


Figure 3.1: The upper picture summarizes the structure and dependencies of the PandaRoot framework [23]. The bottom layer includes third party software, the middle layer the common framework for FAIR and on top some of the detector and experiment specific adaptations are presented. The bottom diagram shows the simulation stages within the PandaRoot framework.

3.2 FairRoot

The FairRoot framework is based on ROOT and includes additional core services for detector simulation and offline analysis. It provides base classes to construct experimental setups in an efficient way using the basic Root classes. The implemented simulation routine uses Virtual Monte Carlo which allows the easy usage of different particle transport engines. Some basic functions of Root are extended to simplify the implementation of complex reconstruction chains and analysis tasks. This also includes an interface to run parts of the code on GPUs called FairCuda. Data IO, as well as parameter handling and database connections are also handled by the framework. Because of the demand of some experiments, e.g. $\bar{\text{P}}\text{ANDA}$, the framework is capable of handling free flowing input streams of detector data, which is necessary to deal with its trigger-less operation mode. Therefore the framework provides basic classes and functions to simulate time sorted data streams based on standard event based simulations, including also event mixing.

3.3 PandaRoot

Detector specific geometry, reconstruction and particle identification codes are developed within PandaRoot and can be run in the respective stages, which are indicated in figure 3.1. In the simulation stage(SIM), specific initial state particle distributions, physics channels and antiproton-proton background reactions are produced. For that purpose, various event generators can be called with different focus, e.g. EvtGen [26], DPM [27], UrQMD [28] and Pythia [29]. Particle transport through the detector material is realized with Virtual Monte Carlo, which can load either Geant4 [30] or Geant3 [31] for the simulation itself. In the following digitization stage the generated Monte Carlo (MC) data is processed to simulate the realistic response of the subdetectors. In the reconstruction stage, information provided by the tracking detectors is put together to reconstruct charged tracks and propagate these to the outer subdetectors. In the PID stage various particle identification (PID) algorithms based on different subdetectors are performed. A probability density functions (p.d.f.) for every reconstructed track and particle species is computed per PID algorithm. These are combined to receive a global identification probability using Bayes theorem [19]. For the following analysis stage various fitting algorithms for the four momentum and position of the particles as well as particle selection and combination mechanisms are provided.

3.3.1 Generators

Generators determine the produced particles and their properties in a specified reaction like a beam-target reaction in $\overline{\text{PANDA}}$ according to a chosen model. These model can be backed up by measurements or just theoretical predictions. For most generators the decay chains of short-lived particles can be set manually to focus on specific channels.

EvtGen

EvtGen is a Monte Carlo event generator that simulates the decays of heavy flavour particles, primarily B and D mesons. It contains a range of decay models for intermediate and final states containing scalar, vector and tensor mesons or resonances, as well as leptons, photons and baryons. Decay amplitudes are used to generate each branch of a given full decay tree, taking angular and time-dependent correlations into account which allow for the simulation of CP-violating processes.“ [32]

DPM

The Dual Parton Model (DPM) generator is based on known cross-sections of $\overline{p}p$ collisions. It includes inelastic hadronic, elastic hadronic as well as coulomb elastic scattering processes. While it is not possible to specify certain channels, this generator allows for studies on the expected background. For most of the performance studies described in this thesis, the DPM generator was used to generate realistic particle distributions. of background events.

BoxGenerator

The BoxGenerator produces particles of a specified type with parameters randomly distributed in a definable range. The number of particles per event and their types are defined by the user. If necessary it is also possible to specify all parameters exactly. This generator is very useful for technical purposes like detector optimization and algorithms performance studies due to the a priori defined particle parameters.

UrQMD

The UltraRelativistic Quantum molecular Dynamics Model (UrQMD) generator is also included in PandaRoot. UrQMD produces particle distributions according to $\bar{p}N$ heavy nuclear interactions. The UrQMD is mostly used to generate background events for this type of experiment, which is planned for later stages of \bar{P} ANDA.

Pythia

Pythia is another $\bar{p}p$ background generator used for an energy regime above the for \bar{P} ANDA planned region. Nevertheless it is included for testing purposes.

3.3.2 Detector Simulation

In this stage the interactions of the particles with all the included active and passive material of the \bar{P} ANDA detector, as well as the response of the material like excitations are simulated. As one of the first tasks all the included subdetector geometry descriptions are loaded in this stage. This stage of the simulation is performed event by event without interactions and pileups in between the events.

Particle Propagation

After the generation of the particle, the propagation through the detector is handled by the Virtual Monte Carlo [22] package which enables the use of two different transport engines, i.e Geant 3 and Geant 4. These engines simulate the detector material interaction of the particles, the influence of the set magnetic field as well as the decay of the particles. Daughter particles are treated in the same way. Particles with an kinetic energy below the cut-off energy are ignored to save computing power.

Active Detector Material

The specific behavior of the active detector materials is implemented individually for every subdetector. In a first step the momentum, energy, particle ID, position,

time and energy deposit of passing particles are collected event by event and stored for every subdetector.

3.3.3 Digitization

While the simulation stage focuses on the particle propagation and the simulation of the relevant physics processes caused by the particle passage, the following digitization stage processes the simulation of the functionality of the various subdetectors and their electronics. It should cover artificial generation and suppression of electronic noise, signal thresholds, or inefficiencies as well as the local reconstruction. The local reconstruction includes all data processing which is done close at the detector. The raw data of the sensors are rarely used or even useful at later stages. For example the FEE channel number and the TDC and QDC value are specific to the exact setup of the detector. These values are converted to a understandable, general quantities like position in global coordinates, ns, and charge by a "calibration". Zero-suppression is done at the local reconstruction as well. Information passed to the next stage should not include any information not accessible from the real experiment.

Time Based Simulation

In the standard digitization mode, the data from the same annihilation event are processed event by event with a $\bar{p}p$ annihilation time set to 0 for every event. However, to simulate the continuous readout of $\bar{P}ANDA$ the option to run a time based digitization is included in this stage. At the first level the $\bar{p}p$ annihilation times are set to realistic values and the subdetector time information is updated respectively. A full time based digitization includes event mixing, and pile up in the various detectors. This simulation of a continuous read out can be realized individually by the detector groups. However, FairRoot provides some specialized functions and containers to buffer, pile up and manipulate the data of the simulation stage, while still giving ample scope to include the detector specific behavior. The output data of this digitization mode are not sorted event by event anymore. However, the subdetector data are sorted in time and continuously streamed to the next processing stage or the output data file.

3.3.4 Reconstruction

In the reconstruction stage the data of the various sub detectors are put together to reconstruct the tracks of the detected particles. Various tracking algorithms are currently under development with focus on different purposes like online or offline reconstruction, primary tracks or secondary tracks with a displaced vertex. Common to all algorithms is the extensive usage of data provided by the dedicated tracking detectors, i.e. MVD, STT, GEM, and FTS. Studies on this algorithms will be used to develop a final global tracking algorithm.

Offline Reconstruction

Most of the tracking algorithms implemented in PandaRoot so far are designed for the so-called offline reconstruction. These algorithms expect the input data sorted event by event and assume a reconstructed $\bar{p}p$ annihilation time (t_0). This kind of reconstruction will be performed after the software filter/trigger decision on the stored data. Therefore these reconstructions can be performed at any time, or even reran and the processing time is not as critical as for other steps.

Online Reconstruction

An important subset of the reconstruction is the so-called online reconstruction. This stage will be performed between the detector readout and the software filter decision, as already mentioned in the DAQ section 2.3.8. This reconstruction is closely linked to the time based simulation. Important tasks in this stage are the event triggering, t_0 determination and the sorting of the continuously streamed data into event packages. In this stage also a fast track reconstruction and PID is necessary to support the software trigger with all information needed to make a valid decisions on discarding or storing the data. Possible algorithms are currently under development. Some parts of such algorithms will be discussed in chapter 6.

3.3.5 PID

In the Particle Identification (PID) stage the particle species of the reconstructed particle tracks are determined. In a first step the reconstructed particle tracks are propagated to the outer detectors and are matched with the data of the PID

detectors. Each sub detector system supports specialized PID algorithms which cover a certain momentum range of particles and could be run independently of all other PID algorithms. In order to combine the results every system provides a probability density function (p.d.f.) for every particle hypothesis. The tested hypotheses are p , \bar{p} , $\pm K$, $\pm\pi$, $\pm\mu$, $\pm e$. Under the assumption of independence of the sub detector p.d.f.s, these results are combined in a global PID probability using a Bayesian approach. In this stage the EMC is important to identify neutral candidates. Energy deposits in the EMC, which can not be associated to a reconstructed and therefore charged track are tested for neutral particle hypotheses.

3.4 Analysis

The last stage of data processing is the analysis of the reconstructed information. This can be done using the so-called RHO package which is included in PandaRoot. The RHO package includes selected parts from the analysis package of the BaBar [33] experiment ported to PandaRoot. However the framework was extended by necessary functionalities. It provides an efficient way of working with these particle candidates and offers fast standard operations like creating composite particles, applying cuts and fits while taking care of double counting. Implemented fitters allow mass fitting, 4C kinematic fitting and vertex fitting.

4 $\overline{\text{P}}\text{ANDA}$ Barrel Time-of-Flight detector

The Barrel TOF will provide precise timing information for all charged particles reaching the device. The detector concept is a TOF hodoscope in which large organic scintillator plates are segmented in many small scintillator tiles made out of the fastest scintillating materials. A CAD drawing of the current design of the Barrel TOF is shown in Fig. 4.1. The optical readout of the scintillating light is performed by Silicon Photomultiplier (SiPM) embedded within the gaps between tiles. Due to this small segmentation the variation of the photon path length inside the scintillator material becomes small and the time resolution improves. In addition a spatial resolution given by the width of the scintillating tiles in z direction is provided. A more accurate resolution is achieved for the azimuthal direction, using timing differences of the double readout of each scintillator end. SiPMs are compact, robust and without intrinsic limits to lifetime coming from integrated anode currents. If used in an environment with ionizing radiation, their functionality however will be slowly compromised. In $\overline{\text{P}}\text{ANDA}$ the Barrel TOF will surround the interaction point at a radial distance of about 50 cm and cover the central region of $22^\circ < \theta < 140^\circ$. A coverage of the smaller angles with scintillation tiles is not intended. Instead a conventional Forward TOF wall much further downstream will cover the angles $0^\circ < \theta < 5^\circ$ and $0^\circ < \theta < 10^\circ$ in the vertical and horizontal direction, respectively. In this chapter the desired capabilities for the detector are discussed briefly in section 4.1 while the technical requirements to fulfill these are summarized in section 4.2. In the last section (4.3) the final design of the Barrel TOF is described in more detail. The descriptions in this chapter are partly also published in the Technical Design Report of the Barrel TOF [13]. For further reading a more in depth discussion of the technical aspects of the detector can be found in that document.

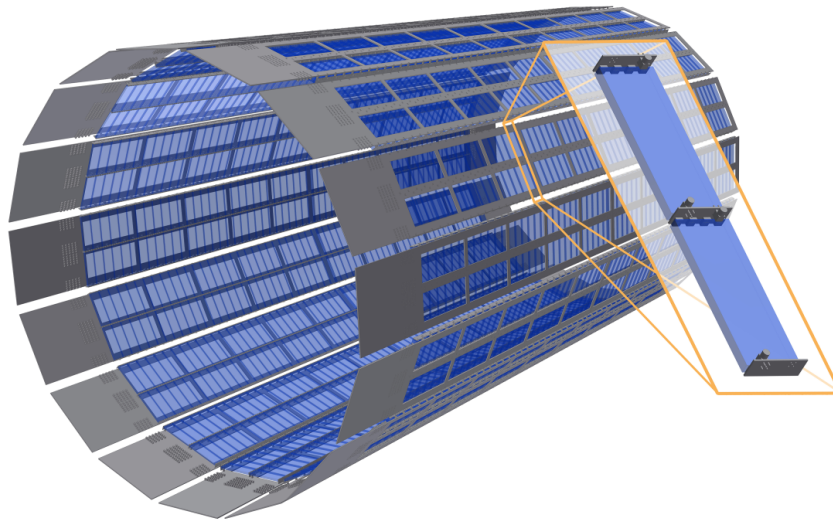


Figure 4.1: CAD Drawing of the whole Barrel TOF detector with an insert of a magnified drawing of a pair of scintillator tiles. Scintillator tiles are drawn in blue, printed circuit boards (PCB) in grey. It is comprised of 16 segments and covers an active area of 5 m^2 around the $\bar{p}p$ interaction point

4.1 Capabilities

Studies of the \bar{P} ANDA detector system revealed that an additional fast timing counter in the TS would remedies some shortcoming of the system [13][16, 34, 35, 36, 1].

4.1.1 Particle Identification

The Barrel TOF will extend the PID capabilities of the \bar{P} ANDA detector to regions not covered by other detector systems. It will provide PID based on the time-of-flight for particles at large polar angles in combination with the central tracker. Therefore the Barrel TOF can identify also slow particles below the momentum threshold of the Cherenkov detectors. PID is also provided for faster particles and the redundancy of the DIRC and the Barrel TOF in this region will be used to further precise the results. The PID capabilities are discussed in more detail in section 6.3 and 6.4.

4.1.2 Software Trigger

\bar{P} ANDA has no hardware trigger but continuously digitizes all detector signals after autonomous hit-detection. The complete processing of all events at the full interaction rate is not possible since this would require computing resources exceeding the cost of the entire experiment. Therefore simpler event signatures have to be used for a software trigger, i.e. a very fast first selection level which takes only few microseconds. Depending on the available computing power and buffer space a reduction by a factor of 100–1000 must be achieved in the first fast selection. This trigger may be based on algorithms relying on one or few detectors. These algorithms must not require long data processing in the FEE and in the following computational operations. The goal is to achieve high rejection factors from simple signatures like particle multiplicity, particle coincidences in time, or topological track pointing. In the start-up phase of \bar{P} ANDA the more complex detector systems like electromagnetic calorimeter, central tracker and micro-vertex detector have to be calibrated and aligned carefully and details of their stable operation have to be established in practice. In such a learning phase these detectors are not well suited as input for the fast software trigger. Any signature based on not understood or simply not well calibrated detectors will be spurious and unreliable and may create biased signatures. Drawing physics observations from these signatures will be difficult or even erroneous. At the beginning of any experiment it is therefore necessary to base the input for further better understanding of a complex detector system on simple and reliable detectors for reference, e.g. scintillator based devices .

4.1.3 Event Sorting

In addition to the contribution of a time-of-flight detector system leading to an increased performance of particle identification, a high time resolution will serve as an essential ingredient for any event building algorithm. One of the key features of the \bar{P} ANDA experiment will be a high luminosity mode with sufficiently high event rates to tackle physics questions with adequate statistical power. In this mode the average event rate will be in the order of $\dot{N}_{avg} = 20$ MHz. This poses a technical challenge for the readout, which is intensified by the fact that the events are not distributed equidistant in time. Instead they exhibit an exponential behavior concerning the time difference between sequent events as illustrated in Fig. 4.2. This means that smaller time differences are in general more likely. In particular 63% of all reactions have a δt smaller than the average value. At this point it seems clear that a high resolution timing is desirable to disentangle signals from

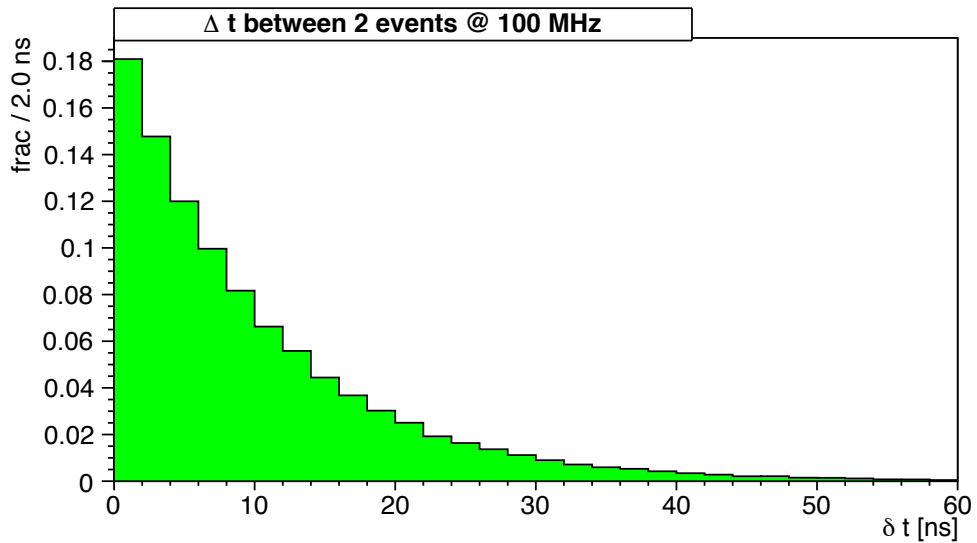


Figure 4.2: Distribution of the time difference δt between two sequent reactions at an instantaneous event rate of $\dot{N} = 100$ MHz.

different events. Event Sorting and t_0 determination is discussed in more detail in chapter 6.

4.1.4 Pattern Matching

A detector with good time resolution outside the central tracker (CT) may serve as a seed for track finding in the CT. This works best if the detector would resolve both ϕ and z at a reasonable granularity. In contrast, developing track seeds from the side of the MVD requires more processing time due to the more complicated structure of the MVD and the higher track density. Moreover, displaced tracks emerging from weak decays will be missed and require a second pattern recognition pass. The track seeding by the timing detector does not require the highest possible time resolution. But a key issue is to have the hits of the timing detector easily available without further parallel processing or calibration, since otherwise the tracking process would have to wait for this pre-processing.

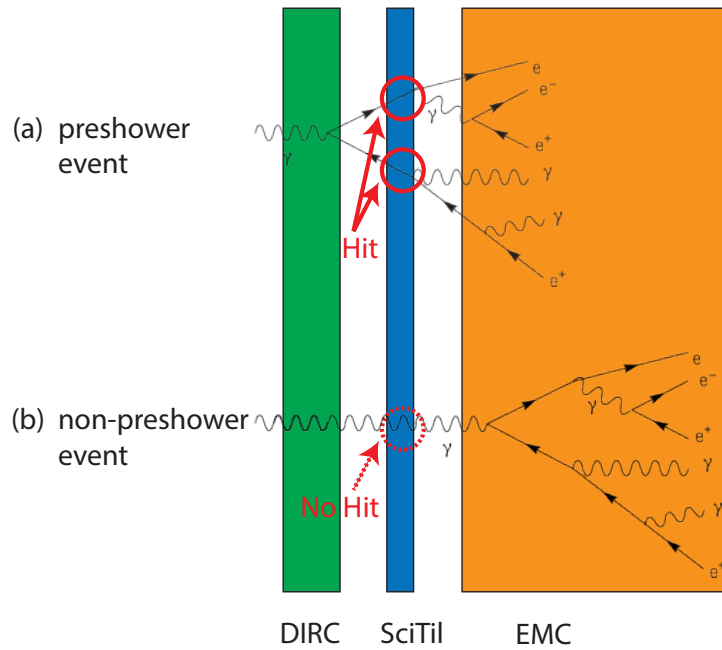


Figure 4.3: Schematic drawing of the pattern for a preshower event (a) and non-preshower event (b).

4.1.5 EMC Preshower Detection

The finite material budget of detectors and supporting structures in front of the EMC leads to a non-zero probability that γ -rays start electromagnetic showers before reaching the EMC detector. Such an event is called a preshower. In an earlier study [15] it was shown that in the planned \bar{P} ANDA detector system preshowers take place with finite probability mostly due to the material of the barrel DIRC detector. As a consequence the energy resolution of γ -rays deteriorates. The Barrel TOF detector is located right after the barrel DIRC and right before the EMC detector with essentially the same solid angle coverage. The thin plastic scintillators of the Barrel TOF detector have a high detection efficiency for charged particles but are essentially blind to γ -rays. Therefore the Barrel TOF can tell if a registered hit in the EMC is caused by a γ -ray or by a charged particle (preshower event). Fig. 4.3 describes the difference of patterns between a preshower event and a non-preshower event.

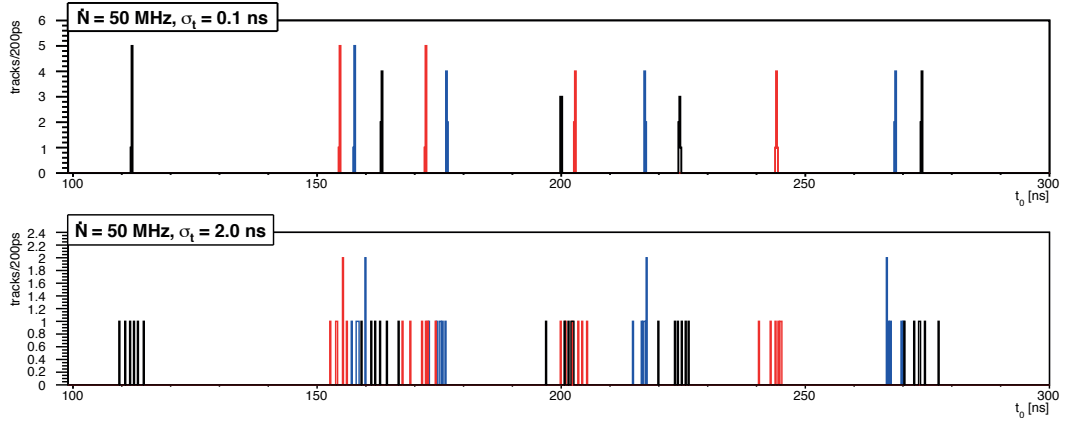


Figure 4.4: Illustration of $t_{0,i}$ distribution of reactions with 6 tracks at an instantaneous rate of $\dot{N} = 50$ MHz and total time resolutions of $\delta t_1 = 100$ ps (top) and $\delta t_2 = 2$ ns (bottom). The three colors black, red, and blue are cyclically used to mark time signals $t_{0,i}$ from different events.

4.2 Requirements

4.2.1 Time Resolution

Beside the need of a good time resolution for a time-of-flight based PID, also the event entanglement is an issue addressed by the time resolution. The performance of the event building depends on the spread of the determined event time ($t_{0,i}$) distribution. The better the $t_{0,i}$ s of different events are separated in time, the higher the selection efficiency will be. Overlapping distributions however may result in efficiency loss, since these events cannot be separated in a simple way anymore. This was also discussed in the proposal for the Barrel TOF [36]. Figure 4.4 illustrates the clustering and overlapping of events for different time resolutions. The time signals of different events are colored cyclically with the colors black, red and blue. While in the first case with time resolution $\delta t = 0.1$ ns different events can be separated well, this feature gets partially lost in the second case with $\delta t = 2.0$ ns.

The fraction of events whose creation time distributions does not overlap with those of earlier or later events has been determined for reactions with 6 charged tracks as a function of the instantaneous rate in the range between 10 MHz and 100 MHz for four different time resolution values $\delta t \in \{0.1, 1.0, 2.0, 5.0\}$ ns. The four curves, colored in black, red, blue and magenta, respectively, are shown in figure 4.5.

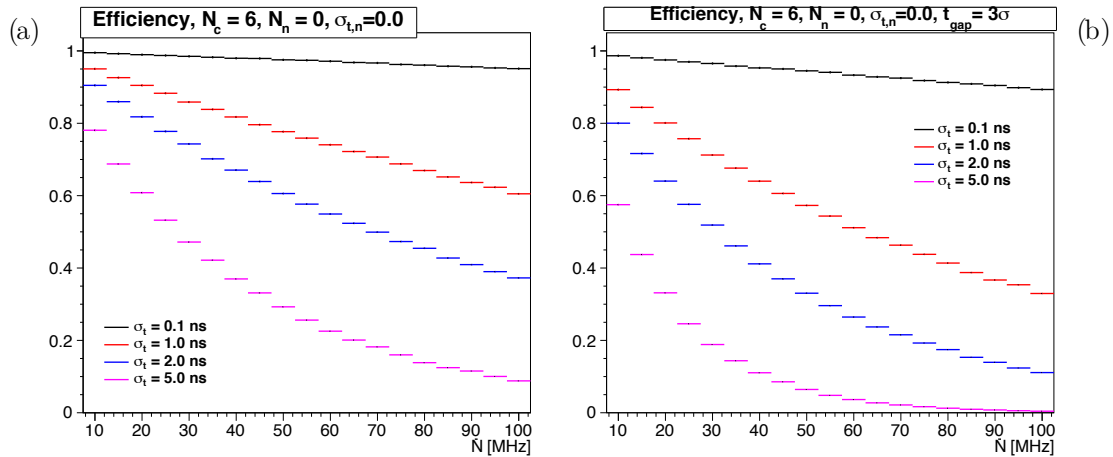


Figure 4.5: Event rate dependent efficiency based on pure overlap (a) and on an event building algorithm assuming a time gap of 3σ (b) described in the text for reactions with $N_c = 6$ charged tracks. The values are plotted for instantaneous rates between 10 MHz and 100 MHz and time resolutions of $\delta t \in \{0.1, 1.0, 2.0, 5.0\}$ ns, colored in black, red, blue and magenta, respectively.

4.2.2 Position Resolution

A reasonable granularity is necessary for the Barrel TOF. This is first of all in order to keep a double- or multiple-hit pile-up probability in a single tile lower than a certain level so that the detector can remain functional during the high luminosity operation. The double-hit probability and its influence on the efficiency was quantitatively studied by simulations using the latest geometry. The results will be discussed in section 5.2.2. The granularity is also necessary in order to match the hits in the Barrel TOF with hits in other detectors. Matching between detectors is done in a space-time phase space. Even though the Barrel TOF has the finest time resolution in the target spectrometer, an order of cm position resolution is desired. This helps reduce possible matching combinations and hence rejecting fake tracks in a pattern matching algorithm. It also helps with the EMC preshower detection as well. For each EMC cluster a corresponding hit in the Barrel TOF is searched for in both time and space, where the window is given by the time resolution and position resolution of the Barrel TOF, respectively.

4.2.3 Mechanical Requirements

The \bar{P} ANDA Barrel TOF detector shares the mechanical support structure with the Barrel DIRC. Due to this constraint, the Barrel TOF has the same 16-fold azimuthally segmented structure. Figure 4.6 shows the half-barrel = 8 segments of the Barrel DIRC and Barrel TOF detectors, kept in the same support structure. The maximum allowed radial space for the Barrel TOF is 20 mm. Beside this space limitation the design must deal with other restrictions. To minimize any disturbance of the EMC measurements the material budget and radiation length must be kept as low as possible. The detector elements itself should have a modular structure and be decoupled from the maintain of the Barrel DIRC. Still the system has to be robust against mechanical shocks and should stay operational for more than 10 years of \bar{P} ANDA without any planned major repair services. Due to the magnetic field in the target spectrometer only non-magnetic material can be used. The radiation hardness is also an issue to be addressed. The \bar{P} ANDA experiment pursues a high luminosity of up to $2 \times 10^{32} \text{ cm}^{-2}\text{s}^{-1}$ in order to acquire high statistics for rare physics channels. Sufficient radiation resilience of the system for a long and stable operation of the experiment must be assured.

4.3 Design

As discussed the Barrel TOF shares its mechanical support with the Barrel DIRC. Therefore it has the same 16-section segmentation structure, with a gap to allow the target pipes to pass, azimuthally around the beam direction. Each of these 16 segments is independent, acting as a standalone detector, and is called a super-module. Super-modules can be inserted into the common support structure with the Barrel DIRC (c.f. figure 4.6). A super-module has the dimension of $2460 \times 180 \text{ mm}^2$ and its thickness is below 20 mm. A super-module includes not only the active detector material in form of scintillator tile modules, but also the readout electronics and the signal transmission lines connecting the tile modules with the readout electronics. Figure 4.7 shows a drawing of one super-module.

Each segment contains 120 scintillating tile modules arranged side by side in two columns, covering an active area of about $1800 \times 180 \text{ mm}^2$ and an azimuthal angle of 22° – 140° . A scintillator tile module, shown in figure 4.8, is made of a plate of plastic scintillator, which converts an energy loss of a passing high energy charged particle into photons, and an array of Silicon Photomultiplier(SiPM) converting photons into a proportional charge. The scintillator material has a thin shape of

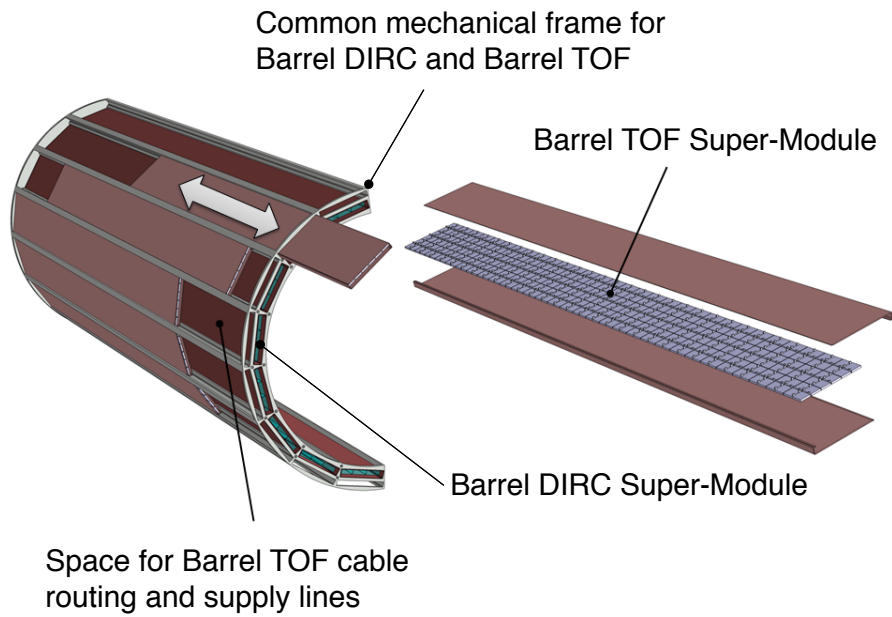


Figure 4.6: Conceptual drawing of the Barrel TOF barrel with the 16-segment super-module structure together with the Barrel DIRC, showing how they could be assembled together and share the mechanical support. In this figure only one half of the barrel with 8-segment is shown.

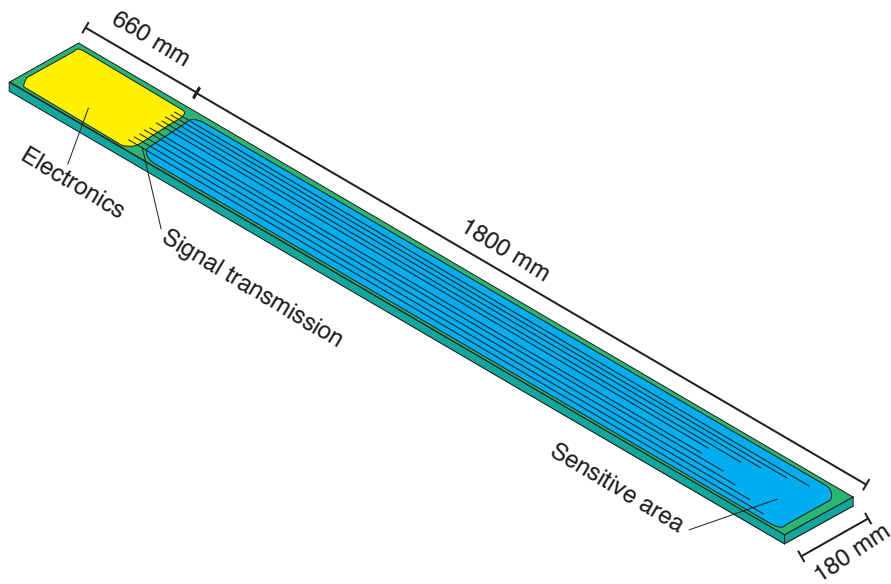


Figure 4.7: A conceptual design of the \bar{P} ANDA Barrel TOF super-module that consists of a sensitive area (light blue), electronics part (yellow) and signal transmission lines in-between them.

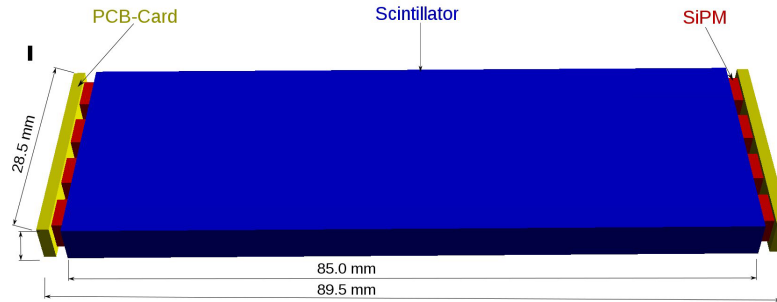


Figure 4.8: A schematic of the plastic scintillator tile module. It measures $87 \times 29.4 \times 5 \text{ mm}^3$. This is slightly smaller than the pitch of $90 \text{ mm} \times 30 \text{ mm}$ due to necessary thickness of the SiPM, PCB board and wrapping materials. The surfaces ($29.4 \times 5 \text{ mm}^2$) at the small ends are covered by 4 SiPMs. Position information along the long axis can be obtained from the time difference of the signals from both sides. The module is first wrapped with reflective material and then with light tight material.

dimensions $87 \times 29.4 \times 5 \text{ mm}^3$, slightly smaller compared to the actual space on the super module due to necessary thickness of SiPM, PCB board and wrapping materials.

The scintillation photons are detected at two ends using 4 SiPMs each, with $3 \times 3 \text{ mm}^2$ sensitive area each. The small sensitive area is one of the limitations of SiPM at the moment, however, multiple SiPMs can be combined into a single channel. With such a technique the sensitive area can be multiplied by a factor of typically 2-5 without increasing the number of readout channels. The 4 SiPMs at each end are placed equidistantly so that the sensors cover the scintillator ends as homogeneously as possible. This and a good light collection efficiency minimizes the hit position dependence of the time resolution. The modules are wrapped with aluminized mylar foil as a reflective material in addition to a black wrapping to make the detector light tight. The time resolution in σ in lab measurements for such a scintillator tile module is about 54 ps [37]. The position information along the long axis can be obtained from the time difference of signals between both ends. The value obtained for the position resolution is 5.5 mm in σ . Two of such modules form a dual-module which is mounted all together on the super module using 4 MMCX connectors as shown in figure 4.9. In total the whole barrel will

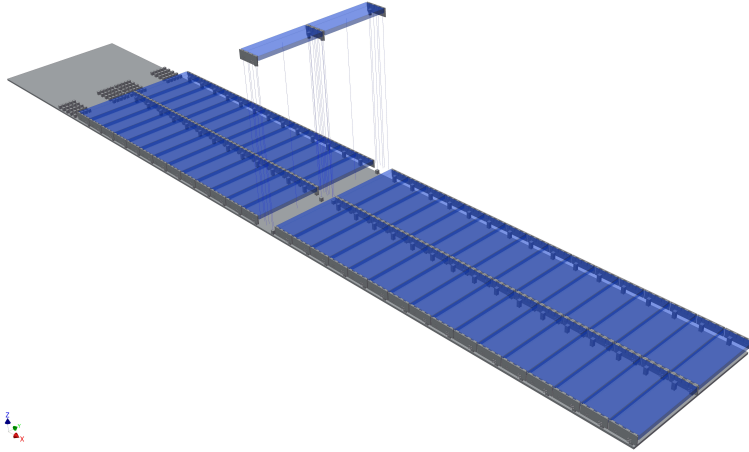


Figure 4.9: A 2×60 matrix array of scintillator tile modules is mounted on a super-module. Sensors are aligned in three lines, both sides of the long axis of the super-module and in the middle. Two scintillators are connected at the $30 \times 5 \text{ mm}^2$ surface with a double-sided sensor-module. Therefore a super-module furnishes 60 dual-modules. The figure depicts also an assembling procedure of a dual module onto a super module. One dual-module is mounted on a railboard with 4 MMCX connectors.

be equipped with 1920 scintillating tiles, 3840 readout channels and 15360 SiPMs.

The front-end readout electronics (FEE) are concentrated at the back end of the super module. The FEE amplifies and digitizes the signal from the photo sensors and transfers the data to the \bar{P} ANDA computing node. With the concentrated FEE design at the end of the board in backward direction, the average material budget is kept low over the super-module surface. The expected hit rate is reduced in the FEE area, i.e. radiation exposure, is lower. The radiation hardness requirements on the electronic circuits are eased accordingly. Figure 4.10 shows the result of my simulation studies on the expected hit rates in the Barrel TOF for background events using the DPM generator.

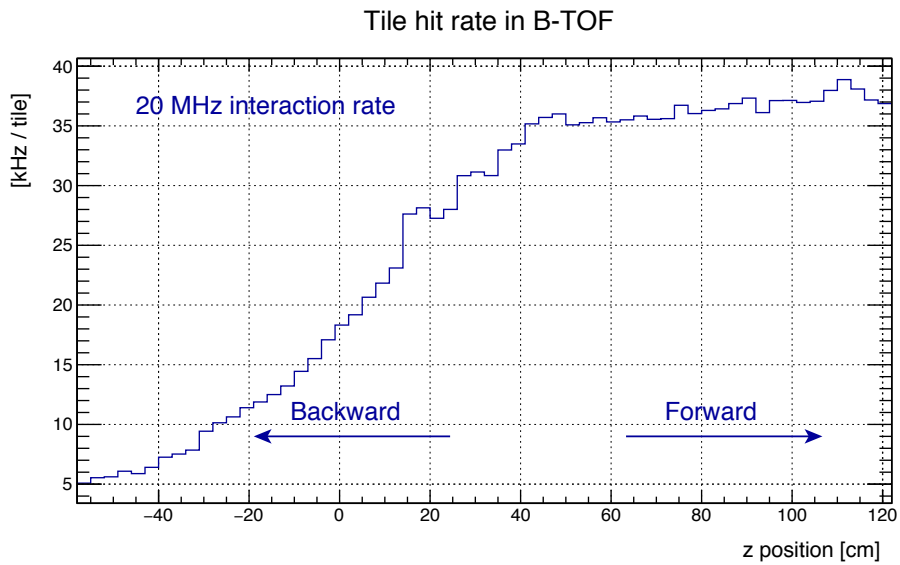


Figure 4.10: Expected hit rates per scintillator tile as a function of the tile z position with an average hit rate of up to 39 kHz in the forward region and an overall average of about 27 kHz. The calculation is based on a simulation using the DPM event generator with an average interaction rate of 20 MHz. The FEE position actually is between $Z = -80$ to -60 cm, outside of the range shown here. The radiation exposure is about one order of magnitude lower than in the forward region.

5 Barrel TOF optimization studies

In order to investigate the performance of the Barrel TOF within the final experiment simulation studies were required. A realistic implementation of the Barrel TOF detector components and their response to passing particles was implemented in the PandaRoot framework. Two different design options were simulated to support the optimization of the detector layout. This chapter will discuss the implementation of the Barrel TOF in the simulation framework Pandaroot and the simulation results on the efficiency studies for the mentioned designs. My work presented in this chapter is also discussed in the “Technical Design Report for the PANDA Barrel TOF”[13]

5.1 Implementation of the Barrel TOF

As discussed in section 3.3 a full simulation in PandaRoot is divided into five main stages: simulation, digitization, reconstruction, particle identification and analysis. Since the first two stages simulates the detectors hardware response, for which a deep knowledge about the detector in the specific environment and readout system is required, every subdetector system must be implemented individually in Pandaroot by the corresponding group with expertise. The implementation of the Barrel TOF in the simulation and digitization stage of Pandaroot is described in the following section. Further informations on the developed and implemented reconstruction and particle identification algorithms are described in chapter 6

Geometry

The simulation stage can be split into describing the detector geometry, generating the primary particles and the transporting the simulated particles through the

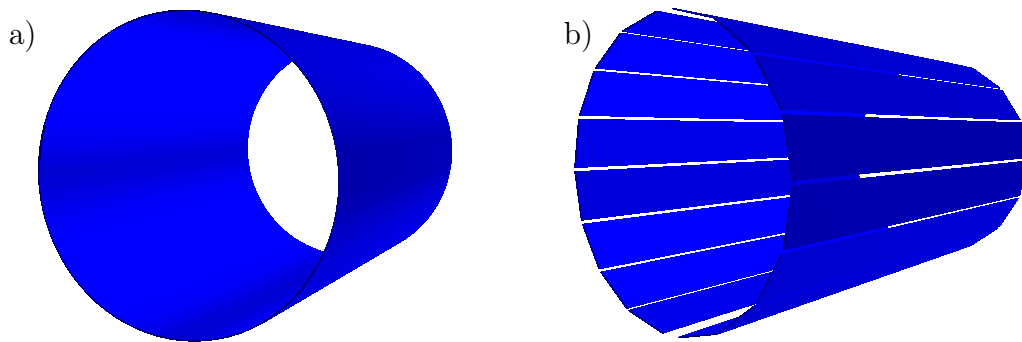


Figure 5.1: For simulation studies different variations of the Barrel TOF are implemented in PandaRoot. a) Reference geometry, represented by a single continuous cylinder without any dead area. b) Geometry consisting of 16 perfect super-modules without any gaps within a super-module.

detector. The Barrel TOF geometry is described using the geometry classes provided by the basic ROOT framework. I created specific macro files for the ROOT framework, which can be executed to generate the geometry files describing the Barrel TOF designs for the simulation stage of PandaRoot. These predefined detector designs can be loaded at the beginning of the simulation stage. As part of my work for this thesis the geometry macros were updated many times in order to represent the current status of the project. In addition to the implementation of the current Barrel TOF design, simple and therefore unrealistic designs of the detector and design prototypes were implemented to perform optimization studies. Figure 5.1, 5.2 and 5.3 show drawings of some implemented geometries, generated within the root framework. The order of subfigures does not represent the time line of the project but different complexity levels of realism.

The first geometry (Fig. 5.1a) represents an ideal detector of a single continuous cylinder and served as a reference for various studies. The cylinder has an inner radius of 503 mm, a length of 1800 mm and a thickness of 5 mm. It is completely built up of active scintillator material without any electronics or support structure. The active area of this detector is about 5.7 m². For the simulation studies it is located at the same position as the realistic geometries. Therefore it has a 100 % geometrical efficiency within the given laboratory angles that is in reality reduced due to support structure and other PANDA detector materials. The second geometry (Fig. 5.1b) is built up by 16 super-modules with perfect efficiency. This geometry takes into account the restrictions by other sub detector systems and support structures. However, it also consists only of sensitive material, perfectly filling the available space without fitting sensors and electronics and provides an active area of 5.2 m². Figure 5.2b) shows a realistic design option which includes

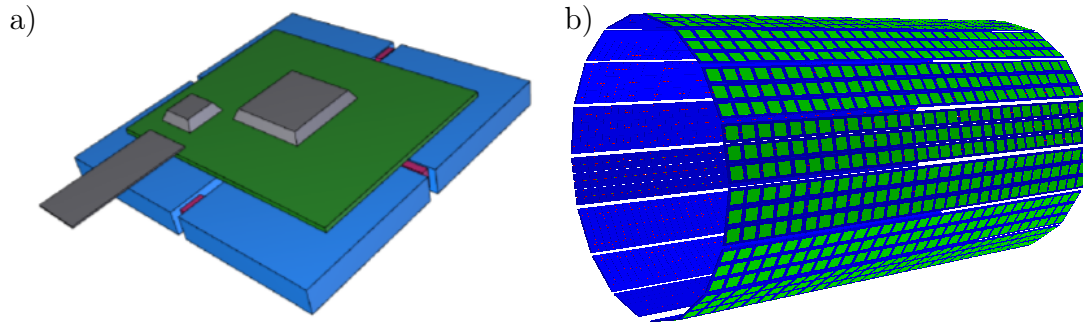


Figure 5.2: a) The implemented realistic design option A is build off modules including 4 scintillating tiles (blue), 8 SiPMs (red) and a PCB board with the readout electronics attached (green and grey). b) The full barrel according to design option A.

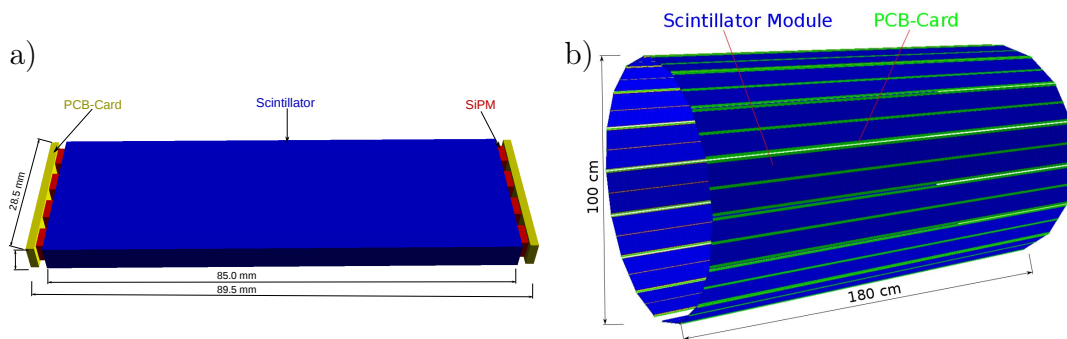


Figure 5.3: a) The dual-module design of the final design (Design option B). Its consisting of a scintillation tile (blue) read out by 8 SiPMs (red) and connected via a PCB board (yellow). b) The implemented full barrel for design option B which corresponds to the final Barrel TOF design. In green the PCB rail-boards transmitting voltage and signal to the FEE are indicated.

gaps and blind spots to fit support structures, SiPM sensors and electronics as well as the space constraints due to other detector systems. This realistic design option A corresponds to the geometry originally proposed for the Barrel TOF [1]. As before the blue colored area indicates the scintillating material. The green material represents PCB boards for the readout. The single scintillator tiles which are arranged in groups of 4 into so called quad-modules (cf. figure 5.2a). In between these tiles SiPMs are placed, represented in red. In total 5760 scintillating tiles of size $28.5 \times 28.5 \times 5 \text{ mm}^3$ resulting in an active area of 4.7 m^2 are included. Nevertheless this design A is still partially idealized, namely there are missing gaps between the scintillating tiles for the wrapping material and no PCB board connectors for the SiPMs are included.

The last design reflects the most up-to-date design of the Barrel TOF which is presented in chapter 4. As shown in figure 5.3a the $87.0 \times 29.4 \times 5 \text{ mm}^3$ scintillating tiles were equipped with 4 SiPMs on each side. According to the described super-module structure, 120 of these modules are assembled including sensor boards for the serial connection and PCB railboards for the transmission of the signals to the FEE. Space for the wrapping material is considered, however the material can be ignored safely in this simulation. Figure 5.3b shows the fully implemented Barrel TOF with a sensitive area of 4.9 m^2 . The support structure is shared with the Barrel DIRC detector. Therefore it is part of the Barrel DIRC implementation in PandaRoot and not covered by this implementation. The Root macro to build this latest design of the Barrel TOF is accessible in the PandaRoot repository:

```
PandaRoot/macro/scitil/geometry/create_scit_rootgeo_201601.C.
```

The binary geometry file is located at

```
PandaRoot/geometry/SciTil_201601.root.
```

Simulation

As described in section 3.3 in the simulation stage, generated particles are transported through the detectors using Monte-Carlo engines. The sensor boards, the railboards, and the SiPMs are only passive materials in the detector simulation, whereas the scintillating tiles are active. Track and particle data are monitored when a particle enters and exits the tile, i.e. event ID, Track ID, entry and exit position and momentum, entry time, track length, and energy loss. Event and track IDs can be used in the analysis to get access to the full Monte-Carlo information on the particle generation. The data are discarded if the total energy deposit of a particle in the scintillator is below a threshold of 100 keV. This corresponds to 1/10 of the energy deposit of a MIP, which is about 1 MeV. According to the last

test beam measurements, an energy deposit below this threshold will create less than 10 detected photons. This is probably hard to distinguish from noise in the real experiment. This cut ensures that low energetic particles in the Barrel TOF don't slow down the simulation and still gives a good enough approximation. The following lines of code show how to load the Barrel TOF in the simulation macros of PandaRoot and set the variable and optional parameters(i.e. geometry file and threshold).

```

1 //----- B-TOF -----
2 PndSciT *SciT = new PndSciT("SCIT",kTRUE); //load the B-TOF module
3 SciT->SetGeometryFileName("SciTil_201601.root");
4 SciT->SetThreshold(0.0001); //set threshold in GeV.
5 fRun->AddModule(SciT); // activate the module

```

Digitization

In the digitization stage the detector electronics response simulated. The classes for the Barrel TOF digitization implementation were created and updated during the progress of this thesis many times to reflect the status of the PandaRoot evolution as well as the detector development. The primary class for the digitization is called “PndSciTDigiTask“ which handles the signal processing for the event-based as well as for the time-based digitization. The electronics of the Barrel TOF is simulated in a simplified way in the current version due to two reasons. First the scintillation photons are not simulated individually to save a computing resources. Second the FEE development is not yet complete and some minor changes might be expected. The implemented digitization class describes a realistic signal output according to test beam results which were performed in the last years. For every recorded signal stored in the simulation stage the exact timing information is used to generate realistic signals for both readout channels per scintillator.

For that purpose the timing information is smeared randomly using a Gaussian distribution with a standard deviation of $75 \times \sqrt{2}$ ps. This 75 ps single tile time resolution is slightly above the value of 54 ps achieved in test beams to ensure conservative results in the simulation. The factor $\sqrt{2}$ takes into account the slightly higher time resolution of the individual channels. Additionally an estimation for the photon propagation to the SiPMs is taken into account. It uses the hit position in the tile and an effective speed of light of $v_{\text{eff}} = 1.01 \times 10^8$ m/s for the photons, measured at beam tests [13]. This approximation is necessary to skip the simulation of the scintillation light and the single photon propagation.

The timestamps obtained in that way are subsequently processed likewise a realistic readout electronics can handle them. The two timestamps per particle and scintillating tile are used to calculate an average time stamp and the time difference between the separate channels. The time difference combined with the effective speed of light in the material is used to gather a position information on the detected particle along the 90 mm side with a resolution of about 5.5 mm in standard deviation. In the final experiment this method may be updated according to the FEE development. The processed signals are kept in a buffer. For the event-based digitization a Barrel TOF signal is crosschecked with all remaining Barrel TOF signals from that event. If more than one particle crossed the scintillator within the set pile-up time, the following hits pile-up, namely the energy deposits are summed up, attributes it to the first hit and discard the hit. The reason therefor is that the FEE can not separate overlapping signals, and simply integrates the combined signal above a certain threshold to evaluate the energy deposit. If particles cross the scintillator after the pile-up time but within the dead time of the DAQ, needed to process the signals, the hit is simply discarded. The standard values for the signal pile-up time is 10 ns and for the dead time is 1000 ns and can be adjusted for simulation tests or FEE updates. In the time-based operation mode additionally all signals are ordered in time, exceeding the boundaries of the single $\bar{p}p$ annihilation. Instead of checking only a potential pile up with signals coming from the same event, a pile up with every signal within the set detector dead time is taken into account. Figure 5.4 and 5.5 show the number of detected signals in the Barrel TOF as a function of the time stamp for an event based and a time based simulation using the DPM background generator.

The listing below shows the macro code to load and change settings for the digitization stage of the Barrel TOF implementation.

```

1 //-----B-TOF Digitization -----
  PndSciTDigiTask* SciTDigi = new PndSciTDigiTask();
3 SciTDigi->SetVerbose(iVerbose);
  SciTDigi->SetDeadTime(1000); //in ns
5 SciTDigi->SetTimeResolution(75); // in ns
  SciTDigi->RunTimeBased(); // activate timebased mode
7 fRun->AddTask(SciTDigi);

```

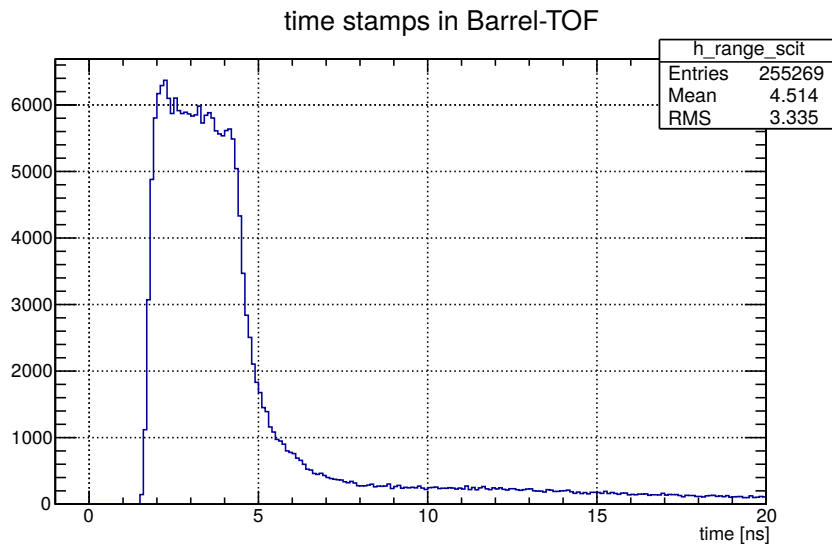



Figure 5.4: Time stamp distribution of detected particles in the Barrel TOF for the event based simulation mode. In this mode every $\bar{p}p$ annihilation takes place at 0 ns.

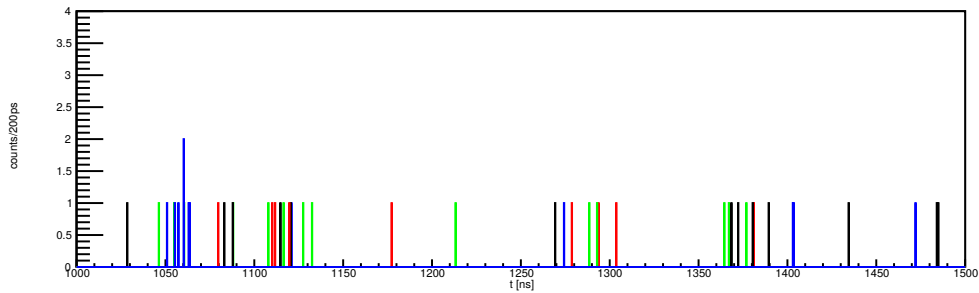


Figure 5.5: Section of a time stamp distribution of detected particles in the Barrel TOF for the time based mode and a simulated average event rate of 100 MHz. Timestamps from the same event are equally colored. Consecutive events are iteratively colored in black, red, green and blue. In this mode every $\bar{p}p$ annihilation get a realistic time information and the corresponding detector signals space out in time.

geometry	number of scintillating tiles	tile size [mm ²]	active area [m ²]
perfect barrel	1	-	5.7
perfect super-modules	16	180 × 1800	5.2
design A	5760	28.5 × 28.5	4.7
design B	1920	86.95 × 29.4	4.9

Table 5.1: Properties of the studied Barrel TOF design options.

5.2 Barrel TOF efficiency studies

In this section the simulation studies on the detection efficiency of the Barrel TOF are presented. During the development of the Barrel TOF two different geometries were studied and their efficiencies were compared to optimize the detector. The two design options were already presented in section 5.1, i.e. the original design (A) and the design proposed in the TDR (B). In 5.2.1 the geometrical acceptance of the Barrel TOF for realistic particle distribution in $\bar{p}p$ annihilations is discussed. In 5.2.2 the detection efficiency of the single tiles is discussed taking into account the capability of the planed electronics. The combined total efficiency of the Barrel TOF system and the impact of the results are discussed in 5.2.3.

5.2.1 Geometrical Efficiency

For this evaluation, the realistic detector geometries were compared to the ideal geometries represented by the single continuous cylinder and the perfect super modules (Fig. 5.1). Table 5.1 summarizes the properties of the implemented geometries. Comparing the design A and B, option B has a slightly larger active area. However, for the particle detection efficiency, the pure active area is not the only important criteria. The \bar{P} ANDA experiment is a fixed target experiment. Therefore the final state particles will have a forward boost, which is more significant for higher primary \bar{p} beam momenta.

Due to this varying momenta and varying impinging angle in the Barrel TOF layer the shape and positions of the gaps in between the active material become also important beside the pure active area.

In order to study the geometrical efficiency with a realistic particle distribution, simulations were performed using PandaRoot. The $\bar{p}p$ events were generated us-

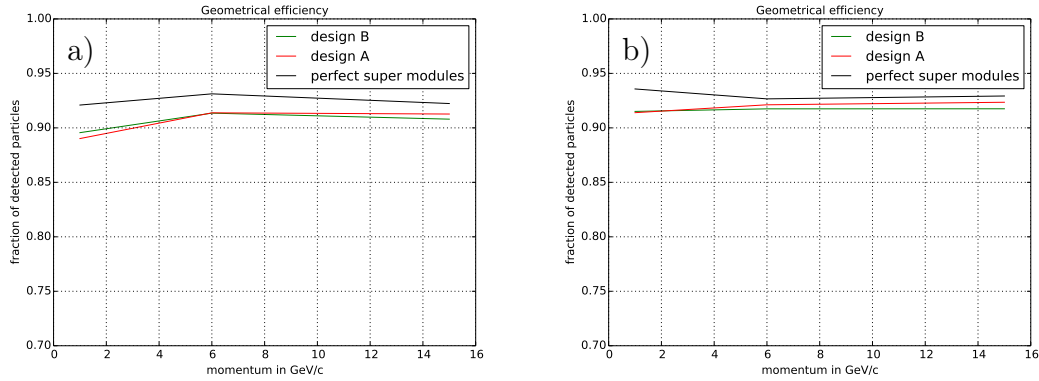


Figure 5.6: Geometrical detection efficiency for primary particles (a) and all particles (b) in comparison to the perfect barrel. For comparison also the results for a detector based on ideal super modules is shown in black.

ing the DPM generator (cf. 3.3.1) at three primary momenta i.e. of 1.5, 6.2 and 15 GeV/c. These are the minimum and maximum planned momenta, and a medium momentum, planned for example for hyperon runs. In addition to the Barrel TOF detector all other detector geometries and materials of the barrel spectrometer up to the EMC were included. This includes also all support structures, implemented at that time in PandaRoot. This ensures an as realistic secondary particle generation and particle distribution in the simulation as possible.

As explained in section 5.1 a minimum energy deposit of a particle in the scintillator is required to detect the particle. This was considered for the realistic geometries as well as for the reference geometries. The detector dead times and signal pile-ups were not taken into account, to study the pure geometrical acceptance. This geometrical efficiency E_{geo} was calculated as the ratio of detected particles in the respective geometry ($\#Hits$) to the number of detected particles in the reference geometry ($\#Hits_{reference}$).

$$E_{geo} = \frac{\#Hits}{\#Hits_{reference}} \quad (5.1)$$

As described above the primary \bar{p} beam momentum has an effect on the detection efficiency. Figure 5.6 summarizes the extracted efficiencies for the two realistic design options as well as for the perfect super modules.

It can be seen that for the, primary particles design A and design B achieve a similar geometrical efficiency between 89.6 % to 90.9 %. Design A slightly favors higher beam momenta and therefore particles emitted in more forward angles. For

comparison also the detection efficiencies for all particles, charged primaries and secondaries and neutrals, are plotted on the right side. The efficiencies of the perfect super-modules show that even with unrealistic and perfect detector only a few more percentage can be achieved. Design A and B are both equally close to the ideal super-module case, namely 92% to 93%. However, design B is realistic also with respect to the implemented sensors, signal lines and wrapping material. Therefore it can be concluded that the geometrical efficiency of design B is already highly optimized.

This results already indicate, that not only the primary momentum has an influence on the efficiency. Especially the production angle of the final state particles is a critical parameter. The efficiencies as a function of the production angles of primaries are shown in figure 5.7 for a primary beam momentum of 1.5 GeV/c, 6.2 GeV/c and 15 GeV/c. Design A and B show a very similar efficiency for low and high production angles. However for particles emitted perpendicular to the primary \bar{p} beam, i.e. production angles of 70°-110° the design B surpasses design A. This can be explained by the structure of the modules. Figure 5.8 shows the structure of a super-module for design A and B. Design B has a slightly higher total active area than design A (cf. table 5.1), but Design B has one gap of 3 mm in the middle compared to Design A with more than one gap of size 1.5 mm. Charged particles enters the scintillator with finite angle due to the bending in the magnetic field and the forward boost. The gap size changes effectively by a track incident angle, which is a function of Pt, and therefore of the beam momentum. For low and high production angles design A strongly profits from that effect while the minimized gaps of design B reduce this influence. For production angles of $\theta \approx 90^\circ$ the full gap size effects the efficiency and design B surpasses design A. Overall design B has a more homogeneous detection efficiency as a function of the emission angle θ .

5.2.2 DAQ Efficiency

Realistic sensors like the used SiPMs have a dead time after a detected hit. This and the time needed to process the signals by the electronics lead to a finite single tile detection rate capability. More than one particles hitting a scintillating tile within a small time window can lead to pile-up of the SiPMs signal. Although this signal pile-up may be identified due to an increased measured energy deposit, the time and position information for the subsequent hits can not be reconstructed. I performed simulation studies to investigate the probability of such multi-hits in a single tile of the Barrel TOF as a function of the DAQ dead time, to determine

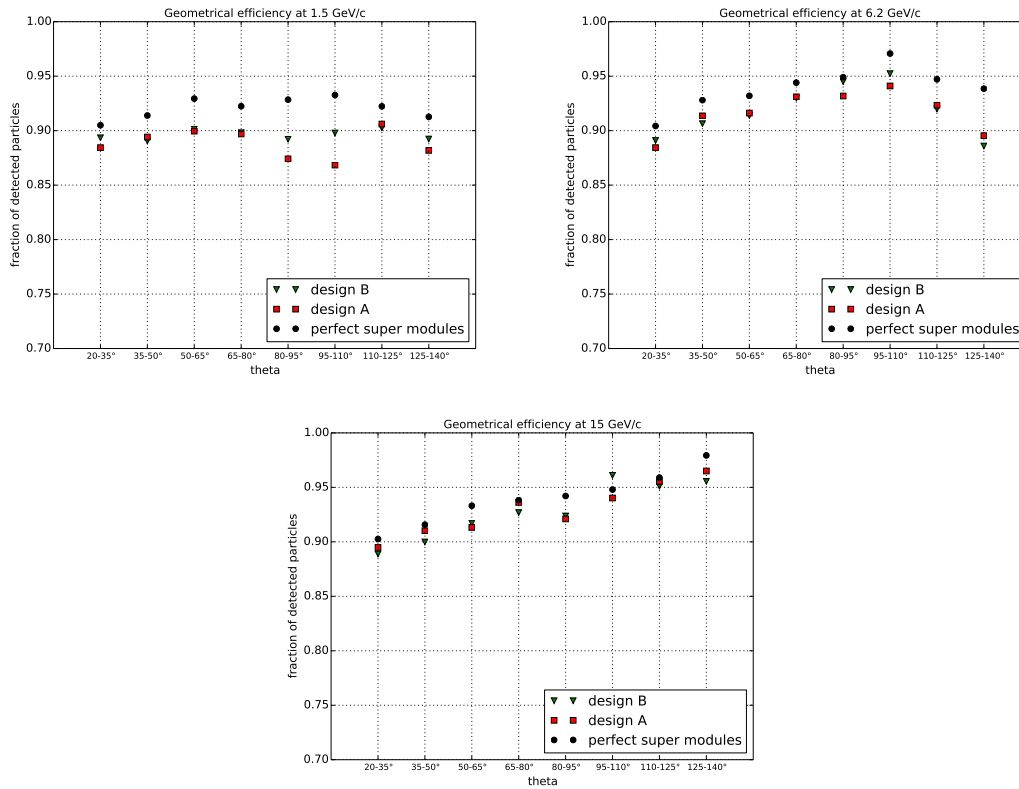


Figure 5.7: Geometrical efficiency for primary particles for the realistic designs in comparison to the reference geometry as a function of the primary particles production angles. Due to the reduced gap size between the scintillating tiles perpendicular to beam direction for design B (green triangle), it achieves a higher efficiency for particles with an emission angle of 65° - 110° then design A (red squares)

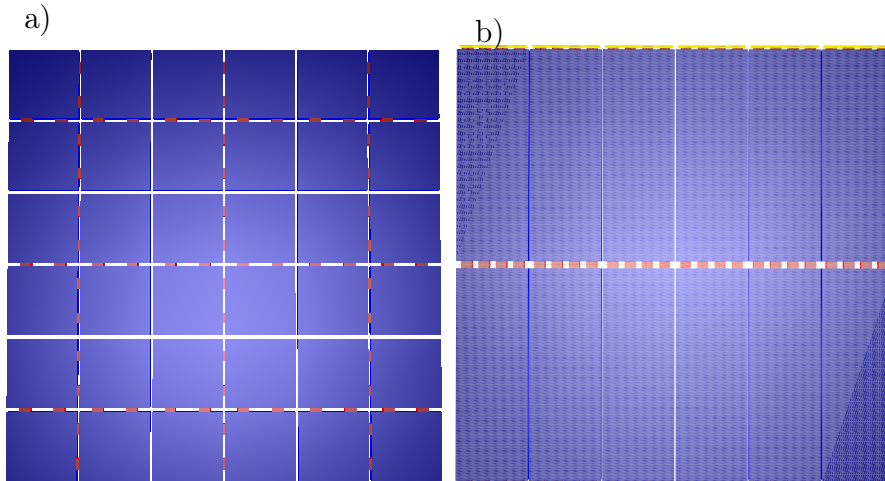


Figure 5.8: Section of the super-modules of design A (a) and B (b). The scintillator are colored in blue, the SiPMs in red and the PCB connector boards in yellow. Major parts of the PCB boards are fade out to reveal the scintillating tile structure. Design A consists of modules of 4 scintillating tiles with equidistant gaps of 1.5 mm in transverse and longitudinal direction. Design B reduces the gaps in transverse direction to a minimum of 0.6 mm but has a bigger gap in in the middle in the longitudinal direction of 3 mm.

the percentage of lost information.

For this evaluation simulation studies the time-based simulation mode was used. The full $\bar{\text{P}}\text{ANDA}$ geometry with either the design option A or B described in section 5.1 was included. For the event generation, the DPM generator was used to produce a realistic particle distribution and an 20 MHz average interaction rate was assumed. The signal processing time of the readout electronic as well as the exact recovery time of the SiPMs were still unknown at the time of that study. Therefore single tile dead time values in a range from 1 ns up to 10 μs were tested. The term dead time is used as a general term for the signal processing time and the recovery time of the sensors in this study.

As distinct from the study on the geometrical efficiency, the hit rates were not compared to a perfect reference geometry. Instead the numbers of reconstructed hits after the digitization stage, simulating the DAQ, were compared to the numbers of particles hitting the Barrel TOF in the simulation stage.

$$E_{DAQ} = \frac{\#Hits_{digi}}{\#Hits_{sim}} \quad (5.2)$$

The efficiency loss due to multiple signals in one tile is affected by the size of the

scintillating tiles only. The results of the study are summarized in figures 5.9 and 5.10.

The efficiency is decreased for design B due to the increased tile size. For DAQ dead times below 100 ns the efficiency saturates. Multi hits in such short time distance are coming from the same event. A much lower, unrealistic detector recovery time < 1 ns is needed to detect and distinguish these particles. For final state particles only, this saturation level is about 100 % efficiency for the smaller design A as well as for design B. Due to the operating principle of the planed FEE, signals separated by more than about 50 ns can be buffered if the DAQ is already occupied. Therefore short peaks in the hit rate can be compensated as long as the average hit rate stays below the the DAQ rat capability. Simulation showed that a maximum hit rate of 40 kHz is expected for design B (cf. 4.10). This is below the rate capability of the planed FEE as known so far. Assuming therefore an effective DAQ dead time of 50 ps, the studied geometries will provide the same performance for primary particles.

Taking into account all particles, similar results are achieved. Below 100 ns the efficiencies saturates. However, electro magnetic showers, and other secondary particles, increase the multi hit probability. The efficiency is therefore decreased to about ≈ 78 % for design A. Design B is effected slightly more, however as shown the primaries are detected with the same efficiency, so the design B is still compatible.

Also the influence of the primary \bar{p} beam momentum on the DAQ efficiency was evaluated. Figure 5.10 shows the results for 1.5, 6.2 and 15 GeV/c \bar{p} beam momenta. For higher beam momenta a slightly reduced efficiency is observed due to an increased particle multiplicity and a less homogeneous distribution. Simulation studies showed also an increased particle multiplicity in the Barrel TOF for a low primary momentum of 1.5 GeV. However, the more homogeneous particle distribution leads to an increased efficiency per scintillating tile. Nevertheless this study also shows that for a detector dead time of 50 ns the efficiency already starts to saturate and the difference is negligible.

5.2.3 Combined Efficiency

The studies presented in this sections showed that investigated realistic design options slightly differ under various conditions. Design B, provide a larger sensitive area. Due to the forward boost of the particles in combination with the distribution of the insensitive gaps design A still slightly exceeds design B in the average

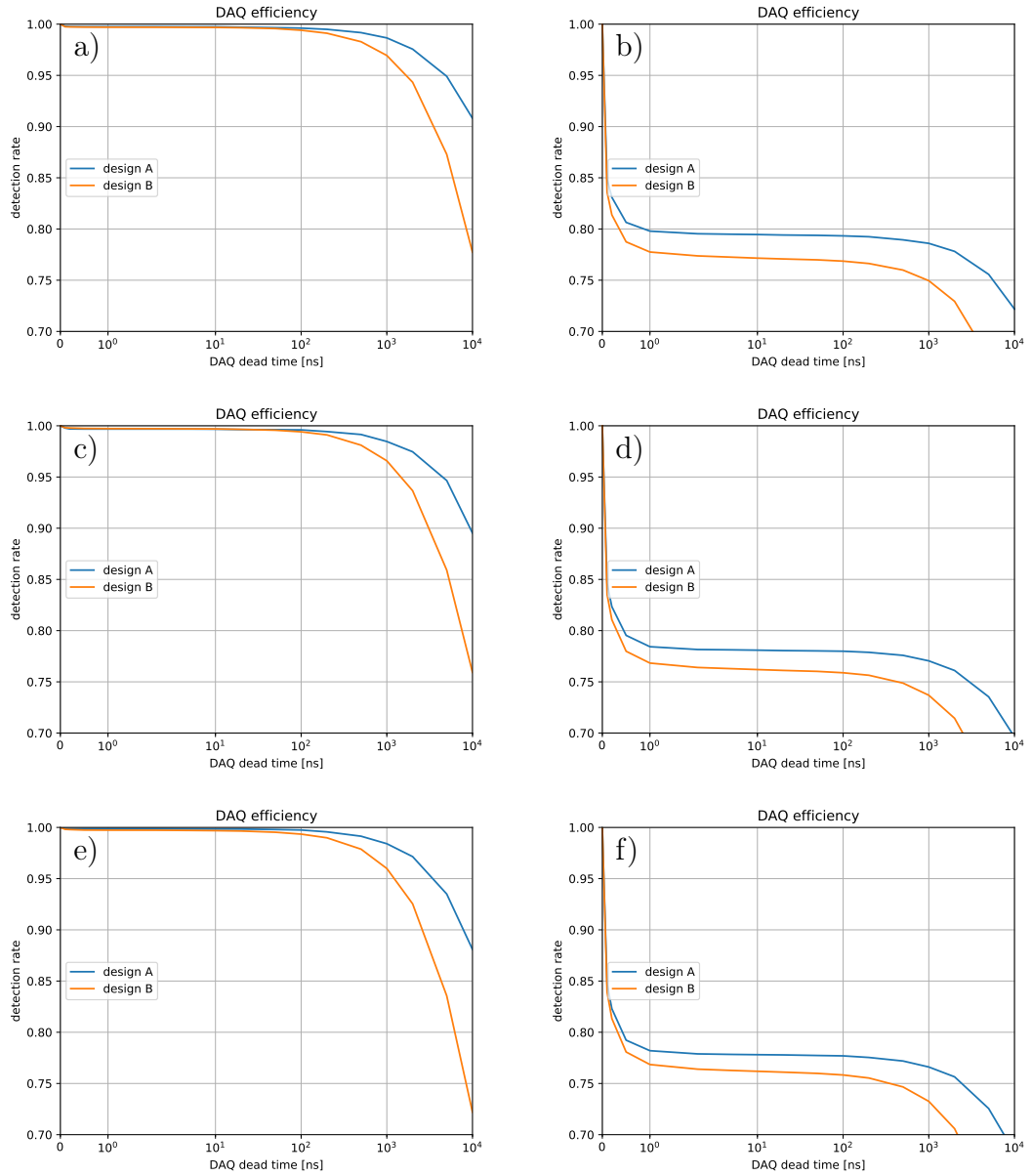


Figure 5.9: DAQ efficiency as a function of the DAQ dead time for the two design options. The first column (a,c,e) shows the detection efficiency for primary particles. The second column (b,d,f) the efficiency for all particles. 1.5 GeV/c (a,b) , 6.2 GeV/c (c,d) and 15 GeV/c (e,f) primary momenta were evaluated. The smaller sized tiles of design A (blue) are in general less affected by the multi-hit probability than design B (orange). However, for the expected effective dead time of about 50 ns the values are equal for primaries due to saturation effects.

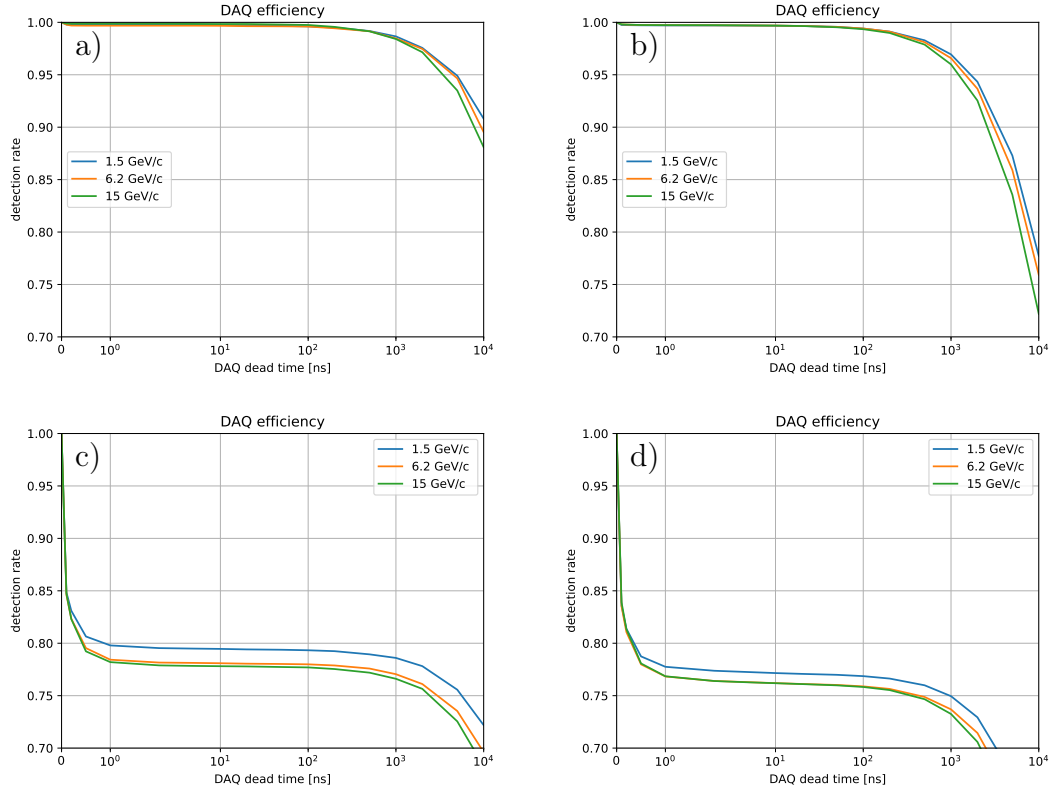


Figure 5.10: The DAQ efficiency for beam momenta of 1.5, 6.2 and 15 GeV/c are shown. The left column describes design A, the right column design B. The efficiency for primaries only is shown in the first row and for all particles in the second row. The efficiency is increased for lower momenta due to a reduced particle multiplicity and a more homogeneous distribution of particles. For the expected effective DAQ dead time of 50 ns this effect is negligible and a stable efficiency of 99.6 % is reached for primary particles.

geometrical efficiency for high primary beam momenta. However, the efficiency of design B is more homogeneous distributed over the whole detector and momenta. One drawback of the increased tile size of design B could be the increased multi-hit probability within the DAQ dead time. However, it was shown that even in the high luminosity mode the planed FEE will not suffer from this problem. Table 5.2 summarizes the detection efficiency for primary particles for a \bar{p} beam momentum of 6.2 GeV/c and an expected effective DAQ dead-time of 50 ns and The differ-

geometry	number of tiles	tile size mm ²	active area m ²	geometrical efficiency	single tile efficiency	total efficiency
perfect barrel	1	-	5.7	-	-	-
perfect super-modules	16	180 × 1800	5.2	93.2 %	-	-
design A	5760	28.5 × 28.5	4.7	91.4 %	99.6 %	91.0 %
design B	1920	86.95 × 29.4	4.9	91.4 %	99.6 %	91.0 %

Table 5.2: Summary of the studies on the efficiency for 6.2 GeV/c beam momentum and 50 ns DAQ dead-time

ence in the combined efficiency is very small. However as explained in chapter 4 the design B has advantages in the achieved time resolution, the realization of the read-out, the mounting and the construction costs. This study proved that the design B has no significant drawback in terms of efficiency compared to the originally planed design of the Barrel TOF.

6 Barrel TOF performance simulations

In comparison to the chapters above, which are focused on the detector development and respective software implementations and simulation studies, this chapter describes studies on the performance of the Barrel TOF detector for various tasks in the final experiment. Beside actually evaluating the performance, I developed and investigated the discussed algorithms by myself or adapted them to the needs of the \bar{P} ANDA experiment. My work presented in this chapter is also discussed in the “Technical Design Report for the: \bar{P} ANDA Barrel TOF”[13] 4.1

6.1 Event Building

The \bar{P} ANDA experiment has no dedicated start time detector. Therefore the determination of the $\bar{p}p$ annihilation time, called event time or t_0 in this thesis, is challenging. Average event rates up to 20 MHz, a continuous read out, potential event mixing and a missing common hardware trigger complicate the situation. One of the first tasks in the reconstruction chain of \bar{P} ANDA will probably be the event building. Even before the first track reconstruction the signals belonging to one event must be packed together into one package and the corresponding t_0 should be estimated as accurate as possible. Figure 6.1 shows simulated signal time distributions using the time-based mode for some detectors in the target spectrometer of \bar{P} ANDA. For detectors with a low time resolution, like Barrel TOF and the EMC, the individual events are most likely separated. For the tracking detector (STT) or the Micro Vertex Detector (MVD) this is not true anymore. However, also the signals in fast responding detectors are not completely separated event by event if late arriving secondary particles are taken into account.

Algorithms, independent from high level information like tracking or PID, are an important first step for the reconstruction stage to prepare the data for the following processing. The TOF counters, i.e. Barrel TOF and FTOF, provide

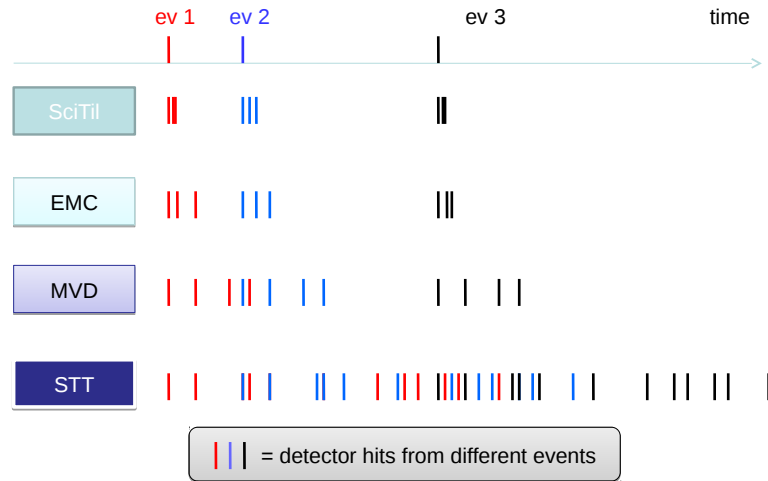


Figure 6.1: Detector signals for different subsystems are shown on a time line. For the Barrel TOF (named as SciTil) the signals arrive most likely event by event. However, for the tracking detectors the events overlap.[38]

timing information of charged particles with very high accuracy without the need for reconstructed track parameters. Therefore the timestamps provided by the TOF counters can be used for an algorithm to estimate the event times and provide informations for the packaging of the data.

The parameters of the signals delivered by the Barrel TOF and other detectors were studied in simulation for the development of an event sorting algorithm. These simulation studies discussed in this section were performed using PandaRoot version 29573. The DPM generator with a \bar{p} beam momentum of 6 GeV/c was used to generate the events. For the time based simulation mode an average event rate of 20 MHz was assumed to simulate the planed high luminosity mode of \bar{P} ANDA

Fig. 6.2 shows a typical timestamps distribution of signals from the TOF counters (Barrel TOF and FTOF) for an event rate of 20 MHz. All timestamps from the same event are equally colored. Consecutive events are iteratively colored in black, red, green and blue. On the negative y-axis the Monte Carlo event time is indicated. The first timestamp from the TOF counters of an event always has a small offset compared to the event t_0 due to the flight time of the particle. The width of a single event can exceed 50 ns. Therefore even in the TOF counters the events are

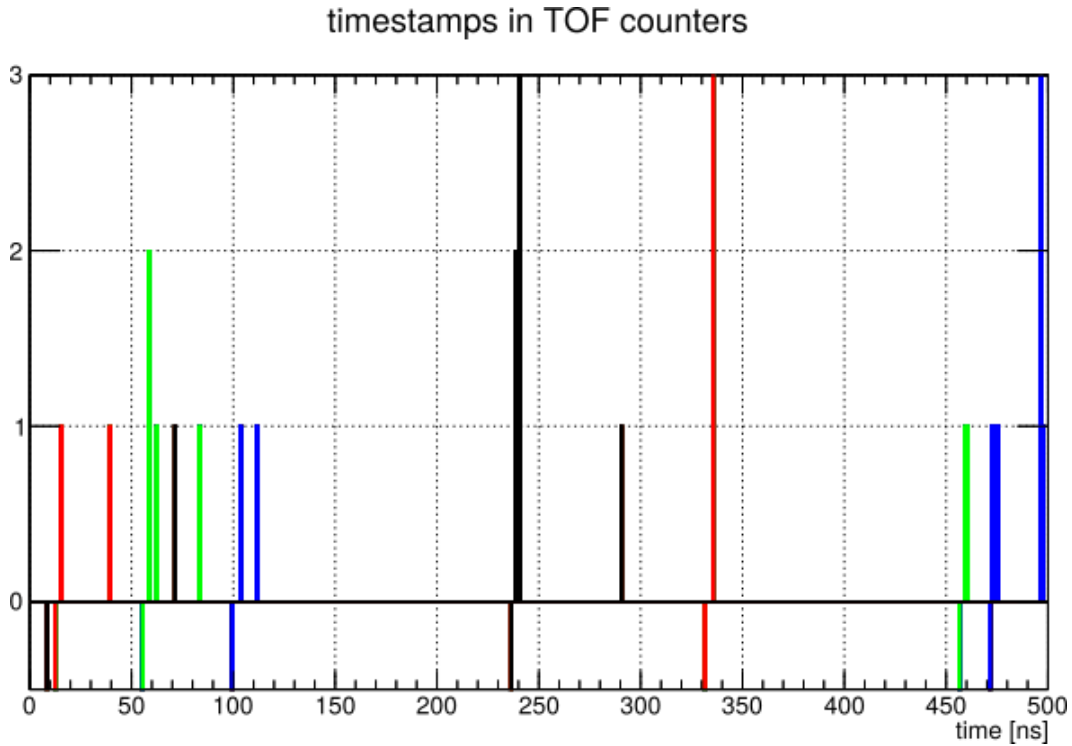


Figure 6.2: Timestamps detected in TOF counters at an average $\bar{p}p$ interaction rate of 20 MHz. On the negative y-axis the Monte Carlo event time is indicated. All timestamps from the same event are equally colored. Consecutive events are iteratively colored in black, red, green and blue.

not clearly separated and a small fraction of events may overlap. Apart from the difficulty of determining the individual t_0 for such mixed events, the final event-packages must contain all the data pertinent to an event. However, the additional amount of wrong matched signals sorted in an event-package should be reduced to a minimum to improve the performance of the online and offline reconstruction, the software filter and the later analysis of the data.

6.1.1 Event Structure

First timestamp distribution in the Barrel TOF for the background was evaluated performing an event based simulation of 10^5 DPM events (cf. Figure 6.3) This diagram revealed three critical parameters. The rise of the distribution is shifted due to the flight time of the particles by some ns. No dedicated peak is evident, but majority of the signals are detected in a finite time window. A long tail is present

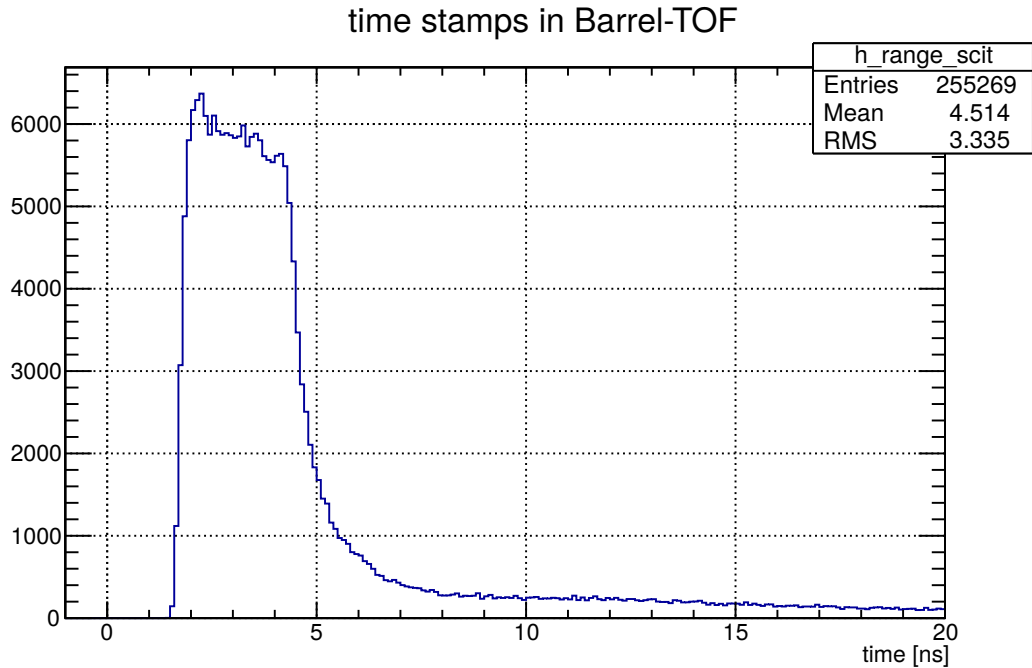


Figure 6.3: The event based timestamp distribution of the Barrel TOF is shown for 10^5 DPM events. The starting point of the distribution is shifted due to the minimum time of flight of particles and the long tail represents late arriving, possible back scattered particles. In total about 2.5×10^5 signals are detected.

which represents late arriving particles. These particles are hard to handle in an event building algorithm, especially without any tracking information. These late particles have an increased possibility of mixing with subsequent events. To ensure that all signals of possibly late particles would be included in the corresponding event package, the time wise width of an event package would need to be far greater than 50 ns. This extended time window dramatically increases the possibility of event mixing.

I studied these late signals and the corresponding particles. It turned out that various processes are causing this tail, however the contribution differ a lot. The most prominent source for this late signals are neutrons or secondary particles, created by neutrons. These neutrons are not directly emitted from the interaction point into the acceptance range of the Barrel TOF, but backscattered from outer detector regions into the target spectrometer. Therefore the flight times are long compared to particles emitted directly into the acceptance range of the Barrel TOF. In figure 6.4, showing the event display of PandaRoot, charged tracks are

emitted directly into the Barrel TOF producing fast signals. However, also very delayed signals are present, caused by a neutron backscattered from the forward spectrometer. Beside neutrons also photons can be emitted backwards from the forward spectrometer into the barrel region. Figure 6.5 describes a sample event with a photon triggering a late signal in the Barrel TOF. Compared to backscattered photons and neutrons typical backscattered, or backwards emitted, hadrons have a short mean free path length. Therefore also the potential delay of such particles is reduced to about 20 ns as shown in figure 6.6. Also the detection rate of such backscattered hadrons is lower compared to photon and neutron induced signals. The last studied category were late signals caused by long interaction and decay chains. Figure 6.7 picture an event with a proton interacting with detector material and producing a π^+ . This is causing a μ^+ in an interaction which is decaying into an e^+ at some point which is finally detected in the Barrel TOF. The timestamps of such signals often exceed more the 500 ns and goes up to the μ s region.

To summarize the results of the study on late detected signals figure 6.8 breakdown the same timestamp distribution as figure 6.3 with a logarithmic y-scale. The red colored area shows the distribution for all detected signals whereas the green colored distribution describes the signals connected to primary particles directly emitted into the Barrel TOF acceptance range. It is evident that primary particles only contributing to the peak of the structure. Starting from about 15 ns the majority of signals are related to neutrons, which is indicated by the blue colored area. Independent of the creation process these late detected tracks are probably very difficult to reconstruct, because the particles are either backscattered or their points of creation are very displaced. Additionally the huge delays of the corresponding signals in any detector system make a proper assignment to a specific event nearly impossible. However, the various intensive interactions of the corresponding particles with detector material make their signals hardly usable for physics analysis. Thus, it is important and sufficient to focus on signals of particles directly emitted in the acceptance range of the Barrel TOF instead of including all signals of an event at all costs.

To decide on the interesting region of signals in the timestamp distribution the peak like structure in figure 6.8 was evaluated. The minimum time-of-flight for a direct, primary or secondary, particle is 1.66 ns as apparent from figure 6.8. This value was also validated by calculations, assuming a particle traveling with the speed of light and the shortest possible track length from the interaction point to the Barrel TOF of about 50 cm. For the calculation of the maximum time-of-flight for direct particles a minimum transverse momentum (p_t) had to be assumed. In the magnetic field of 2 T inside the target spectrometer a particle needs at

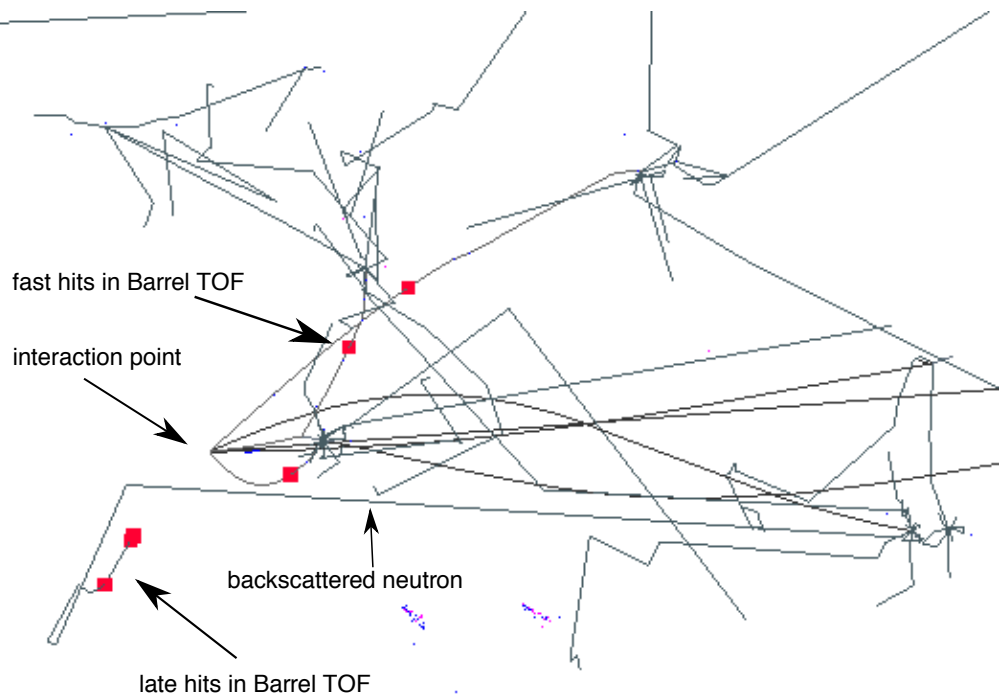


Figure 6.4: Typical event with a back scattered or emitted neutron causing late hits in the Barrel TOF. Three charged tracks are directly going into the Barrel TOF and produce fast arriving signals. The signals in the left bottom corner are related to neutrons, backscattered from the forward spectrometer

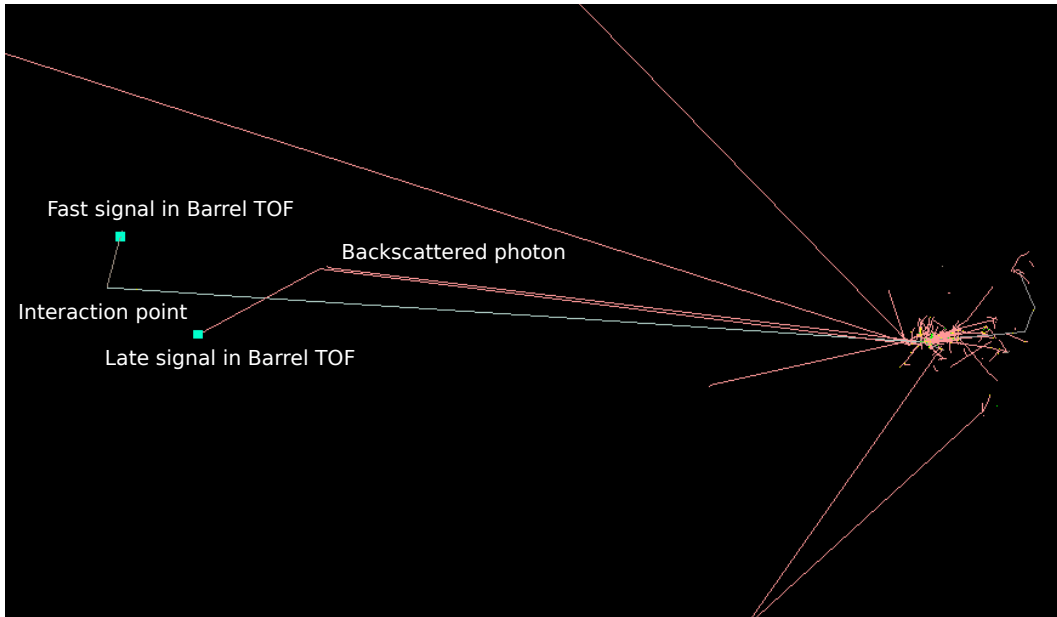


Figure 6.5: Event with a fast signal in the Barrel TOF triggered by a charged primary particle and one late signal caused by an photon emitted backwards from the forward spectrometer

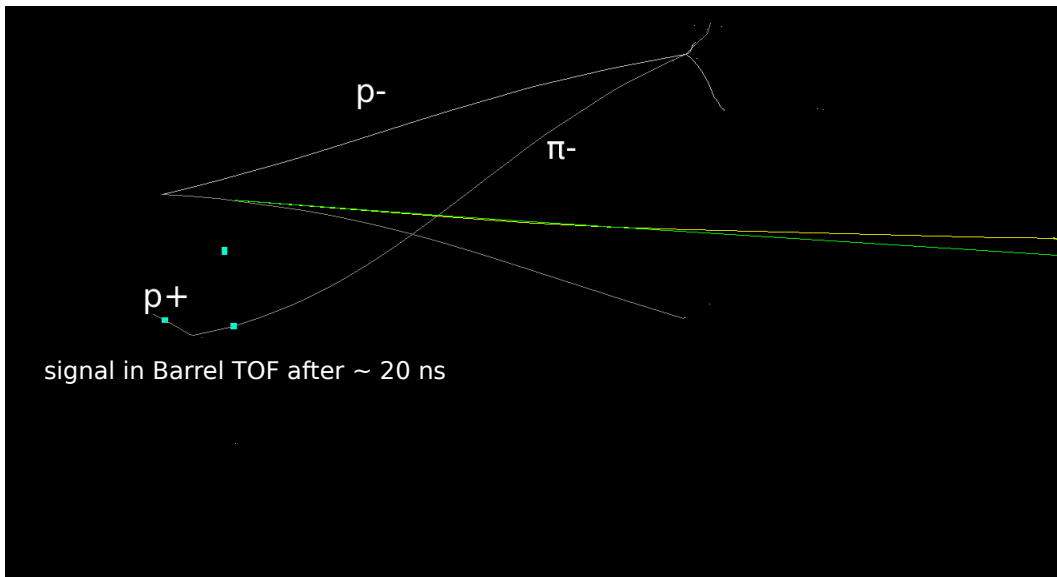


Figure 6.6: In the shown event an emitted \bar{p} interacts with an outer detector part and a produced π^- is emitted backwards into the Barrel TOF. The signal is registered late, about 20 ns after the $\bar{p}p$ annihilation.

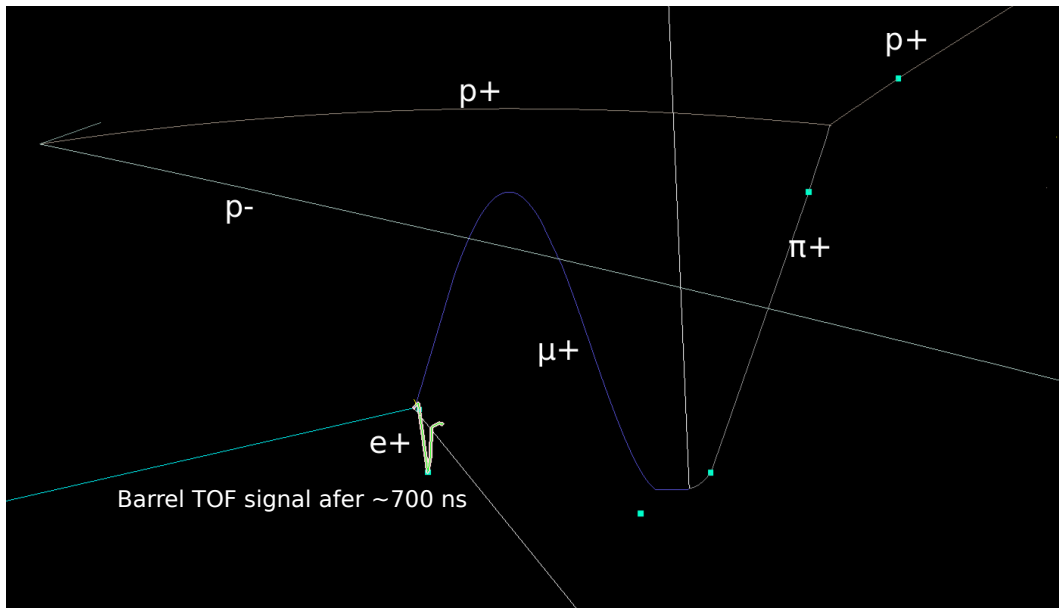


Figure 6.7: If a long interaction or decay chain is experienced, maybe including emission products of excited detector material, very late signals may be detected in the Barrel TOF. In the shown example a $p \rightarrow \pi^+ \rightarrow \mu^+ \rightarrow e^+$ interaction and decay chain produces a signal after about 700 ns.

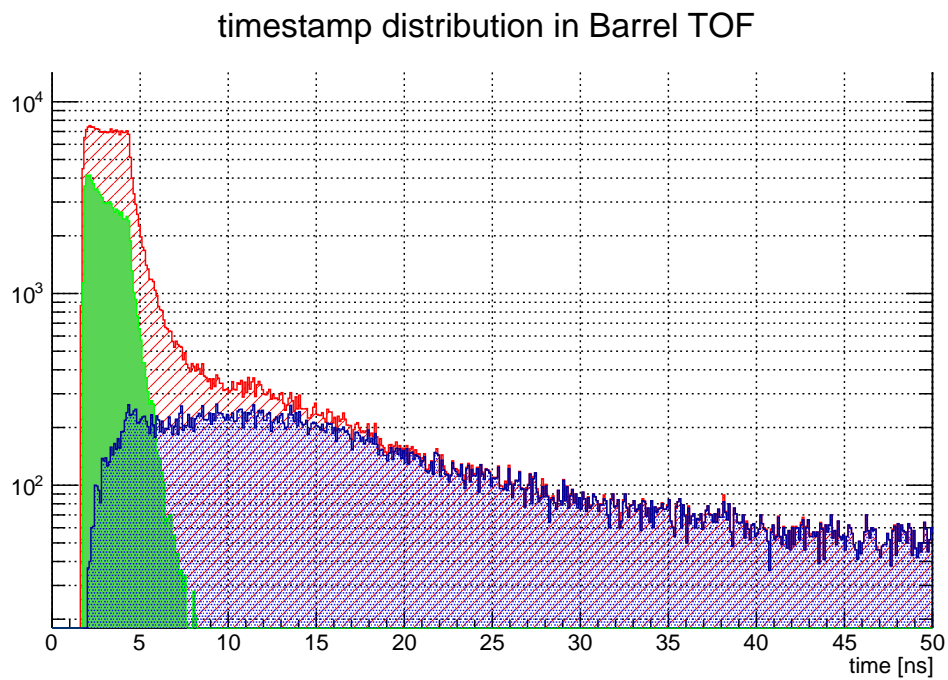


Figure 6.8: The signal distribution in Barrel TOF as shown in figure 6.3. The distribution of signals caused of primary particles is colored in green. Signals initiated by neutrons are colored in blue and are responsible for most of the signals delayed by more than 20 ns. The combined signal distribution is colored in red.

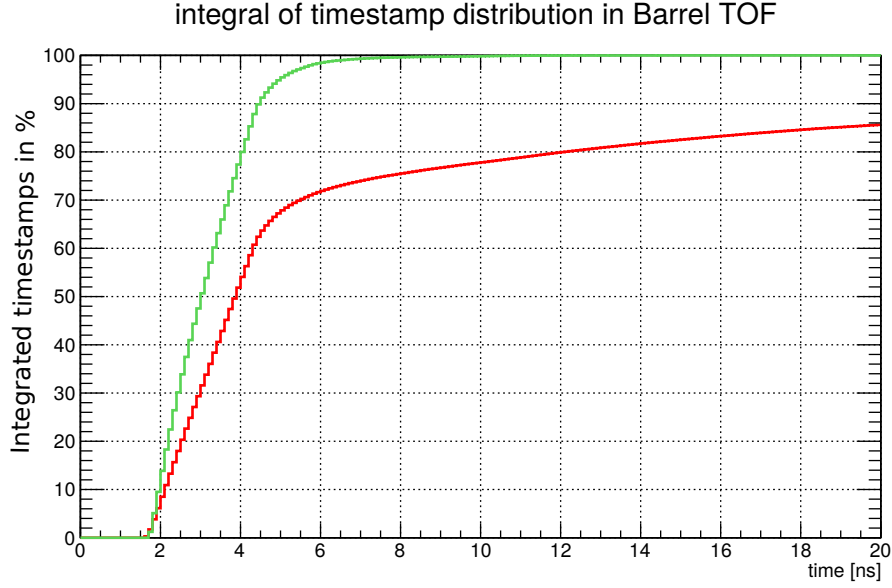


Figure 6.9: Integrated timestamp distribution in the Barrel TOF in percent. Signals of all particles (red) and of primary particles only (green) are indicated.

least about $p_t=150$ MeV/c transverse momentum to reach the Barrel TOF. This results in a time-of-flight of 16.6 ns. Considering the energy loss of particles in the inner tracking detectors the minimum transverse momentum must be even above 150 MeV/c. Therefore the effective maximum time-of-flight is even below. Particles with a $p_t > 300$ MeV/c which are reconstructible with a high quality (cf. section 2.3) are certainly included within this range.

Therefore a reasonable event width in the Barrel TOF is 15 ns, from 1.6 ns to 16.6 ns. Figure 6.9 shows the simulation results for the integrated timestamp distribution in the Barrel TOF. The green line indicates the integrated timestamp distribution for primary particles and confirms the calculations of the arrival times between 1.6 ns and 16.6 ns.

For a proper event sorting and t_0 determination it is advantageous to correct the described offset of the Barrel TOF timestamps, evident in figures 6.2 and 6.3. This offset is varying for the signals depending on momentum and track length. Both quantities are not available at this stage. However, subtracting an estimated time-of-flight from the measured timestamp is a fast method to correct the offset. As a first order approximation, it can be assumed that the detected particles travel at speed of light on a straight path from the interaction point to the scintillating

tile of the Barrel TOF. The time-of-flight can be calculated using the following formula where t is the measured timestamp and l the length of the flight path.

$$t_{corr} = t - \frac{l}{c} \quad (6.1)$$

Figure 6.10 presents the timestamp distribution and integrated timestamp distribution in the Barrel TOF after this speed-of-light correction. The offset of the distribution vanished and the full width at half maximum (FWHM) was significantly reduced. An evaluation of the integrated distributions showed that over 99% of the primary particles arrived at the Barrel TOF within 4 ns. Also 75 % of the combined, primary and secondary, particles reached the Barrel TOF within this 4 ns time window. This structure and boundary values were very important for the development of an event sorting algorithm.

The studies described in this section were also performed on the Forward TOF detector system, and showed comparable results. Especially I proved that a speed-of-light correction performed on the provided FTOF data results in a timestamp distributions equivalent to the Barrel TOF timestamp distribution discussed in this section. Therefore the data provided by the TOF detectors can be combined to increase the statistics and therefore the reliability of algorithms discussed in the following sections.

6.1.2 Event Determination Algorithm

For a first event sorting and preliminary t_0 determination only timestamps provided by the sub detector systems are available.

Apparent from figure 6.3 an average detection rate of about 2.5 particles per event is expected in the Barrel TOF. Even if the contribution of the Forward TOF detector is taken into account the particle multiplicity per event stays low on average. Figure 6.11 presents the results on the studied combined particle multiplicity of the Barrel TOF and the Forward TOF detector. For 33% of events only one or two particles are detected in the TOF counters. Hence, the particle multiplicity per event in the TOF counters is not high enough to use a signal pile-up for the determination of an event. As a result a priori every detected timestamp in the Barrel TOF is potentially indicating a new event. However, as described in the results of the study on the event structure (cf. section 6.1.1), timestamps following each other in a time window of 15 ns are potentially carrying important information of the same event. Hence these data must be put together into one event package for

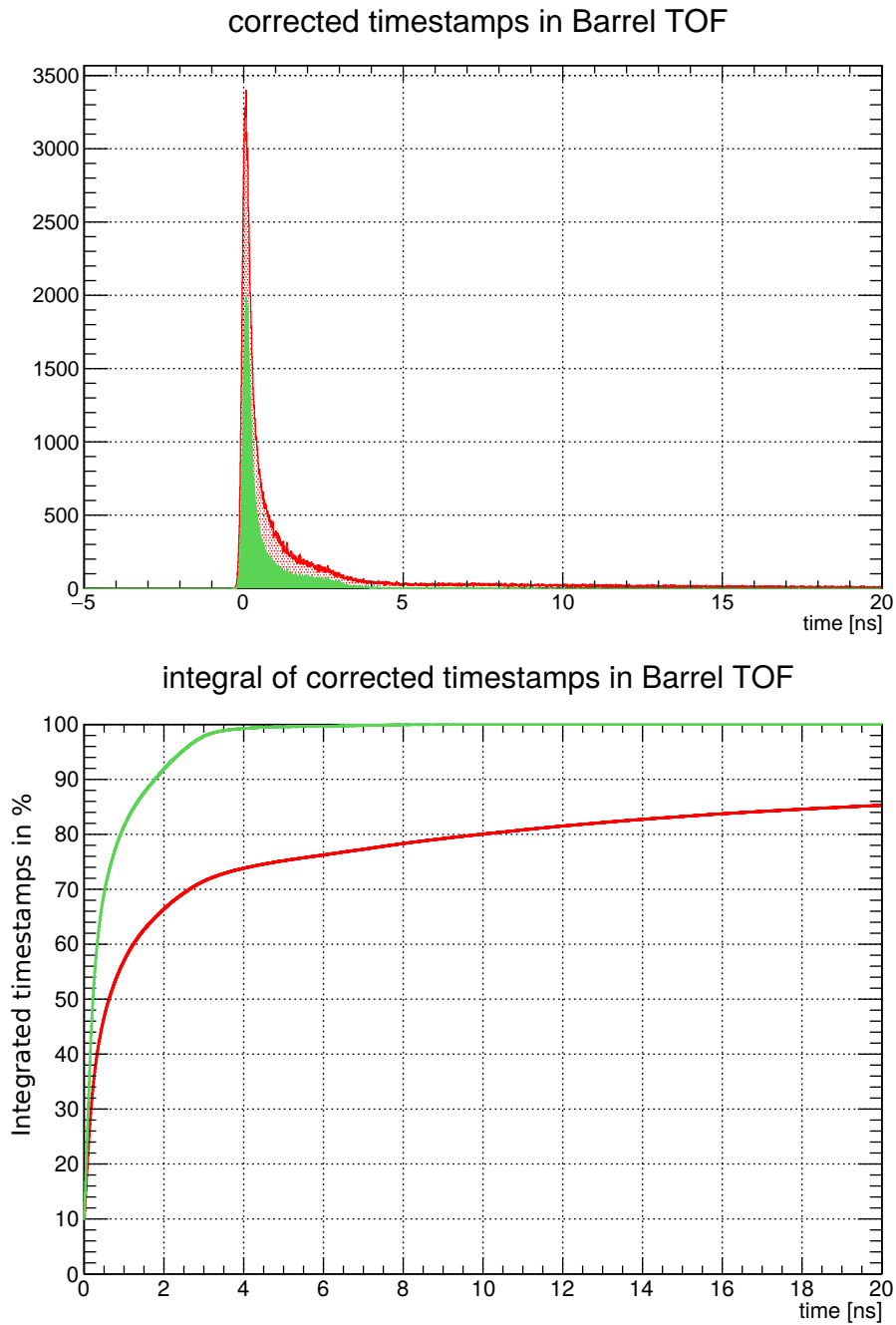


Figure 6.10: The upper plot shows the timestamp distribution in the Barrel TOF after applying the explained speed-of-light correction. The lower plot presents the corresponding integrated timestamp distribution. The fraction coming from primary particles is again colored in green, the total distribution in red

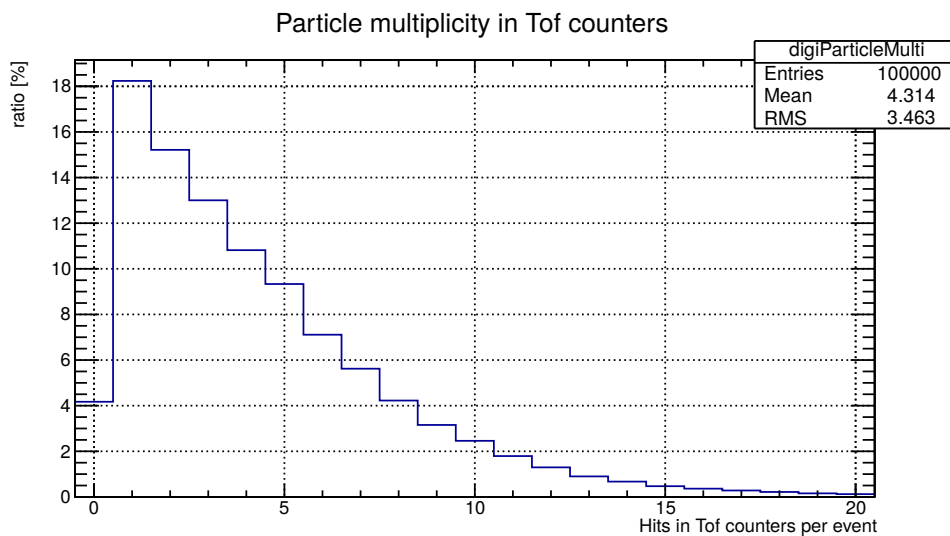


Figure 6.11: Combined particle multiplicity for the Barrel TOF and the Forward TOF detector for simulated events using the DPM generator.

further processing. As a result, a signal in the Barrel TOF can not be uniquely associated with a particular event at this level of reconstruction.

The timestamp distribution after the discussed speed-of-light correction can be exploited to optimize the number of detected events and to decrease the double association of signals to more than one event. The majority of particles arrive at the Barrel TOF well before the 15 ns, actually within the 4 ns time window. If two speed-of-light corrected timestamps are separated by more than 4 ns, this indicates two separate events.

The developed and tested algorithm in this during this thesis assumes that every delivered timestamp is a priori a potential trigger for an event candidate. All signals following within 15 ns after a triggered event may belong to the same event. Up to 4 ns after an triggered event, no new event triggers are accepted. After 4 ns signals can trigger the next event candidate. However, since every event has an acceptance window of 15 ns, the event-packages may overlap and some data will be duplicated in more than one event-package. This ensures that events close to each other are detected separately and still contain the full event information. Timestamps triggering an event serve also as an estimate for the t_0 Fig. 6.12 schematically explains this algorithm.

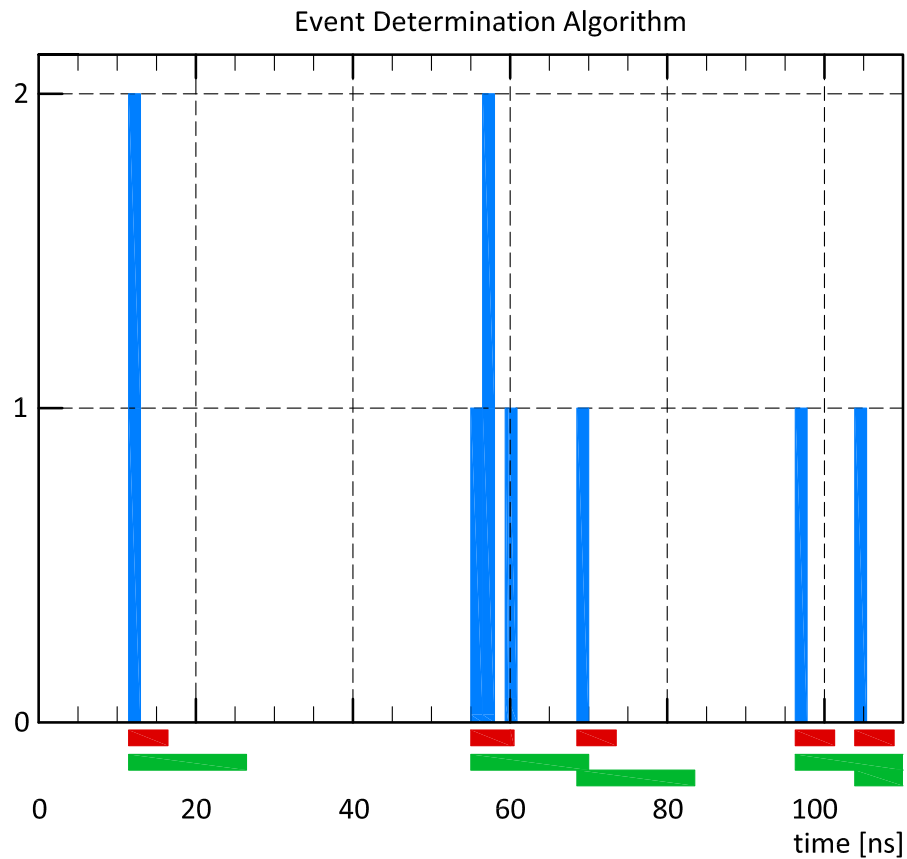


Figure 6.12: Every timestamp can potentially be the trigger for an event candidate. After a trigger has been accepted, there is a dead-time of 4 ns (red) where no other trigger is accepted. All timestamps after a trigger and within a time window of 15 ns may belong to the same event (green). These event time windows potentially overlap to ensure the completeness of the data.

6.1.3 Performance Study

To evaluate the performance of the described algorithm I analyzed 10^6 DPM events. The continuous data stream was simulated assuming 2 MHz and 20 MHz average event rate. 96% of the events produced at least one signal in either the Barrel TOF or the FTOF (cf. figure 6.11). However, for only 93% of the events a signal within 4 ns was detected, even if applying the speed-of-light correction. An event was counted as correctly identified, if it was detected within 4 ns of the $\bar{p}p$ annihilation time. This was based on the results discussed in the sections above, but may change for an upgraded algorithm taking into account also other subdetector systems. Therefore the described algorithm can maximally identify 93% of the t_0 s within a range of 4 ns.

For 2 MHz event rate about 1.73×10^6 event candidates were triggered. Analyzing the corresponding t_0 candidates revealed that about 0.93×10^6 candidates were triggered within a maximum discrepancy of 4 ns to a ideal t_0 . Hence, nearly 100% of the events with a fast TOF signal were correctly triggered as an event candidate. In addition about 0.5% of events were packed completely in the event package of the events, but didn't trigger a separate event-package. The reason for this is that the separation in time of these events was less than 4 ns. However, these events are not lost since all the data was stored. A track reconstruction algorithm of a later stage must disentangle these events from each other.

6.5% of the MC events were either missed by more than 4 ns or not found at all.

In addition to the correctly identified events about 0.8×10^6 event candidate triggers occurred, which could not be matched with an MC event within the given limits. These triggers create additional ghost event-packages, which are not present in the MC data.

The same evaluation was performed with an average event rate of 20 MHz. The fraction of correctly identified events reduced to about 89%. However, additional 4%, were packed into the event-packages of the previous events because of their small interval. Including these hidden events the fraction of found events stays at 93%. Interestingly the rate of ghost event packages reduced to about a factor of 0.66. This can be explained by the decreased average spacing of the events and therefore less options to trigger ghost events in between.

Fig. 6.13 schematically shows the results of the algorithm for a few events at an average event rate of 20 MHz. Tab. 6.1 on page 77 summarizes the results for the 2 MHz and the 20 MHz study.

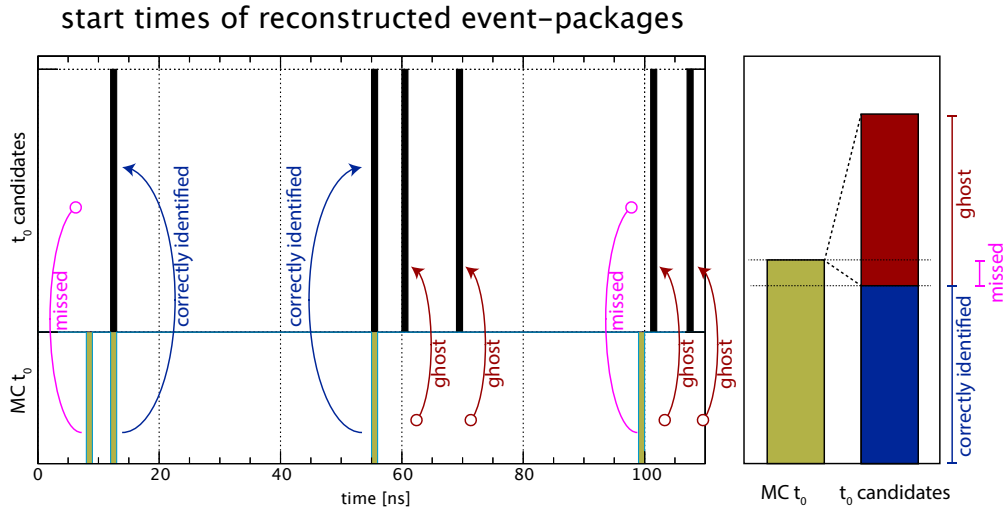


Figure 6.13: Schematic results for a 20 MHz event rate. In black the estimated t_0 for reconstructed event-packages are marked. On the negative axis in pink the MC event times are indicated. Two events are missed (pink) and 4 ghost events are triggered. The right sided diagram summarizes the fraction of MC events to correctly identified and ghost events.

As mentioned timestamps triggering an event also serves as a good estimator for t_0 . Analyzing the results of the developed algorithm showed a very good performance on the t_0 determination. Fig. 6.14 summarizes the results on the t_0 determination for 2 MHz average event rate. The t_0 can differ from the MC value up to 4 ns. A higher difference is considered as a missed event. The achieved t_0 resolution for the correctly identified events is $\sigma = 0.55$ ns. The double peak structure in this distribution is due to the slightly different timestamp distribution in the FTOF compared to the Barrel TOF. Also the used speed-of-light correction provides better results for the Barrel TOF due to the shorter track lengths compared to the FTOF detector. Therefore future improvements on the correction can even improve this algorithm.

6.1.4 Ghost Reduction

To reduce the amount of ghost events a clean up algorithm using additional sub-detector systems was studied. The basic idea is to cross check every potential trigger signal in the TOF detectors with other detector systems before accepting the trigger. Not all systems in \bar{P} ANDA are suitable for this task. The system must be placed central to ensure that nearly every event produces a signal. It must not

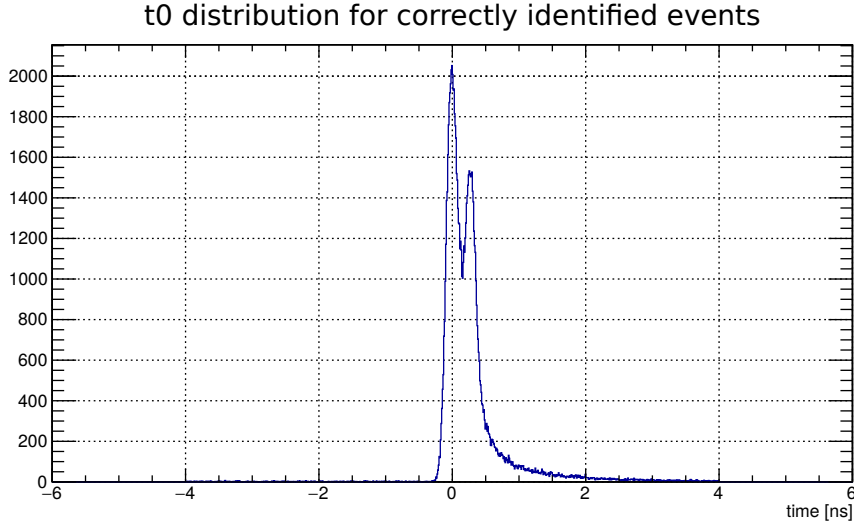


Figure 6.14: The distribution of reconstructed t_0 for all correctly identified events at 2 MHz event rate. The double peak structure is due to the slightly different timestamp distribution and speed-of-light correction performance of the Barrel TOF and the FTOF. The achieved t_0 resolution is $\sigma = 0.55$ ns

be to close to the TOF detectors to not be effected by the same backscattered or late arriving particles. Also the time resolution needs to be suitable for this task, although the requirements are low compared to the Barrel TOF time resolution. For these reasons the MVD detector was the first choice. Figure 6.15 shows the timestamp distribution MVD signals for 10^5 simulated DPM events. The standard deviation of the distribution is about 4.2 ns and the mean value is shifted by 1.9 ns as a result of the average particles flight time. Both values can be improved by applying the speed-of-light correction. However, for this first prove of principle I skipped this step because the finally t_0 is not directly influenced by the time information of the MVD. Beyond, the signal multiplicity in the MVD is in the order of 11 per event.

To decrease the ghost rate a potential trigger signal of the TOF detectors is cross-checked with the MVD signals. If a MVD signal is present in a range of ± 4 ns the trigger is confirmed. Otherwise the trigger is ignored. For an average event rate of 20 MHz this algorithm led to a reduction of triggered ghost events by more than 50 %. However, the correctly identified events were also reduced from 89 % to 83 %. Including events packed together with the previous the fraction decreases to 87 % compared to 93 %. The reason for this is that not all events produce a

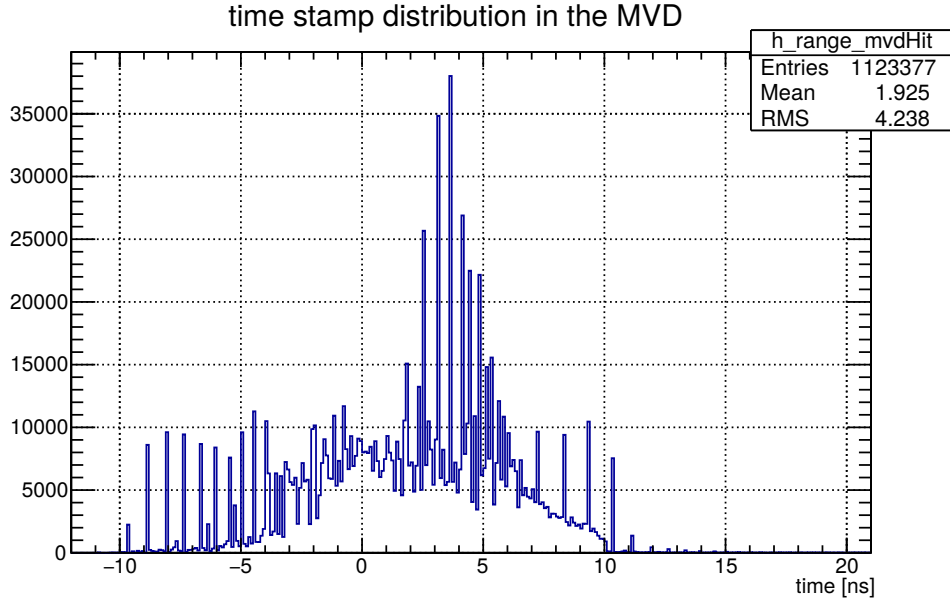


Figure 6.15: Timestamp distribution in the MVD for DPM generated events. The mean value is shifted to 1.9 ns, and the resolution in sigma is $\sigma = 4.2$ ns

signal in the MVD detector. Hence some correct triggers are discarded. This problem could be surpassed by including more detectors for the cross checking process, however, with the drawback of a reduced ghost suppression rate. The results for this simple crosschecking algorithm are also included in Tab 6.1.

6.1.5 Summary

It was shown that the late arriving particles do not prevent a sorting of the important data. The discussed algorithm is able to determine all events with at least one fast particle hitting the TOF counters. It provides a decent t_0 information without the need of any track informations. The high amount of triggered ghost event-packages can be suppressed by including other detector information. However, the fraction of correctly identified events also reduces in this case. Further studies on each sub detector system can improve the performance. However, this was out of the scope of this thesis, because the R&D of the subdetector systems is still ongoing and the start setup of \bar{P} ANDA was still in discussion. Furthermore it should be studied which type of event could not be detected with such an algorithm to ensure all events containing interesting physics are detected. A

practicable solution could be to further increase the event trigger rate if needed to include all interesting events and postpone the ghost reduction to a later stage. With additional tracking information discarding ghost packages could be done more precisely.

event rate	# t_0 candidates/ # t_0 (MC)	#identified/ # t_0 (MC)	#missed events/ # t_0 (MC)	#ghosts/ # t_0 (MC)
2 MHz	1.73	0.93 (0.935)	0.065	0.8
20 MHz	1.55	0.89 (0.93)	0.07	0.66
20 MHz with ghost reduction	1.12	0.83 (0.87)	0.12	0.29

Table 6.1: Statistical properties of the event determination algorithm. The t_0 candidates are the sum of correctly identified and ghost events. The values of correctly identified events in brackets indicate the ratio of correctly found t_0 s including also events completely packed into the previous event package. These combined with the missed events give the total number of Monte Carlo events.

6.2 T_0 Reconstruction

For a proper calculation of t_0 , tracking information as well as information on the PID is needed in addition to the timing information of the TOF counters. Accessing all this information it would be possible to calculate the position and time of creation of a particle with a very high precision. However, as discussed in section 6.1, for the online reconstruction of the events no tracking and PID information will be available in the first place. Hence, a precise calculation of t_0 is not directly possible. Nevertheless it is possible to derive a first estimation of t_0 for example in combination with the discussed event trigger and building algorithm. The final structure of the \bar{P} ANDA online reconstruction is not fixed yet, but investigated intensively at the moment. If other algorithms and detector systems can manage the event building, the TOF counters can focus on a more accurate t_0 reconstruction in this first stage. I developed and tested such an algorithm, which assumes a completed event building. It provides t_0 information for event packages which can be used afterwards for the first reconstruction iteration. The basic concept is similar to the concept used in section 6.1. Without information on track length and momentum of the particles an estimate for the flight time is used. However, I improved the accuracy of the estimation by evaluating average values for the path length and momentum instead of assuming the speed of light for the particle

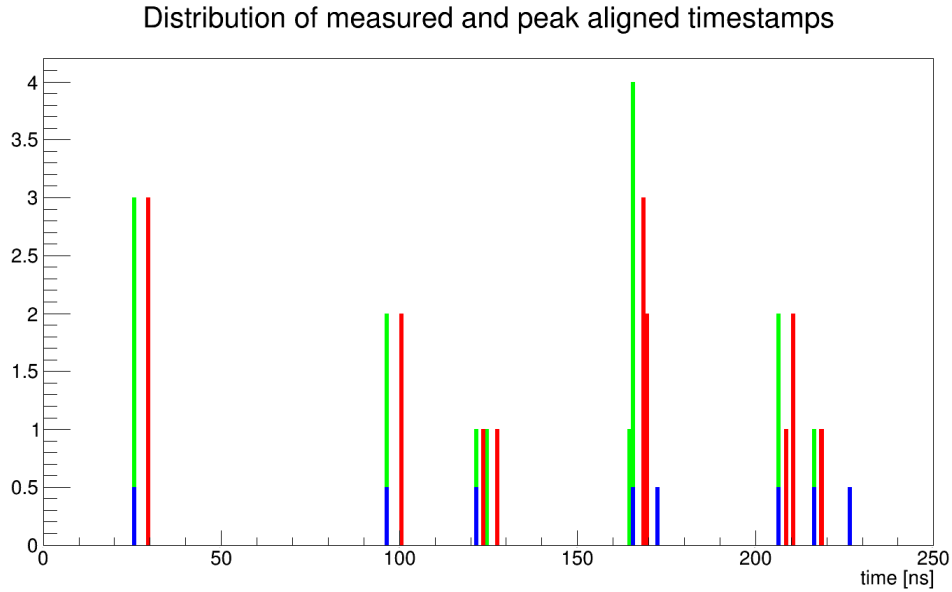


Figure 6.16: The basic principle of the timestamp correction: The measured timestamps (red) are shifted by their specific typical time-of-flight (green) and start to pile up around t_0 (blue small marks).

velocity. More precise a typical time-of-flight was evaluated, as a substitution for the average path length and momentum. In combination with the very precise time measurement and sufficient position resolution of the TOF counters the time resolution improved.

6.2.1 Typical Time-of-Flight

The measured timestamps in the TOF counters should be corrected by an typical time-of-flight. These typical flight times are correlated to the detection position in beam direction (z position) in the Barrel TOF. To estimate t_0 the measured timestamps are shifted with the corresponding typical time-of-flight (Fig 6.16). For this study Monte Carlo data was generated using the trunk version 28975 of PandaRoot. 10^6 events were simulated using the DPM generator at a beam momentum of 6.2 GeV/c.

Figure 6.17 shows the timestamp distribution of Barrel TOF signals for the event based simulation. Primary and secondary tracks and the combined distributions are indicated. In agreement with the previous discussed study, the main fraction

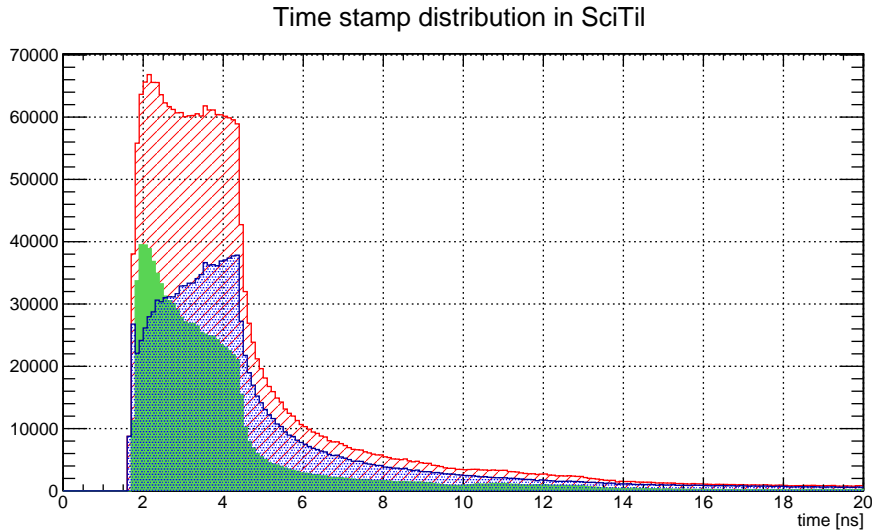


Figure 6.17: Distribution of simulated timestamps in the Barrel TOF for primary (green), secondary (blue) and combined (red) particles. The distribution of primaries is centered at 4.3 ns with a resolution of $\sigma = 3.8$ ns and FWHM of 2.6 ns. The secondaries are centered at 5.8 ns with $\sigma = 5.5$ ns and FWHM = 3.0 ns. The combined distribution centered at 5.2 ns has a resolution of $\sigma = 5.0$ ns and FWHM of 2.9 ns. Late arriving particles cause a long tail down to >20 ns, however 75% of the data points are located in the interval from 1.6 to 5.6 ns.

of the registered timestamps is located in an interval from 1.6 to 5.6 ns. Seemingly the secondary particles have an increased average time-of-flight and therefore an increased width of the distribution. However, the different structure of the dominant part of the timestamp distributions for primaries and secondaries can be explained by the distribution of the detection position of the particles as shown in Fig. 6.18. Secondary particles likely hit a Barrel TOF detector tile in more forward direction. This leads to an increased average time-of-flight. Nevertheless this effect is compensable even without knowing the particle type.

To evaluate this typical time-of-flight as a function of the detection position in beam direction the Barrel TOF has been sliced into sixty regular rings of scintillating tiles. The time stamp distributions for all rings were examined. Fig. 6.19 shows a outline of the slicing. Also the distribution for the Barrel TOF ring located 60 cm in the beam direction is shown, which is representative for all 60 slices.

Compared to the total distribution shown in 6.17 these distributions show a narrow peak for primary and secondary particles located at the same value. Hence, the

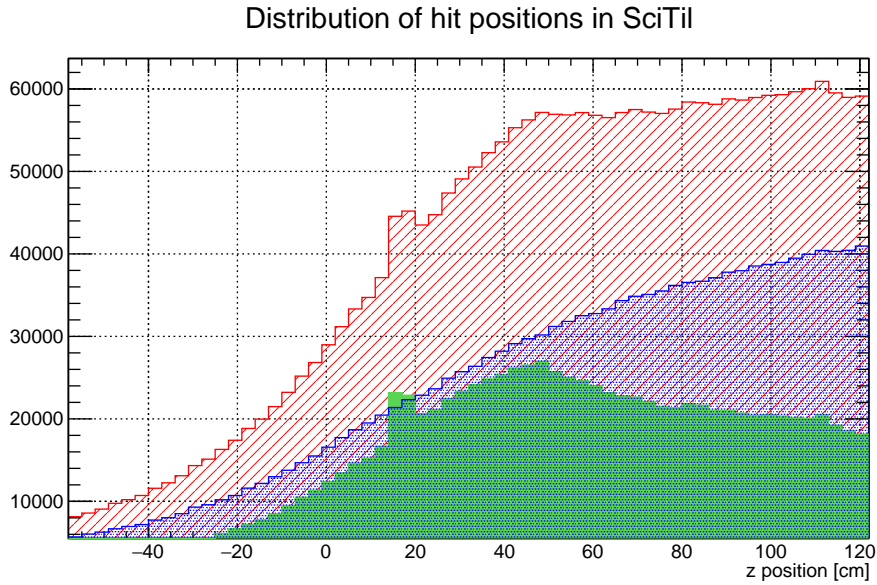
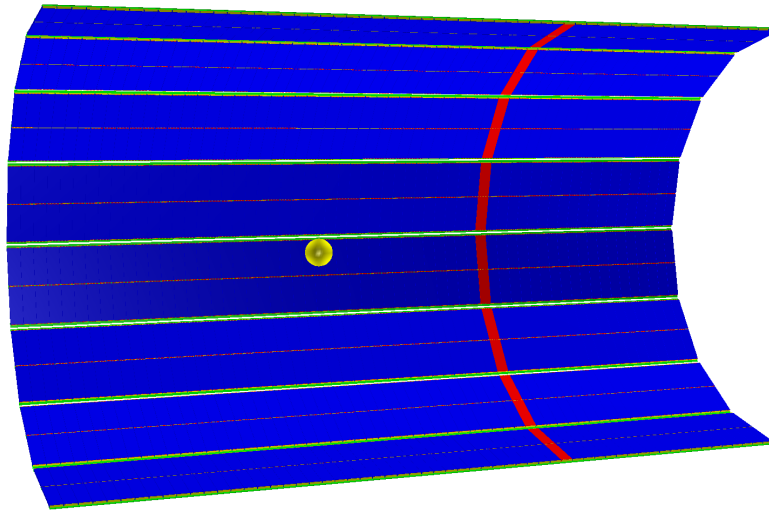


Figure 6.18: Distribution of the signals in the Barrel TOF as a function of the hit position in beam direction. Primaries (green), secondaries (blue) and combined (red) signals are indicated

primaries and the secondaries can be used for a t_0 algorithm based on the TOF counters without the need to distinguish them in advance. Figure 6.20 summarizes the mean and peak positions for all Barrel TOF rings. As expected the typical time-of-flight represented as the peak of the distributions shifts to higher values for detection ring positions further away from the $\bar{p}p$ annihilation point ($z=0$).

6.2.2 Suppressing Slow Particles

Delayed signals in the Barrel TOF, which were treated also in section 6.1.1 have a huge influence on the mean value of the timestamp distribution. Therefore one additional attempt of this study was to find and test methods to suppress very slow or late arriving particles. However, at the assumed stage of the reconstruction only very limited information will be accessible. A cross check with signals of other sub detectors may lead to a loss of useful information as shown in section 6.1.4. Additional information provided directly by the Barrel TOF would be a preferable option. Beside the timestamp and position of the detected signals the only information provided by the Barrel TOF is the energy deposit in the scintillating tile. Unfortunately I was not able to extract an exploitable correlation



Distribution of timestamps in SciTil at z position ~60 cm

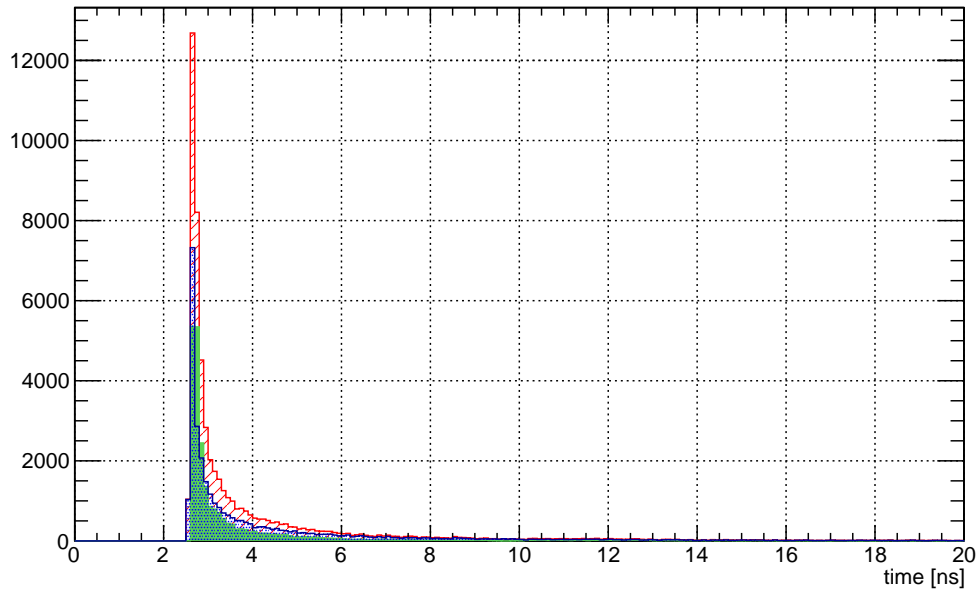


Figure 6.19: The upper plot shows one half barrel of the Barrel TOF. One equidistant ring of scintillators referred to the point of collision (marked in yellow), is highlighted in red. The lower plot summarizes the results for the detector ring, located 60 cm downstream. Primary (green), secondary (blue) and combined (red) timestamp distributions are plotted. The peak position at 2.6 ns and the FWHM of 0.2 ns are stable for all distributions. The mean values and the resolution for primaries (4.0 ns, $\sigma = 3.5$ ns), secondaries (5.2 ns, $\sigma = 5.2$ ns) and combined (4.7 ns, $\sigma = 4.6$ ns) vary due to the increased contribution of late arriving particles for secondaries.

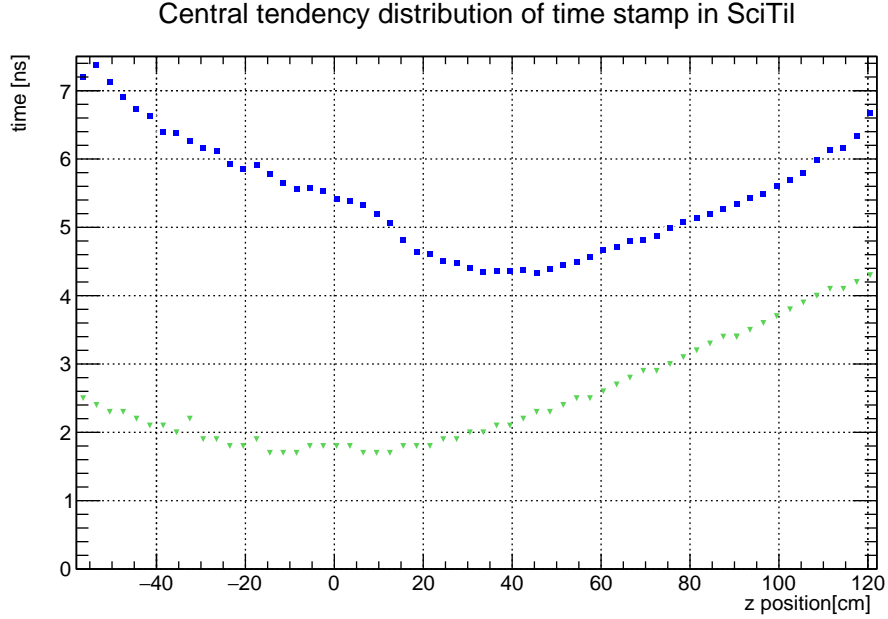


Figure 6.20: Peak (green triangles) and mean (blue squares) values of the time-stamp distributions in the Barrel TOF as a function of the detection position in beam direction.

between the energy deposit and the time-of-flight of particles. Figure 6.21 shows the energy loss of the detected particles as a function of the detection time. Although the distribution contain certain structures which can be related to lower momenta or indirect, longer flight paths, it is not possible to apply an efficient cut on the energy deposit. In any case a significant amount of fast signals would be discarded, while the suppression of late signals is at best moderate. Using more advanced preprocessing like tracking and information of other sub detectors may help to suppress the influence of slow, or backscattered particles.

6.2.3 T_0 Reconstruction Performance

As mentioned, instead of using a simple speed-of-light correction a typical time-of-flight is used to correct the timestamps. The correction values applied on the measured timestamps have a strong influence on the structure of the corrected distribution. Therefore it was a priori not obvious if the mean value of the discussed distributions or the peak position should be used to correct the timestamps. Figure 6.22 shows the corrected timestamp distributions of Barrel TOF signals af-

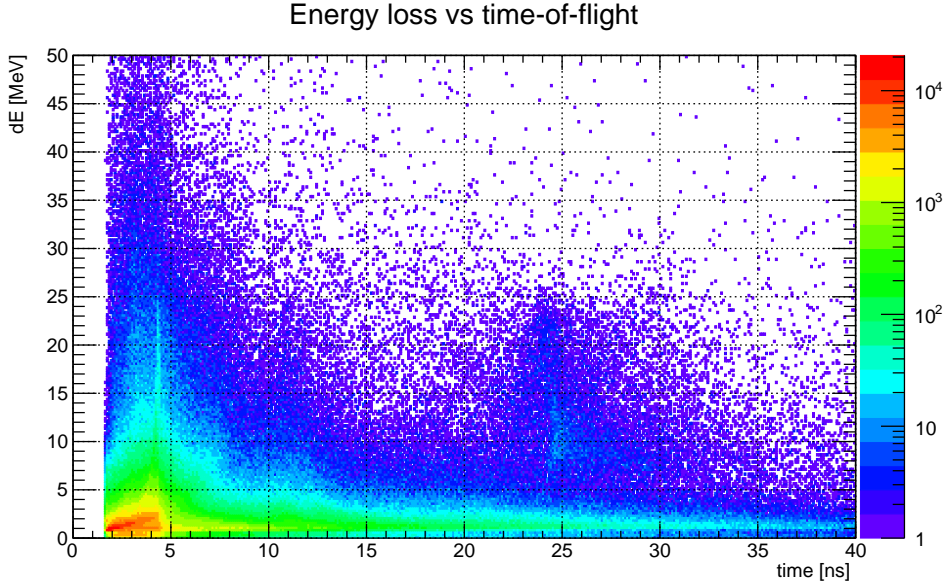


Figure 6.21: Energy loss of the particles detected in the Barrel TOF as a function of their time-of-flight. The average energy loss of slow particles does not increase. Therefore a cut on the energy loss can not suppress slow particles.

ter applying either the “peak alignment” or the “mean alignment” correction. For both distributions the FWHM decreases significantly, while the standard deviation stays nearly constant due to the long tail. For the mean aligned distribution the mean value is located at t_0 . The peak aligned distribution has a very steep rise and is peaking at the t_0 value.

The used correction must be chosen according to the further processing of the data. T_0 can be estimated by calculating the mean of the corrected time stamps per event. For this method the obvious choice is the “mean alignment“ correction. The blue graph in figure 6.23 shows the resulting t_0 distribution. It has a resolution of $\sigma = 3.9$ ns and a mean value of -0.35 ns. However it is not centered around the real t_0 . The long tail of the timestamp distributions of the Barrel TOF signals prevent this algorithm from better performances. In realistic data packages these late signals are most likely not present due to the difficulty to match them to the corresponding event. However, wrongly matched signals or noise from the electronics can influence the t_0 calculation and can not be completely avoided.

An other option is to exploit the structure of the “peak aligned” time stamp distribution. Instead of calculating the mean value of the corrected time stamps,

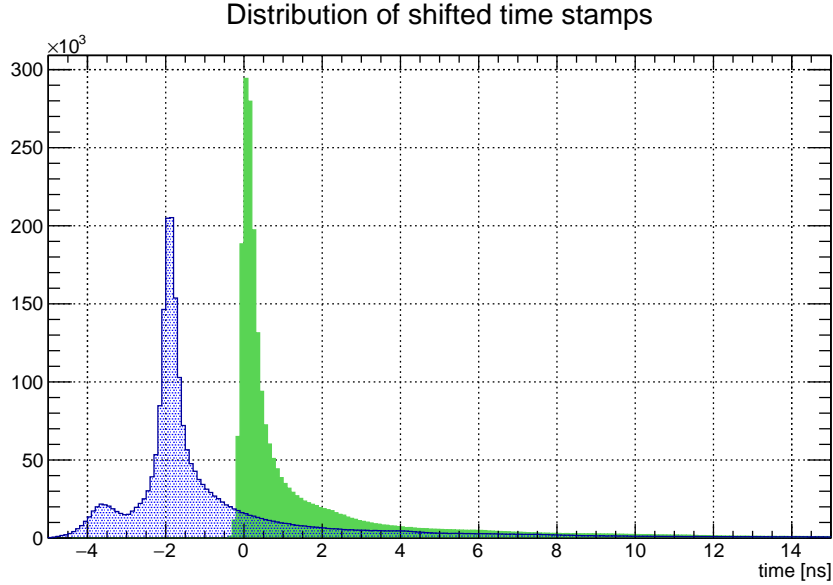


Figure 6.22: Corrected timestamp distribution of the Barrel TOF using either the mean alignment (blue) or the peak alignment (green) correction. The standard deviation remains at $\sigma = 5.1$ ns and the FWHM decreases to 0.4 ns for both distributions.

simply the first detected and corrected signal is used. Due to the steep rise of the distribution this is a good indicator for the peak position and therefore t_0 . The t_0 distribution for this “first time stamp method” is plotted in green in figure 6.23. The calculated standard deviation decreases to $\sigma = 2.3$ ns. However it is still strongly influenced by events without any fast signal in the Barrel TOF.

The accuracy of the estimated t_0 is correlated to the number of signals per event. A small number of hits in the timing counters leads to a large statistical uncertainty. Fig. 6.24 compares the t_0 distribution for events with 1 and 10 detected signals in the Barrel TOF. For the larger particle multiplicity the accuracy improves significantly, up to $\sigma = 0.4$ ns. For the results shown in this study only the time stamps from the Barrel TOF are taken into account. Including the timestamps of the FTOF will further increase the accuracy of this method. Fig. 6.11 shows the detected particle multiplicity in the TOF counters using the DPM background generator. For about 2/3 of the events 3 or more hits are registered which provide sufficient information for a good estimation of t_0 . The particle multiplicity for specific channels may differ from these background events and the t_0 resolution for this events must be studied separately.

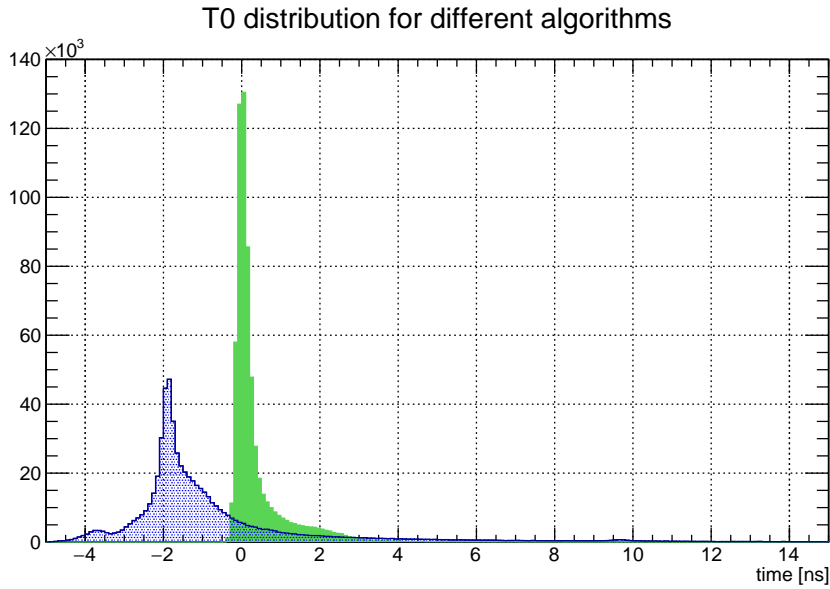


Figure 6.23: The t_0 distribution for the described algorithms. The mean-aligned method resolution is $\sigma = 3.9$ ns (blue). The first peak-aligned method results in $\sigma = 2.3$ ns and a FWHM of 0.3 ns.

6.2.4 Conclusion

It is evident that the secondary particles provide additional, useful information for the t_0 estimation. T_0 can be estimated by using the time and position information of the Barrel TOF and the corresponding typical time-of-flight. According to the calculations presented here, a resolution of 2.3 ns is achieved. As distinct from section 6.1 only the signals provided by the Barrel TOF were taken into account for this studies. Additionally also events with only very late signals were considered. A realistic event sorting algorithms probably cuts this signals away. For the remaining events with Barrel TOF signals the t_0 resolution would increase drastically (cf. 6.1). Nevertheless the results show that exploiting the peak structure of the corrected timestamp distribution of the Barrel TOF enhance the t_0 time resolution. Taking into account only events with high particle multiplicity in the Barrel TOF and therefore a most likely with at least one fast signal the t_0 time resolution already improves to $\sigma < 0.5$ ns. Including the FTOF would further improve the resolution.

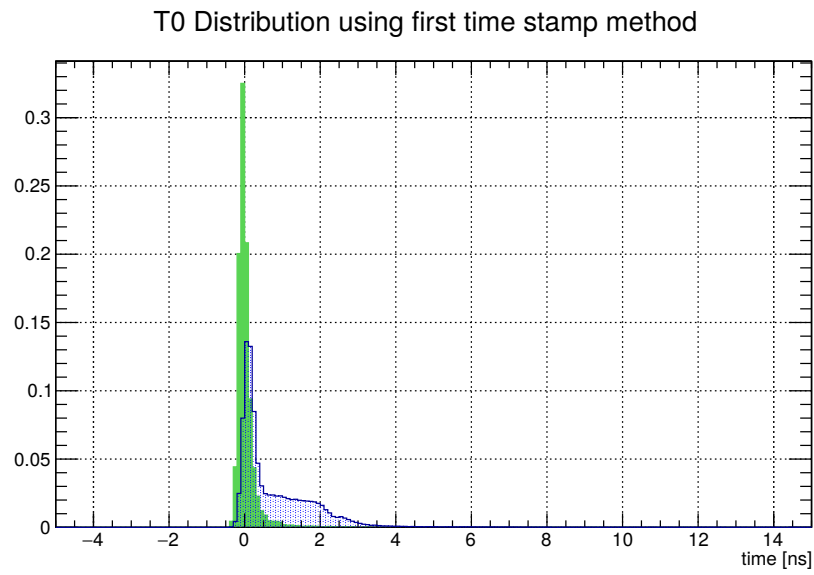


Figure 6.24: The t_0 distribution obtained using the “first time stamp” method for events with a particle multiplicity in the Barrel TOF of 1 (blue) and 10 (green). For events with only one detected particle in the Barrel TOF a $\sigma = 3.7$ ns was achieved. For a particle multiplicity of 10 the resolution improved to $\sigma = 0.4$ ns.

6.3 Relative Time-of-Flight

As described in section 6.1 and 6.2 the determination of t_0 is required during online and offline processing of the data. One application, which demands a t_0 is the time-of-flight based particle identification. Such PID algorithms are based on a measurement of the time difference between the creation time and the detection time of the corresponding tracks in the TOF detectors. Hence, an accurate t_0 has a strong influence on the performance of this TOF based PID systems. Due to technical reasons the installation of a start time detector with a precise time measurement close to the interaction point is not possible in \bar{P} ANDA. Therefore a conventional TOF based PID for single tracks as described in section 6.4 may not be possible in the first reconstruction stage. However, after the event sorting and first track reconstruction, methods based on relative time-of-flight can provide t_0 and PID information without the need for a dedicated t_0 detector. The studies in this section describe the first attempt to apply this methods in the PID stage of \bar{P} ANDA. As mentioned the software framework PandaRoot is still evolving and not all sub detectors are included in a realistic manner. For this reason only the performance of the Barrel TOF was investigated as a prove of principle. For a final implementation other detectors, with the FTOF leading the way should be included, however this was out of the scope of this study.

6.3.1 Relative Time-of-Flight Algorithm

The algorithm, described in the following lines, to overcome the t_0 problem is based on an method described 1981 in [39]. In comparison to the algorithms discussed in sections 6.1 and 6.2, finished event sorting and track reconstruction are needed for this relative time-of-flight algorithm.

The basic principle of the relative time-of-flight algorithm is to iterate through all possible mass configurations for an event. The considered particle species are p, K, π , μ and e. Hence, for an event with N tracks hitting the Barrel TOF, a priori 5^N possible mass configurations exists. For every mass configuration the expected time of creation for every track is calculated using the measured momentum and track length provided by the tracking system. T_0 is calculated as the average of the track creation times. Subsequently, the conformities of the calculated track creation times are rated for every mass configuration. The mass configuration with the most conform track creation times is the most probable one. Fig. 6.25 summarizes this basic principle.

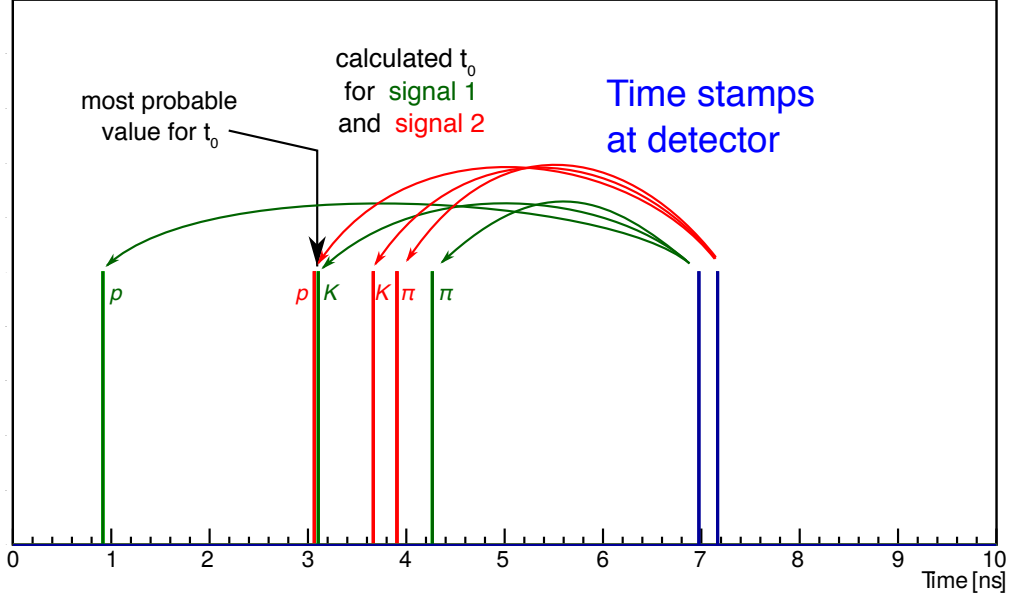


Figure 6.25: For the detected signals in the Barrel TOF (blue) possible track creation times according to a certain mass assumption are calculated (green and red). The combination providing the best conformity is equivalent to the most probable mass configuration.

I adapted this basic principle to the tracking and time-of-flight system of $\bar{\text{P}}\text{ANDA}$ and implemented an algorithm based on this basic principle in the PID stage of PandaRoot. The statistical evaluation is done by a combinatorial algorithm. It assumes a common event time t_0 for every mass configuration. A χ^2 probability weight $W_{(m_1, \dots, m_N)}$ is provided based on the comparison of the measured time-of-flight and the expected time-of-flight of the tracks. The expected time-of-flight is calculated using the reconstructed track parameters. For a given event this task can be reduced to the minimization of the term,

$$\Psi_{W_{(m_1, \dots, m_N)}} = \sum_{i=1}^N \frac{(t_{i,0} - t_0)^2}{\sigma_{i,TOF}^2} \quad (6.2)$$

iterative for all possible mass configurations. The sum is over all tracks hitting the Barrel TOF. The $t_{i,0}$ is the expected track creation time for the mass hypothesis of $track_i$. The event start time t_0 is the free parameter to minimize the term. $\sigma_{i,TOF}$ is the resolution of the time-of-flight system, taking into account the intrinsic time resolution of the Barrel TOF and the momentum and track length resolution of the tracking system. The TOF system resolution is discussed in section 6.4.2. The

expected track creation time $t_{i,0}$ is calculated using formula

$$t_{i,0} = t_i - \frac{L_i \sqrt{p_i^2 + m_i^2}}{p_i c}. \quad (6.3)$$

L_i and p_i are the measured track length and momentum, m_i is mass hypothesis for $track_i$. The minimization of formula 6.2 as a function of t_0 can be simplified to calculating the weighted mean value $\langle t_0 \rangle$ of the $t_{i,0}$. This is done by calculating

$$\langle t_{0,W(m_1,\dots,m_N)} \rangle = \frac{\sum_{i=1}^N \frac{t_{i,0}}{\sigma_{i,TOF}^2}}{\sum_{i=1}^N \frac{1}{\sigma_{i,TOF}^2}}. \quad (6.4)$$

By applying the found t_0 s on equation 6.2, the $\Psi_{W(m_1,\dots,m_N)}$ are evaluated for the tested mass configuration. For the correct mass configuration the $\Psi_{W(m_1,\dots,m_N)}$ are distributed as a χ^2 with $N - 1$ degrees of freedom. The incorrect mass hypotheses will have higher χ^2 values. The observation probability of a χ^2 can be interpreted as a weight $W_{(m_1,\dots,m_N)}$ for the tested mass configuration.

The basic version tested in this study used the mass configuration giving the smallest χ^2 to determine t_0 .

6.3.2 Relative Time-of-Flight Performance

To test the implemented relative time-of-flight algorithm described in this section, simulation studies were performed using PandaRoot trunk version 29448. The simulation setup included the full available \bar{P} ANDA geometry. The events were generated using the DPM generator with a primary beam momentum of 6.2 GeV/c. The discussed relative time-of-flight algorithm was implemented locally on my personal computer in the PID stage of PandaRoot. Therefore the data of the track reconstruction are accessible.

The relative time-of-flight algorithms has increased requirements compared to the previous discussed event sorting and t_0 algorithms. It needs at least two fully reconstructed tracks with a matched Barrel TOF or FTOF signal. Due to the status of the forward tracking implementation and the FTOF in PandaRoot at the time of this study, the FTOF could not be used for this performance study. For that reason the results shown in this section only refer to events with the respective amounts of suitable tracks in the target spectrometer.

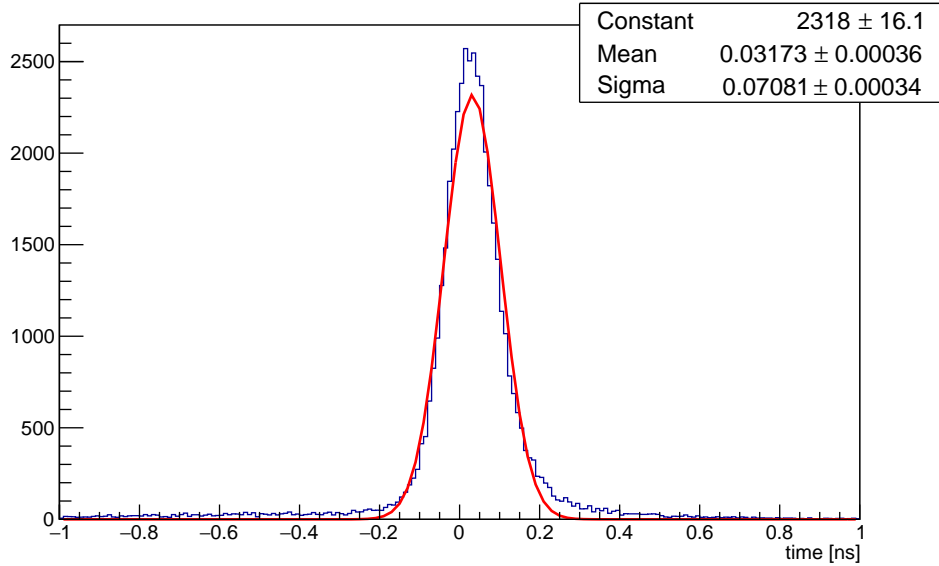


Figure 6.26: Distribution of determined t_0 for events with three or more reconstructed tracks hitting the Barrel TOF. The mean value of 32 ps is slightly shifted. The t_0 resolution is $\sigma = 71$ ps

Fig. 6.26 shows the distribution of the determined t_0 for events with at least 3 reconstructed tracks matched with a Barrel TOF signal. Apparent from the plot the accuracy of the t_0 increases about one order of magnitude compared to the t_0 estimation suggested in section 6.1 and 6.2. The mean of the distribution is slightly shifted to 31 ps instead of the MC value of 0 ps. The reason for this is a systematic underestimation of the track length by the track reconstruction algorithms. With a final, improved tracking this error will decrease.

The achieved resolution of $\sigma = 71$ ps can be improved further. Applying the analysis only on events with 3 or more primary tracks matched with the Barrel TOF and ignoring tracks of secondary particles shows a significant enhancement. This also reflects the status of the track reconstruction algorithms, which are still under development. Especially the reconstruction of displaced, secondary tracks is not finished yet. The observed t_0 resolution for this events is shown in Fig. 6.27. The parameters enhance to a t_0 resolution of 57 ps centered at 25 ps.

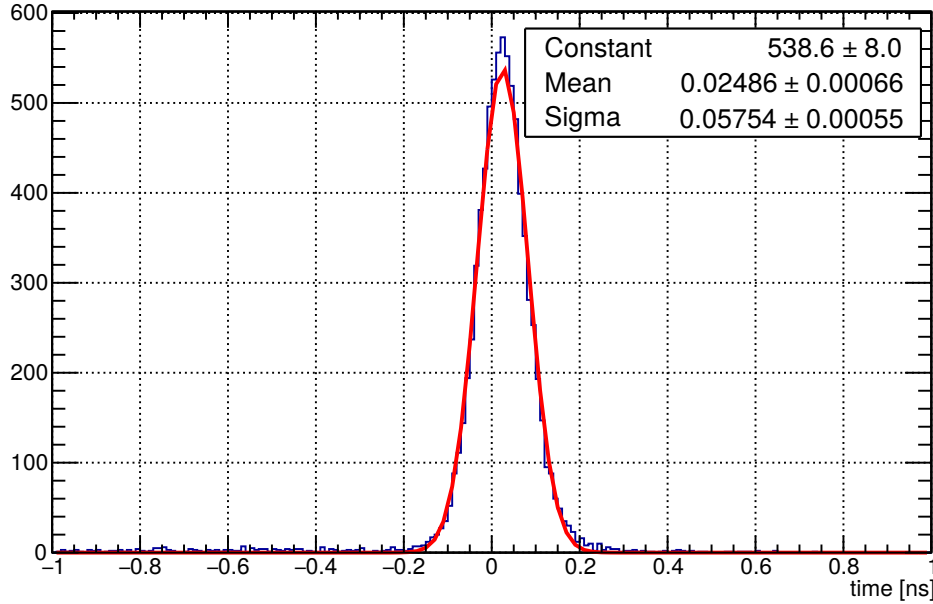


Figure 6.27: Distribution of determined t_0 for events with three or more reconstructed primary tracks matched with the Barrel TOF. The mean is located at 25 ps and the resolution is enhanced to $\sigma = 57$ ps.

6.3.3 Algorithm Enhancements

In the described study only the target spectrometer was included. It can reasonably be expected that this algorithm delivers improved results when the information provided by the forward tracker and the FTOF is included. The reason therefore is not only the increased number of tracks per event to improve the statistics. In addition the different expected momenta of forward emitted particles and the relative long flight path to the FTOF result in a different pattern of the calculated start times for the tested mass configurations. Therefore the pile up probability of the track creation times from target and forward spectrometer tracks would be reduced significantly for a wrong mass configuration. Also ongoing improvements of the tracking algorithms will enhance the performance. The track length of particles starting from the interaction point is reconstructed well. For displaced vertices a significant offset may occur. Also the momentum of the particles is considered as a fixed value although the energy loss of particles can have a significant influence especially for low momentum particles. Both effects can explain the observed offset in the reconstructed t_0 and can be minimized in future version of the algorithm.

In addition it is possible to implement a pre-selection on a specific time window

for the t_0 . The time-window can be chosen based on earlier t_0 estimation or informations of other detectors. In this way some wrong mass configurations can be ignored to save computing resources. Also mismatched or wrong reconstructed tracks can be excluded. A similar approach is used successfully by the ALICE collaboration [40]. The calculated start time of a single track is compared with the reconstructed t_0 using this relative time-of-flight method applied on all other tracks of an event. The influence of such single tracks on the over all χ^2 is checked. If the accordance is poor the tracks are rejected because of a probably poor reconstruction.

Apart from this methods which are based solely on the TOF counter information, it is possible to use the PID information of other detectors to improve the estimation of t_0 . In a simple version a very well tracked and identified particle is used to determine a very accurate t_0 window and afterwards the relative time of flight algorithm search for the mass configuration which fits best the previous conditions. The more particles are identified and tracked precisely as an input to the algorithm the more accurate the final result will be.

6.3.4 Relative Time-of-Flight Based PID

As described in section 6.3.1 the relative time-of-flight algorithm provides χ^2 values for each possible mass configuration. These can be used to derive a weight $W_{(m_1, \dots, m_N)}$ for the configurations. This set of 5^N weights contains all information provided by the tracking and time-of-flight subsystem and therefore can be used directly for a PID decision. It provides a kind probability density function for the corresponding mass combination and the estimated t_0 . However, it is also possible to deliver a PID for single particles to be conform with other ID algorithms. Therefore the probability for a detected particle to be of a specific particle species is calculated using [36]

$$P_{i,j} = \frac{\sum_j W_{(m_1, \dots, m_N)}}{\sum_{i=1} W_{(m_1, \dots, m_N)}}. \quad (6.5)$$

The sum in the numerator is taken over all particle mass configurations, where the i -th track is assumed to be from particle species j . The sum in the denominator is over all weights of the 5^N possible configurations. This calculations provide a probability density function for all tracks and mass hypotheses.

An alternative is the use of the determined t_0 to perform a PID based on a standard

time-of-flight method which is described in section 6.4.

6.4 TOF based particle identification (PID)

Time-of-flight based particle identification determine the mass of particles by measuring the momentum, the path length and required, eponymous time-of-flight between a starting and a stopping position. Due to the uncertainty in the measurement of the track length, momentum, and time-of-flight the mass can not be derived with infinite precision. As a result the particle species can not be determined precisely, instead a probability density function (p.d.f) for every mass hypotheses can be provided.

6.4.1 Basic concept

To derive the p.d.f for a reconstructed track the expected time-of-flight of the particle to the Barrel TOF is calculated. For this the reconstructed track length and momentum provided by the tracking system and a mass hypothesis is used. The time-of-flight based PID algorithm I implemented in PandaRoot covers the mass hypothesis of e^- , μ^- , π^+ , K^+ , p^+ and respective antiparticles. The following equation is used to calculate the expected time-of-flight

$$t_i = l \times \sqrt{\left(\frac{m_i}{p}\right)^2 + 1}. \quad (6.6)$$

t_i is the calculated time-of-flight, l the reconstructed track length, p the reconstructed momentum and m_i the mass hypothesis. As the next step normalized Gaussian are created, located at the calculated time-of-flights. The parameters of these Gaussian, in a narrow sense the standard deviation, must be adapted to the resolution of the whole TOF system. The resolution of the time-of-flight system is affected not only by the intrinsic time resolution of the Barrel TOF, but also by the track length and momentum resolution of the tracking system. The probability density function is derived from the Gaussian evaluated at the measured time-of-flight of the particles (cf. figure 6.28). Finally the identification probability is derived by normalizing the derived probability density functions in a way that the combined p.d.fs sum up to a value of 1.0.

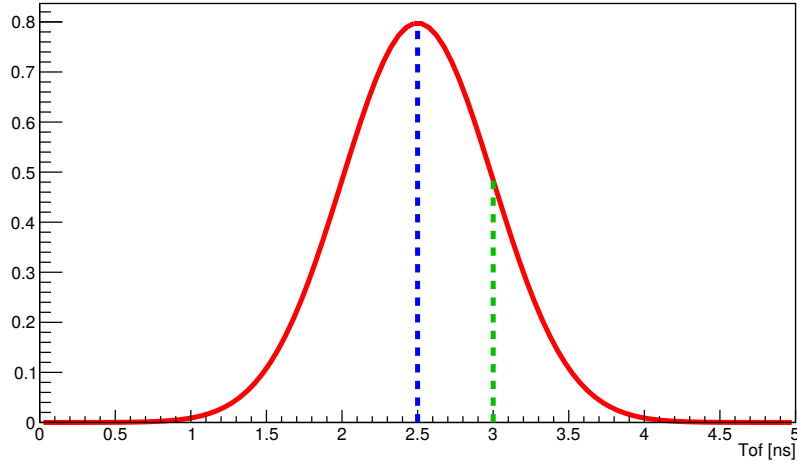


Figure 6.28: The basic concept of evaluating the probability density function for a mass hypothesis. A normalized Gaussian is created at the expected time-of-flight for the mass hypothesis of a proton (blue). The width of the Gaussian is determined by the resolution of the time-of-flight and tracking system. The probability density is evaluated at the measured time-of-flight in the Barrel TOF (green).

6.4.2 Time-of-Flight Resolution

The resolution of the tracking and the time-of-flight system was evaluated using MC simulations in PandaRoot. For this study the trunk version 28975 was used. The Box generator was used instead of the DPM generator to create a well defined particle distribution. 10^6 particles per species with a momentum between of 0.05 - 3 GeV/c were simulated. The emission angle covered the full detection area of the Barrel TOF. At the time when this study was performed, the method for t_0 determination in $\bar{\text{PANDA}}$ was still under discussion. The t_0 resolution was unknown even with limited precision. For that reason a perfectly reconstructed t_0 was assumed in this study. A cut on the reduced χ^2 parameter of the reconstructed and fitted tracks was applied to suppress all tracks with a reduced $\chi^2 > 5$. This mainly effected tracks with a transverse momentum < 0.3 GeV/c which could not be handled properly by the current implementation of the tracking system and ensured that the study is not biased by miss reconstructed outliers (cf. figure 6.29).

The time-of-flight resolution was expected to be neither the same for all particle species nor a fixed value for a specific particle type. In fact it should depend on

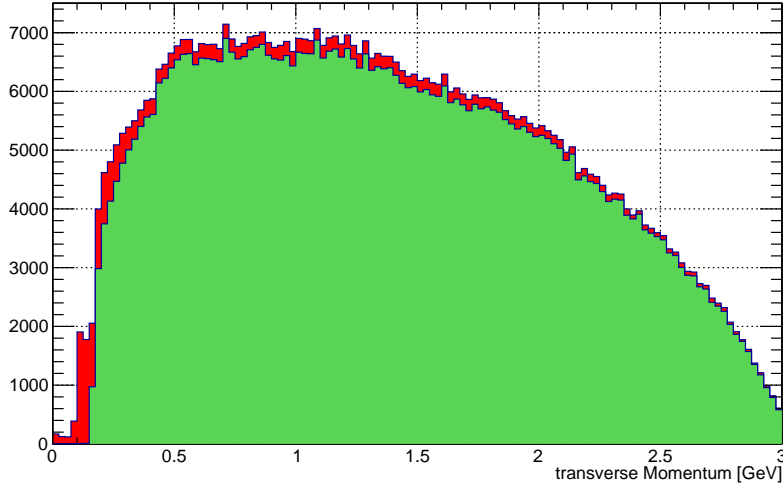


Figure 6.29: The detected timestamps of protons for the TOF resolution evaluation as a function of p_t is plotted (red). A cut on the reduced $\chi^2 < 5$ of the track reconstruction is applied to be less affected by falsely reconstructed tracks (green). This affects particularly tracks with a $p_t < 0.3 \text{ GeV}/c$ and reduces the data by 4.58 %

various track parameters due to different reconstruction efficiencies and resolutions of the tracking system. Therefore the time-of-flight resolution was evaluated independently for the 5 particle species $e^-, \mu^-, \pi^+, K^+, p^+$ as a function of track parameters like momentum, transverse momentum, track length and hit position in the Barrel TOF. To reduce a binning effect of the track parameters in the evaluation a residual time resolution

$$t_{res} = t_{measured} - t_{expected} \quad (6.7)$$

was studied. The expected time-of-flight was calculated using

$$t_{expected} = \frac{l\sqrt{p^2 + m^2}}{pc}, \quad (6.8)$$

with l and p as the measured length and momentum of the track. m is the mass of the particle species, known in this MC studies. To further suppress outliers a maximum difference between $t_{measured}$ and $t_{expected}$ of 50% was allowed. Tracks not fulfilling this requirement were excluded from the study. This reduced the data sample by additional 0.3%. Figure 6.30 shows a typical residual time-of-flight distribution for π^- for a transverse momentum range from 1.5 to 1.51 GeV/c and hit positions of 40 to 46 cm in beam direction in the Barrel TOF.

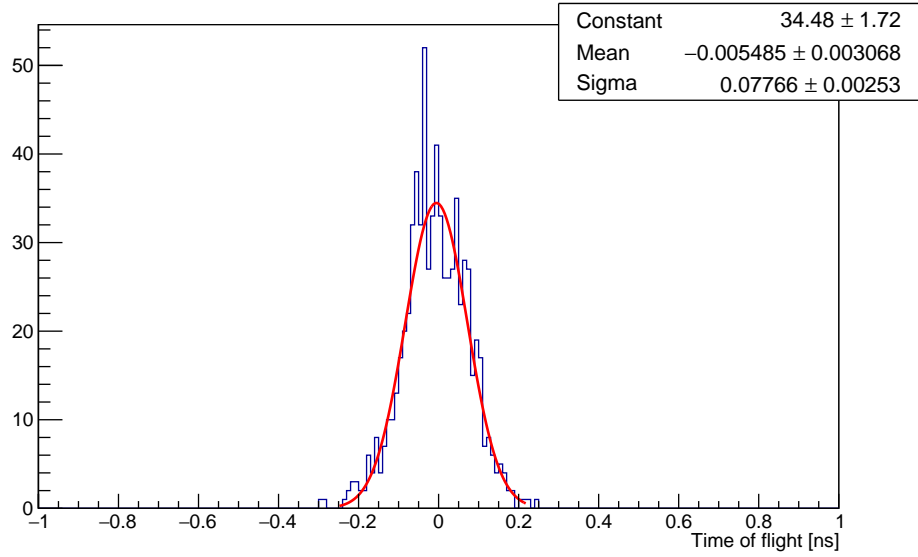


Figure 6.30: The time-of-flight distribution for π^- with a transverse momentum of 1.5 to 1.51 GeV/c detected in the Barrel TOF at 40 – 46 cm in beam direction. The time-of-flight resolution for these track parameters is $\sigma = 0.78$ ns

The evaluated time-of-flight resolutions were summarized in two dimensional profile plots, combining the discussed parameters to study the influence of the track parameters. In this way it was possible to evaluate also a cross influence. Figure 6.31 shows some summary plots for the pion. The studies showed that all investigated parameters influence the TOF resolution of the system. However, the influence can always be retraced to the transverse momenta of the particles. Hence, parameterizing the time-of-flight resolution as a function of the transverse momentum allows a steady description of the respective sigma value.

To parameterize the time-of-flight resolution as a function of the transverse momentum the measured data were fitted using equation 6.9

$$\sigma = \frac{a}{p_t^4} + b \quad (6.9)$$

Among others, this function showed the best χ^2 values for the fits. Figure 6.32 and 6.33 and Tab. 6.2 summarize the results for the different particle species.

The time-of-flight resolution stays stable for high transverse momenta at a value around 78 ps. Below 0.5 GeV/c the time-of-flight resolution worsen due to the

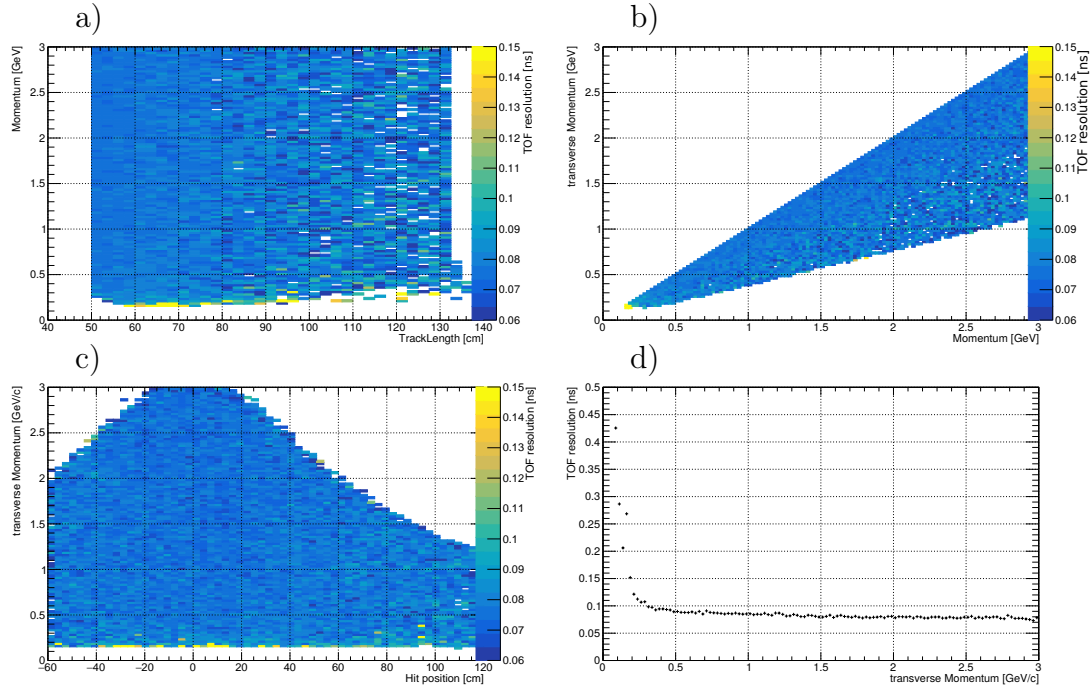


Figure 6.31: The time-of-flight resolution for pions as a function of two track parameters is shown. a) Track length and momentum. b) Momentum and transverse momentum. c) Hit position in the Barrel TOF and transverse momentum. d) The final plot describes the TOF resolution solely as a function of the transverse momentum

particle species	a	b
proton	1.24×10^{-3}	0.0787
kaon	3.00×10^{-4}	0.0767
pion	2.25×10^{-5}	0.0764
muon	2.22×10^{-5}	0.0768
electron	1.53×10^{-5}	0.0765

Table 6.2: The obtained fit parameters for the time-of-flight resolution as a function of the transverse momentum for the different particle species. The fit was performed using equation 6.9.

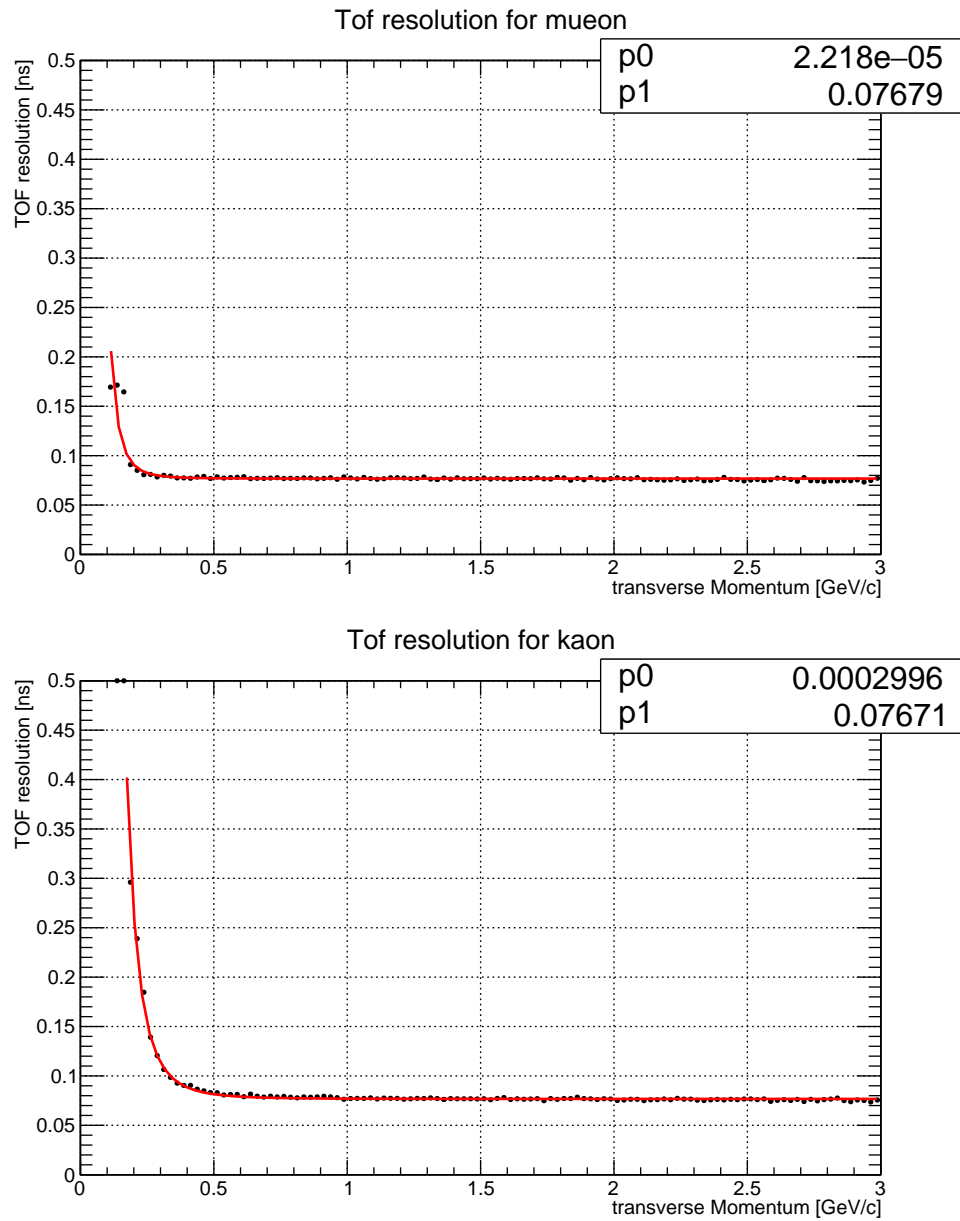


Figure 6.32: The time-of-flight resolution as a function of the transverse momentum for μ and K . The results are representative for all tested particle hypotheses. The red line indicates the fit according to equation 6.9

time of flight resolution

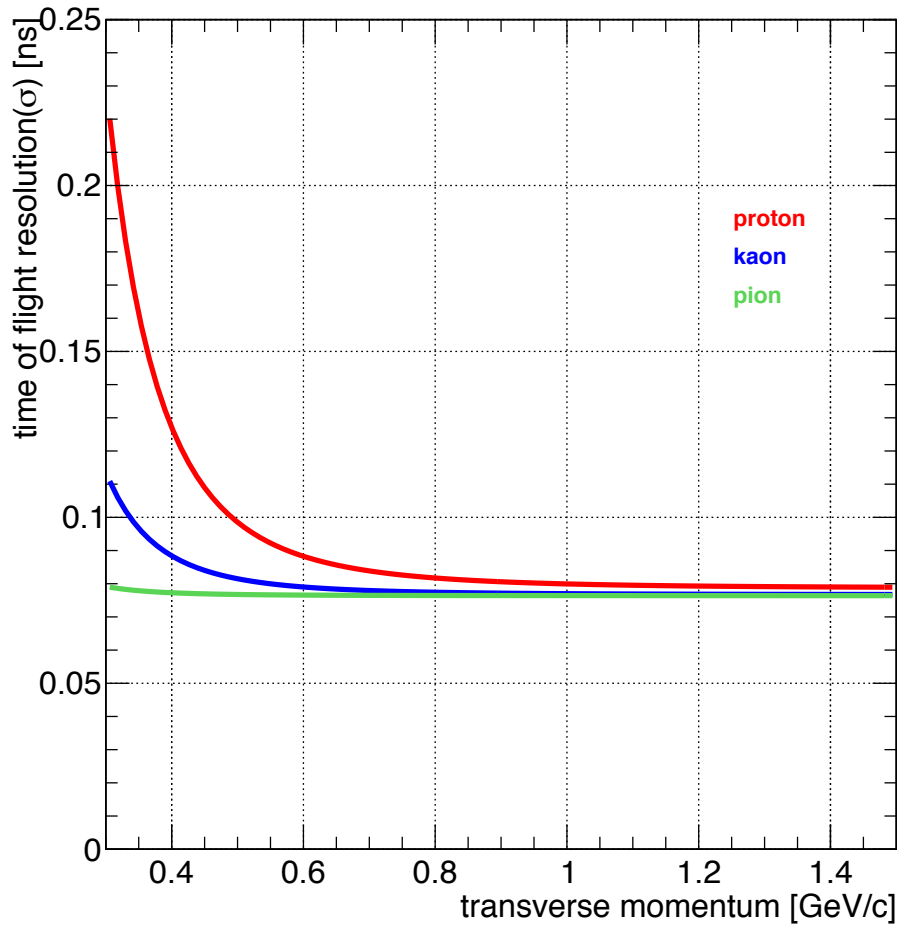


Figure 6.33: Combined fit results of the time-of-flight resolution for p, K, π as a function of the transverse momentum.

worsen momentum and track length resolution. The time-of-flight resolution is more affected for heavier particles than for lighter particles.

6.4.3 TOF Separation Power

The PID separation power for the Barrel TOF using the described time-of-flight method is derived using equation 6.10

$$n_\sigma = \frac{|tof_p - tof_K|}{\frac{\sigma_p}{2} + \frac{\sigma_K}{2}}. \quad (6.10)$$

The time-of-flight resolution σ_i is determined by the derived equation 6.9. The time-of-flight tof_i was calculated using equation 6.6. However, the transverse momentum and a projected track length in the xy plane were used, because only the transverse parts effect the time-of-flight resolution. The projected track length was calculated using 6.11 and 6.12

$$l = r_{bend} * \arccos\left(1 - \frac{r_{BTOF}^2}{2 * r_{bend}^2}\right) \quad (6.11)$$

$$r_{bend} = \frac{p}{qB} \quad (6.12)$$

r_{bend} is the bending radius of a charged particle and r_{BTOF} is the radius of the Barrel TOF, i.e. 0.5055 m. 2 T is assumed for the magnetic field B. The resulting PID separation power of the Barrel TOF for protons, kaons and pions is summarized in figure 6.34.

The separation power stays above 2σ for π/K and above 5σ for K/p separation up to 1 GeV/c transverse momentum. With decreased transverse momentum, especially below the Cherenkov threshold, the separation power increases strongly up to 15σ and 25σ , respectively. The decreased accuracy of the tracking system at very low p_t is partially balanced by the increased time-of-flight difference for these tracks. Hence, a powerful separation of the particles is ensured for the full range of reconstructable tracks.

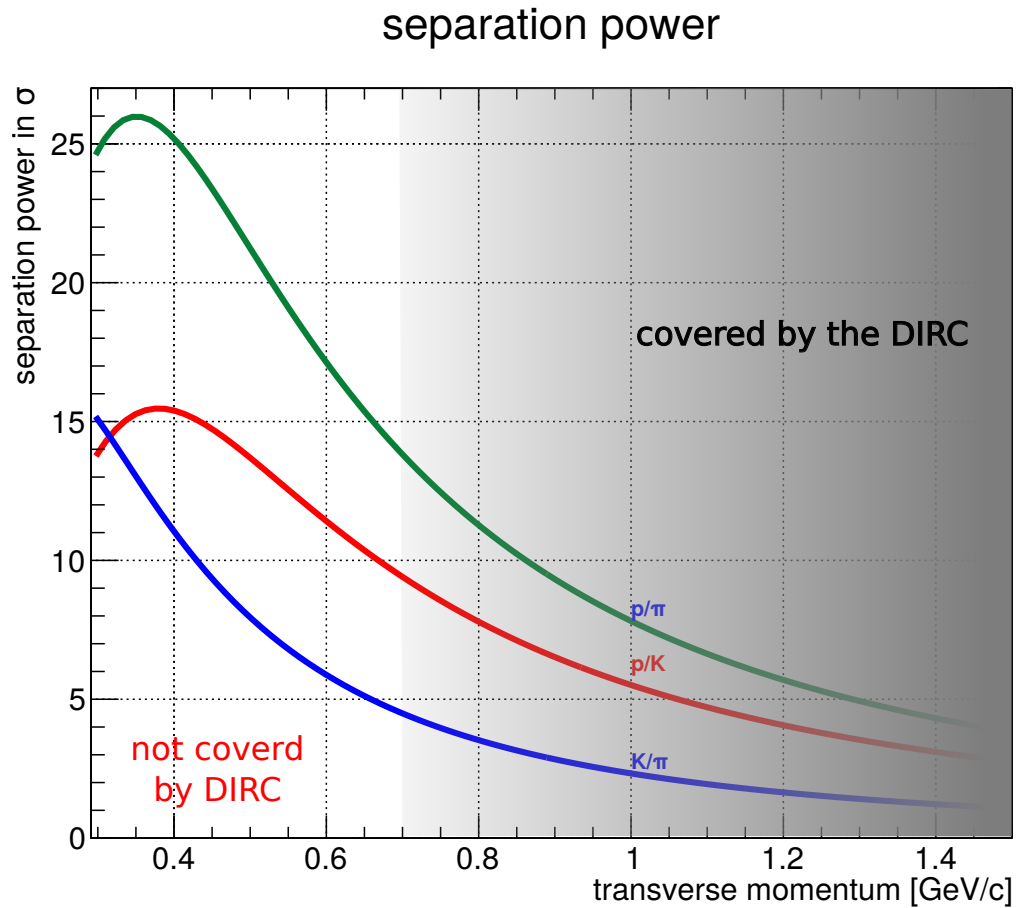


Figure 6.34: Separation power in terms of σ for combinations of p , K and π . Due to the increased time-of-flight resolution for $p_t < 0.4$ GeV/c the separation power decreases for slow particles, although the time-of-flight difference increases. The black shadow indicates the operation region of the DIRC detector.

7 Time Based Event Reconstruction

The importance and the difficulty for the $\bar{\text{PANDA}}$ event reconstruction arising from the technical setup have been discussed already in section 2.3.8 and 3.3.4. Finding a universal technique to identify and reconstruct all relevant events while operating the experiment in the high luminosity mode is a challenging task. Especially since one has to take care of very different event topologies. Section 2.3.8 and figure 2.12 already introduced a basic concept which is currently discussed in the collaboration. During a 6 month internship in Uppsala I worked on this important task and was able to perform the first track reconstruction, using data simulating the continuous read out.

7.1 Preparation

The reconstruction algorithms implemented in PandaRoot at this time were not able to deal with a continuous data stream directly. Such an operation mode would require a advanced memory management to buffer the incoming data stream and provide read and write access for multiple processing nodes at once. This also require flexibility of the involved reconstruction algorithms and probably increases the processing time. One solution is to split the input data stream into event packages of processable size and distribute them to many computing nodes. These packages then can be processed individually in parallel. I implemented such event packing algorithms in PandaRoot and updated an already implemented track reconstruction algorithm for handling these packages, i.e the STTCellTrackFinder. Finally the performance on these event packages, including many, potentially mixed events, was evaluated.

7.1.1 PndBranchBurstBuilder

In a first step a base class called PndBranchBurstBuilder was implemented. This class offers the necessary functionalities to easily derive specialized algorithms for the packaging of the initial data. The provided base functionalities are the handling of the input detectors data streams, the output data stream including a name prefix management, and memory management for the internal sorting and packaging. A missing, but mandatory, function for the finally derived classes is the “cutting function”. It has to decide where to cut the incoming continuous data stream. In addition, more sophisticated processes like copying or resorting of individual data can be realized in derived classes. Derived from this base class I implemented some executable burst builder for the following studies.

Event Based

The implemented event based version does not expect a realistic continuous input data stream, but an event wise input from the standard Monte Carlo simulation. It combines a specified number of events into event packages. This is useful to study the influence of the fixable package size on the reconstruction algorithms. This implementation also works with detector implementations which are not capable of running in a time based mode yet. The following code shows how to activate this class in the macro controlling the reconstruction stage of PandaRoot.

```
1  PndBranchBurstBuilder_eventBased* combine = new
    PndBranchBurstBuilder_eventBased();
    combine->AddInputBranch("STTPoint"); //define the subdetector
    signals which are taken into account
3  combine->AddInputBranch("SciTPoint");
    combine->SetNEvents(3); // set the event package size
5  combine->SetOutputPrefix("burst_eb3");// set a prefix for the
    output
    combine->SetPersistence(kTRUE); // define wether the data
    should be stored in the output file , or is only temporary
    accessible
7  fRun->AddTask(combi3);
```


Time Based

Another implemented version can deal with continuously streamed input data. For that purpose it exploits the \bar{p} beam structure of the HESR. Due to technical reasons the HESR will be filled with antiprotons up to 80%. The revolution time for the stored \bar{p} is in the order of 2000 ns, depending slightly on the used beam momentum. Therefore the incoming signals will be structured in about 1600 ns long packages with a 400 ns gap in between. Depending on the time resolution of the sub detector systems the gap in the individual signal lines may decrease. However, even for systems with a less accurate time measurement or a big variation in the response time a 400 ns gap between $\bar{p}p$ annihilations will prevent an event mixing. Cutting the data stream at the beginning of a new cycle is therefore a safe way to generate event packages without separating important data. The listing below shows the activation code for the reconstruction macros.

```
1 PndBranchBurstBuilder_tb* burst = new PndBranchBurstBuilder_tb();
  burst->AddInputBranch("SciTHit"); // define the subdetector signals
  which are taken into account
3 burst->SetOutputPrefix("burst"); // set a prefix for the output
  burst->SetTimePeriod(2000); // set the revolution time
5 burst->SetPersistence(kTRUE); // define whether the data should
  be stored in the output file, or is only temporary accessible
fRun->AddTask(burst);
```

7.1.2 STTCellTrackFinder

To perform a track reconstruction on the continuous data stream, a suitable track reconstruction algorithm called STTCellTrackFinder was updated. This algorithm is based on a cellular automaton (CA) algorithm [41]. It uses neighborhood relations and boundary values to find track seeds, called tracklets. In a following step these tracklets are combined into tracks using a Riemann fit [42]. The original implementation of this track reconstruction algorithm was written for event based processing. I however updated the interface in a way that the STTCellTrackFinder is able to process event packages of any size.

7.2 First Time Based Track Reconstruction

Combining the time based simulation, the implemented time based PndBrach-BurstBuilder, and the updated version of the STTCellTrackFinder I was able to perform the first track reconstruction on the continuous data stream of the simulated $\bar{\text{PANDA}}$ detector. I simulated 10^4 $\bar{\text{p}}\text{p}$ annihilation events using the DPM generator at a primary momentum of 7 GeV/c. The digitization was executed in the event based and the time based mode, for an average event rate of 2 and 20 MHz. In both time based cases the revolution time was 2000 ns with a 400 ns gap. The event based data was used to build data packages of 2 up to 60 events. I compared the processing time and the reconstructed track number for the two time based simulations and these event packages with the output of the standard pure event based simulation.

Unfortunately, the time based reconstruction was still in early stages of development at that time. Specialized tools to quantitatively evaluate the reconstruction existed only for the event based simulation. Nevertheless these first studies allowed the investigation of interesting parameters. First checks showed that the reconstruction of even very big event packages was working in principle. Figure 7.1 summarizes this first study. The needed total processing time of all generated event packages and the total number of reconstructed tracks as a function of the event package size.

On the one side the processing times for the individual event packages increase, on the other side the total number of event packages decreases with their size. However, looking on the first part of figure 7.1 up to event package sizes of 20, it indicates that also the total processing time for the reconstruction of 10^4 events increases. This total processing time is marked by blue crosses. This increased processing time is crucial for the online reconstruction. Although less packages must be processed the possible combinatorics within one package seems to increase drastically. More tracklets are found and all of them are checked for accordance with each other to constitute a track. Not only these initial combinatorics, but also the amount of finally found tracks increase as indicated by the orange crosses in figure 7.1. Since the amount of simulated tracks was constant for all tests, these additional reconstructed tracks are ghost tracks. Due to the increased amount of signals more wrong combinations are found, which are indistinguishable from real tracks for this reconstruction algorithm. This effect also contributes to the increased processing time and shows that in addition more sophisticated methods to suppress such ghost tracks are necessary. Otherwise the reconstruction stage may be slowed down or the further data processing could be affected by these

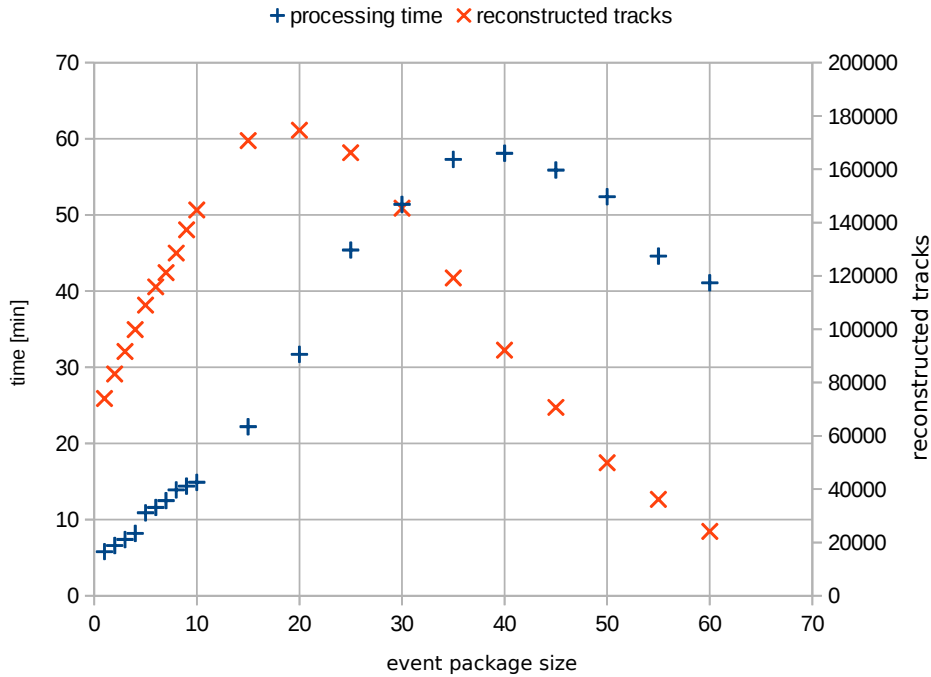


Figure 7.1: The needed computing time(blue +) and the total amount of reconstructed tracks (orange x) as a function of the event package size are plotted. Up to an event package size of 20 the processing time as well as the amount of found tracks increases. For bigger event packages the found tracks and the processing time decreases again.

ghost tracks.

Increasing the event package size further up to 60 events per package inverts the discussed effect (cf. figure 7.1). At a package size of 20 events the signals of the included tracks seems not separated enough anymore. Therefore the reconstruction algorithms can not find as many separated tracklets as before and the number of combined, reconstructed tracks decreases again. At that point we can not study whether ghost tracks or MC true tracks are lost. However we have to assume that also a significant amount of real tracks can not be reconstructed above that threshold. After increasing the event package size further the processing time also decreases, due to the reduced possible combinatorics. Nevertheless it never returns to values comparable to small package sizes.

Finally as mentioned also a time based simulation was evaluated, exploiting the revolution time of the \bar{p} beam. The number of reconstructed tracks and the pro-

cessing time for the time based data is comparable to the results of previous study. Figure 7.2 summarizes the results of the time based simulation and the event based packages in one plot. The data points for the time based simulation, marked by the circles, are set at the average event package size for 2 and 20 MHz average event rate. The number of actual events included in an individual package varies for the time based simulation. Therefore the needed processing time and reconstructed track number differ slightly from the previous results. This difference gets more significant for higher event rates due to the higher fluctuation. These results show, that for an average event rate of 2 MHz a simple approach like exploiting the revolution time of the \bar{p} beam may already simplify the problem significantly. Although the processing time increases, it stays comparable to the event based reconstruction. Additional ghost tracks are reconstructed in comparison to an event based reconstruction. However, at first appearance no loss of real track information is obviously recorded. This is not true anymore for an average event rate of 20 MHz. The processing time increases significantly and it indicates that real tracks may be lost while the ratio of reconstructed ghost tracks increases.

Currently, work is ongoing to improve the reconstruction algorithm to overcome these problems [43]. So far it only takes into account neighborhood relations in space. In the next step the individual timing information of the signals will be used as an additional dimension. Although the timing information is not precise enough at this stage to allow a sorting of the data event by event, it will reduce the possible combinatorics and adjacencies significantly. The determination of possible annihilation times t_0 using the Barrel TOF detector and the developed algorithms discussed in chapter 6 can also provide additional information before the track reconstruction to reduce the combinatorics.

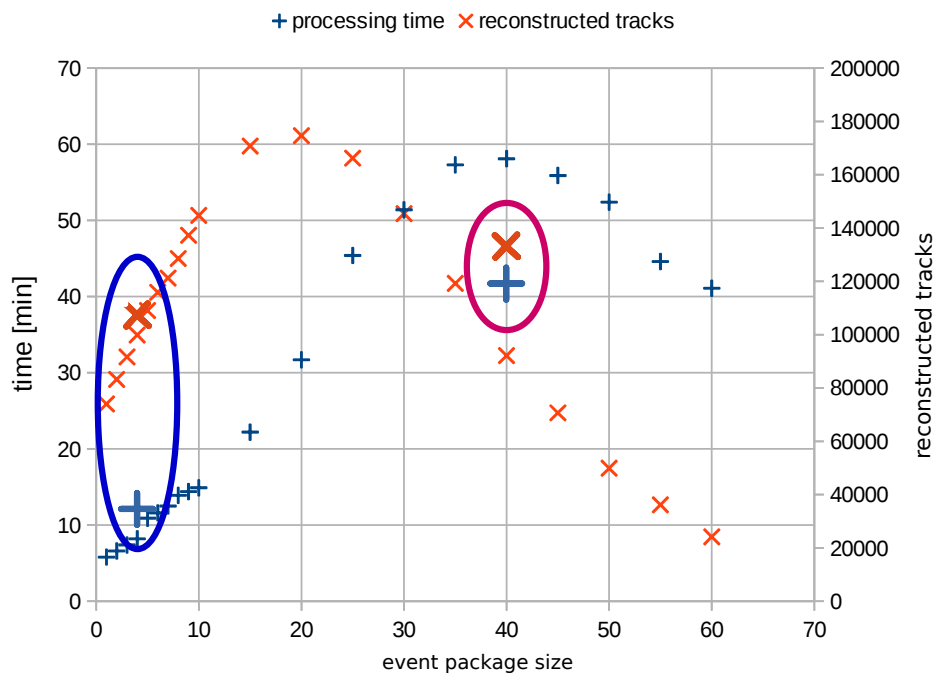


Figure 7.2: In comparison to figure 7.1 also the results for the time based simulation are presented. The big marks in the blue circle indicate the results for an average $\bar{p}p$ annihilation rate of 2 MHz, the marks in the pink circle for 20 MHz

8 Summary and Outlook

\bar{P} ANDA is one of the future new generation experiments in particle physics. It addresses open questions of the weak and strong forces, exotic states of matter and the structure of hadrons via $\bar{p}p$ and \bar{p} -nucleon interactions. \bar{P} ANDA will perform a novel approach of data acquisition. Instead of a common hardware trigger a fully software based system will be used. The Barrel Time-of-Flight detector will be an important system for such a DAQ scheme, due to its very precise and reliable time measurement. The Barrel TOF is mainly composed of scintillating tiles which cover about 5 m^2 in the central region and are readout by Silicon Photomultipliers.

The focus of this work was first on the implementation of the detector system into the software framework of \bar{P} ANDA, called PandaRoot and to perform simulations to evaluate two design options for the Barrel TOF. Therefore I described these two geometries as well as two reference geometries using the geometry classes of ROOT. The two design options mainly distinguish in the shape and size of the scintillating tiles which are $28.5 \times 28.5 \times 5 \text{ mm}^3$ for the original proposed design and $87.0 \times 29.4 \times 5 \text{ mm}^3$ for the final design, respectively. The latter design allows a reduction of readout channels, a simpler mechanical structure and therefore a reduced material budget. Last but not least it allowed an improved time resolution realized with a comparable number of photosensors. However it has disadvantages in the scintillator tile distribution. The reference geometries describe a perfect cylinder and a detector composed of perfect super-modules, representing idealized condition. 16 segmentations of the barrel and the maximum outer dimension of each super-module is a predefined boundary condition for this R&D work, to not interfere with other systems. Although the design of FEE is not yet final, a data acquisition was implemented to the best knowledge as of now. A time resolution of 75 ps in standard deviation was set in the simulations. This is slightly above the latest test beam results of 54 ps time resolution to ensure conservative limits in the performance simulations. Also the event mixing and signal pile up at high interaction rates was implemented in the simulation of the electronics to allow the development and tests of, event sorting, online reconstruction algorithms and trigger.

The simulation studies showed that the two design options had a similar total detection efficiency, including geometrical acceptance and DAQ efficiency, of 91% in comparison to the perfect reference detector. These studies confirmed that the final design has no drawbacks in terms of the detection efficiency. Furthermore the final design had an efficiency less dependent from conditions, such as for primary \bar{p} -beam momenta and final state particle emission angles.

In the second part of this thesis algorithms for the event sorting, the t_0 determination and PID were developed, implemented in PandaRoot and evaluated. All these algorithms are based mainly on the information provided by the Barrel TOF. The evaluation of a developed event sorting algorithm based on the Barrel TOF and the FTOF showed that up to 93% of simulated background events are correctly determined. Furthermore the $\bar{p}p$ annihilation time is predicted with a precision of 0.55 ns for these events. Although backscattered secondary particles induce a significant amount of uninterested hits, these particles do not affect the detection of other events.

The t_0 estimation can be improved further after the sorting of the data in the respective events. For that purpose pre-calibrated average time-of-flight values for all detector segments are taken into account. In comparison to the mentioned event sorting algorithm, so far only the Barrel TOF information was included in this algorithm. Nevertheless it was possible to improve the t_0 time resolution below 0.5 ns, although no tracking or PID information was used. Including also the FTOF system will further improve the performance. These results showed that the TOF counters of $\bar{P}ANDA$ will be able to provide decent t_0 information, even before the tracking and PID stage. This is important to provide this essential information to the track reconstruction algorithms.

Another important use case of the Barrel TOF is the PID, especially below the Cherenkov threshold of about 700 MeV/c. Since $\bar{P}ANDA$ has no dedicated start time detector, a standard time-of-flight based PID is hard to realize. In order to overcome this challenge a relative time-of-flight based algorithm was adapted for the $\bar{P}ANDA$ experiments and included in PandaRoot. This algorithm relies on a proper event sorting and good track reconstruction. It iterates through all possible particle hypotheses and determines the most probable t_0 and mass configuration through a χ^2 minimization. The χ^2 values provide also a probability weight which can be used to derive a probability density function for the respective particle hypotheses. This algorithm shows an improvement of its performance for an increased number of reconstructed tracks hitting the TOF detectors. It was possible to determine the t_0 time with a precision of $\sigma = 57$ ps for events with 3 or more primary particles hitting the Barrel TOF. Although it should be noted that

this signal multiplicity is only achieved for about 35% of the events. Therefore covering a larger acceptance with the FTOF detector is very important to increase the signal multiplicity.

Also a standard time-of-flight based PID algorithm was implemented in PandaRoot. However, due to the missing counterpart for the time-of-flight measurement in $\bar{\text{PANDA}}$, an already reconstructed t_0 is assumed by this implemented algorithms. The time-of-flight resolution of the whole tracking system was evaluated for the various particle species and track parameters. The study showed that this resolution is a function of the transverse momentum of the particles. Although the resolution is constant for momenta above a particle specific threshold, it rapidly becomes worse below. Taking this into account a separation power as a function of the transverse momentum was calculated for the evaluated particle species. It was shown that the separation power stays above 2σ for π/K and above 5σ for K/p separation up to 1 GeV/c transverse momentum. With decreased transverse momentum, especially below the Cherenkov threshold, the separation power increases strongly up to 15σ and 25σ , respectively. The ongoing work on the track reconstruction algorithms and the t_0 determination will have an influence on the provided PID performance. Once this developments converge the implemented time-of-flight PID algorithm will be updated and optimized.

In the last part of the thesis the focus was on the online reconstruction of the continuous data stream of the experiment. For this purpose a new class was implemented into PandaRoot that cuts and packs the continuous data stream into individual packages. The already existing reconstruction software can handle these packages with just minor adaptations. The revolution time of the \bar{p} beam in the HESR was exploited, to cut the stream advantageous positions. In addition, classes were implemented to combine the output of a basic event based simulation into such packages of events for testing purpose. Also one reconstruction algorithm called STTCellTrackFinder, which is based on a cellular automaton algorithms was updated for this packages. Putting this together, the first time based reconstruction was performed. The results showed that the chosen reconstruction algorithm was able to reconstruct packages containing up to 60 events. However the reconstruction time increases strongly up to a factor of 12. Above a package size of 20 events also the reconstruction efficiency drops significantly. with the current state of PandaRoot a quantitative evaluation was not yet possible. Both issues must be addressed in future. since they are crucial for the DAQ of $\bar{\text{PANDA}}$. Nevertheless this study already showed the proof of principle. In the next step the STTCellTrackFinder will be upgraded to include also the timing information of the used signals. For this the Barrel TOF can play an important role.

The studies discussed in this thesis are also part of the Technical Design Report

of the Barrel TOF, which was submitted in February 2017 to FAIR and accepted.

List of Tables

5.1	Studied Barrel TOF design	50
5.2	Results of the efficiency studies	58
6.1	Event determination results	77
6.2	TOF resolution fit parameters	97

List of Figures

2.1	FAIR complex	8
2.2	HESR	10
2.3	The \bar{P} ANDA Spectrometer	11
2.4	Target system and MVD	12
2.5	Magnet system	13
2.6	STT system	15
2.7	GEM system	16
2.8	FTS system	17
2.9	DIRC system	18
2.10	TOF system	19
2.11	Muon system and EMC	20
2.12	Online reconstruction scheme	22
3.1	Structure of PandaRoot	24
4.1	The Barrel TOF	32
4.2	Event spacing in \bar{P} ANDA	34
4.3	Preshower event	35
4.4	Required event sorting	36
4.5	Event sorting efficiency	37
4.6	Segmentation of the Barrel TOF	39
4.7	Super-module design	39
4.8	Scintillator tile module	40
4.9	Scintillator tile mounted on a super-module	41
4.10	Per Tile hit rate in the Barrel TOF	42
5.1	Reference Geometries in PandaRoot	44
5.2	Original Barrel TOF design in PandaRoot	45
5.3	Final Barrel TOF design in PandaRoot	45
5.4	Time stamp distribution for the event based mode	49
5.5	Time stamp distribution for the time based mode	49
5.6	Geometrical efficiency of the Barrel TOF	51
5.7	Geometrical efficiency of the Barrel TOF	53

5.8	Insensitive gaps in the super-module designs	54
5.9	DAQ efficiency	56
5.10	DAQ efficiency	57
6.1	Signal time distribution for target spectrometer detectors	60
6.2	Time based timestamp distribution from the TOF counters	61
6.3	Event based timestamp distribution from the Barrel TOF	62
6.4	Event display for back coming neutrons	64
6.5	Event display for back coming photon	65
6.6	Event display for back coming π^-	65
6.7	Event display for a long interaction or decay chain	66
6.8	Breakdown of the timestamp distribution from the Barrel TOF	67
6.9	Integrated time stamp distribution in the Barrel TOF	68
6.10	Speed-of-light corrected timestamp distribution in the Barrel TOF	70
6.11	Particle multiplicity in the TOF counters	71
6.12	Scheme of the event sorting algorithm	72
6.13	Results for the event sorting	74
6.14	T_0 distribution for the event sorting	75
6.15	Timestamp distribution in the MVD	76
6.16	Timestamp correction	78
6.17	Timestamp distribution of Barrel TOF signals	79
6.18	Barrel TOF signals as a function of the Hit position	80
6.19	Timestamp distribution in a single Barrel TOF slice	81
6.20	Typical time-of-flights for the Barrel TOF	82
6.21	Energy deposit as a function of the time-of-flight	83
6.22	Corrected timestamp distribution of the Barrel TOF	84
6.23	Estimated t_0 distribution	85
6.24	Influence of the particle multiplicity	86
6.25	Relative Time-of-Flight principle	88
6.26	Relative TOF t_0 distribution	90
6.27	Relative TOF t_0 distribution	91
6.28	Basic concept op TOF based PID	94
6.29	Cut on poorly reconstructed tracks	95
6.30	TOF resolution for 1.5+GeV/c π^-	96
6.31	TOF resolution as a function of p , p_t , track length and hit position	97
6.32	TOF resolution as a function of p_t	98
6.33	TOF resolution as a function of p_t	99
6.34	Separation power of the Barrel TOF	101
7.1	Event package reconstruction	107
7.2	Time based reconstruction	109

Bibliography

- [1] K. Goetzen et al. “Proposal for a Scintillator Tile Hodoscope for $\bar{\text{P}}\text{ANDA}$ ”. 2012. URL: <https://panda-wiki.gsi.de/foswiki/pub/Tof/SciTil/scitil.pdf>.
- [2] M. F. M. Lutz et al. “Physics Performance Report for PANDA: Strong Interaction Studies with Antiprotons”. In: (2009). arXiv: 0903.3905 [hep-ex].
- [3] P. Spiller and G. Franchetti. “The FAIR accelerator project at GSI”. In: *Nuclear Instruments and Methods in Physics Research Section A: Accelerators, Spectrometers, Detectors and Associated Equipment* 561.2 (2006), pp. 305–309. ISSN: 0168-9002. DOI: <https://doi.org/10.1016/j.nima.2006.01.043>.
- [4] W F Henning. “FAIR and its experimental program”. In: *Journal of Physics G: Nuclear and Particle Physics* 34.8 (2007), S551.
- [5] D. Prasuhn. “Status HESR”. In: PANDA meeting. June 2014.
- [6] PANDA Collaboration et al. “Technical Design Report, FAIR Antiproton Target and Separator”. In: *FAIR/GSI* (2008).
- [7] PANDA Collaboration. “Technical Design Report for the $\bar{\text{P}}\text{ANDA}$ Internal Targets: The Cluster-Jet Target and Developments for the Pellet Target”. 2012. URL: https://panda.gsi.de/oldwww/archive/TargetTDR/Targets_TDR.pdf.
- [8] URL: <https://panda.gsi.de/>.
- [9] W. Erni et al. “Technical Design Report for the PANDA Solenoid and Dipole Spectrometer Magnets”. In: (2009). arXiv: 0907.0169 [physics.ins-det].
- [10] W Erni et al. *Technical Design Report for the: PANDA Micro Vertex Detector*. Tech. rep. arXiv:1207.6581. Comments: 189 pages, 225 figures, 41 tables. July 2012. URL: <http://cds.cern.ch/record/1470881>.
- [11] PANDA Collaboration et al. *Technical Design Report for the: PANDA Straw Tube Tracker*. Tech. rep. tech. rep., PANDA Collaboration, 2012.
- [12] PANDA Collaboration. *Technical Design Report for the: PANDA Barrel Dirc Detector*. Tech. rep. tech. rep., PANDA Collaboration, 2017.

- [13] PANDA Collaboration. “Technical Design Report for the: \bar{P} ANDA Barrel Time-of-Flight”. 2017.
- [14] PANDA Collaboration. *Technical Design Report for the: PANDA Moun System*. Tech. rep. tech. rep., PANDA Collaboration, 2012.
- [15] PANDA Collaboration. “Technical Design Report for PANDA Electromagnetic Calorimeter (EMC)”. In: (2008). arXiv: 0810.1216 [physics.ins-det].
- [16] M Kotulla et al. *PANDA Technical Progress Report*. 2005.
- [17] D. Steinschaden and \bar{P} ANDA Collaboration. “Event Reconstruction and Simulation in PandaRoot for the \bar{P} ANDA Experiment”. 2017.
- [18] S. Spataro for the PANDA collaboration. “The PandaRoot framework for simulation, reconstruction and analysis”. In: *Journal of Physics: Conference Series* 331 (2011).
- [19] Stefano Spataro. “Event Reconstruction in the PandaRoot framework”. In: *Journal of Physics: Conference Series* 396.2 (2012), p. 022048.
- [20] M. Al-Turany et al. “The FairRoot framework”. In: *Journal of Physics: Conference Series* 396.2 (2012), p. 022001.
- [21] F. Rademakers B. Rene. “ROOT — An object oriented data analysis framework”. In: *Nucl. Intr. Meth. A* 389 (1997), pp. 81–86.
- [22] I. Hrivnacova et al. “The Virtual Monte Carlo”. In: *CoRR* cs.SE/0306005 (2003).
- [23] M.Al-Turany. “FairRoot framework”. In: Talk at HIC for FAIR Workshop. Feb. 2010.
- [24] URL: <https://root.cern.ch>.
- [25] Rene Brun and Fons Rademakers. “ROOT—an object oriented data analysis framework”. In: *Nuclear Instruments and Methods in Physics Research Section A: Accelerators, Spectrometers, Detectors and Associated Equipment* 389.1-2 (1997), pp. 81–86.
- [26] David J. Lange. “The EvtGen particle decay simulation package”. In: *Nuclear Instruments and Methods in Physics Research Section A: Accelerators, Spectrometers, Detectors and Associated Equipment* 462.1 (2001), pp. 152–155. ISSN: 0168-9002. DOI: [https://doi.org/10.1016/S0168-9002\(01\)00089-4](https://doi.org/10.1016/S0168-9002(01)00089-4).
- [27] A. Capella et al. “Dual parton model”. In: *Physics Reports* 236.4 (1994), pp. 225–329. ISSN: 0370-1573. DOI: [https://doi.org/10.1016/0370-1573\(94\)90064-7](https://doi.org/10.1016/0370-1573(94)90064-7).

- [28] M Bleicher et al. “Relativistic hadron-hadron collisions in the ultra-relativistic quantum molecular dynamics model”. In: *Journal of Physics G: Nuclear and Particle Physics* 25.9 (1999), p. 1859.
- [29] Torbjörn Sjöstrand, Stephen Mrenna, and Peter Skands. “A brief introduction to PYTHIA 8.1”. In: *Computer Physics Communications* 178.11 (2008), pp. 852–867. ISSN: 0010-4655. DOI: <https://doi.org/10.1016/j.cpc.2008.01.036>.
- [30] S. Agostinelli. “Geant4—a simulation toolkit”. In: *Nucl. Inst. and Meth. A* 506.3 (July 2003), pp. 250–303. DOI: 10.1016/S0168-9002(03)01368-8.
- [31] Rene Brun et al. *GEANT: Detector description and simulation tool*. Tech. rep. CERN, 1993.
- [32] URL: <http://evtgen.hepforge.org/> (visited on 04/10/2018).
- [33] D. Boutigny et al. “BaBar technical design report”. In: *BaBar Technical Design Report EPAC Meeting Stanford, California, March 17-18, 1995*. 1995. URL: <http://www.slac.stanford.edu/BFROOT/doc/TDR>.
- [34] G. Schepers et al. *Particle Identification at PANDA - Report of the PID TAG*. Tech. rep. PANDA Note, March 2009. URL: <http://www-panda.gsi.de/db/notesDBr/GS14-090310%20pid-tag.pdf>.
- [35] K. Götzten. *Influence of Particle Timing on Event Building*. March 2011. URL: <http://www-panda.gsi.de/db/notesDBr/KG13-110311%20KGoetzen%20EventMixingAtPanda.pdf>.
- [36] K. Goetzen et al. “Motivation of the Barrel Time-of-Flight Detector for \bar{P} ANDA”. \bar{P} ANDA Note. 2011. URL: <https://panda-wiki.gsi.de/cgi-bin/view/Tof/TimingBarrel>.
- [37] S. Zimmermann et al. “ \bar{P} ANDA Barrel-TOF Detector at FAIR”. In: *Journal of Instrumentation* 12.08 (2017), p. C08017. URL: <http://stacks.iop.org/1748-0221/12/i=08/a=C08017>.
- [38] T. Stockmanns. “privat communication”. 2017.
- [39] M. Basile et al. “A large-area time-of-flight system for a colliding beam machine”. In: *Nuclear Instruments and Methods* 179.3 (1981), pp. 477–485. ISSN: 0029-554X. DOI: [https://doi.org/10.1016/0029-554X\(81\)90171-3](https://doi.org/10.1016/0029-554X(81)90171-3). URL: <http://www.sciencedirect.com/science/article/pii/0029554X81901713>.
- [40] A. Akindinov et al. “Performance of the ALICE Time-Of-Flight detector at the LHC”. In: *The European Physical Journal Plus* 128.4 (Apr. 2013), p. 44. ISSN: 2190-5444. DOI: 10.1140/epjp/i2013-13044-x. URL: <https://doi.org/10.1140/epjp/i2013-13044-x>.

- [41] Stephen Wolfram. “Statistical mechanics of cellular automata”. In: *Rev. Mod. Phys.* 55 (3 July 1983), pp. 601–644. DOI: 10.1103/RevModPhys.55.601. URL: <https://link.aps.org/doi/10.1103/RevModPhys.55.601>.
- [42] R. Frühwirth, A. Strandlie, and W. Waltenberger. “Helix fitting by an extended Riemann fit”. In: *Nuclear Instruments and Methods in Physics Research Section A: Accelerators, Spectrometers, Detectors and Associated Equipment* 490.1 (2002), pp. 366–378. ISSN: 0168-9002. DOI: [https://doi.org/10.1016/S0168-9002\(02\)00911-7](https://doi.org/10.1016/S0168-9002(02)00911-7). URL: <http://www.sciencedirect.com/science/article/pii/S0168900202009117>.
- [43] J. Regina. *PhD project*.

Dominik Steinschaden

Guntherstraße 13/17

1150 Vienna

Tel.: +43676 6962349

dominik.steinschaden@gmail.com

RESEARCH EXPERIENCE

PhD student

Jun 2014 - Jun 2018

Stefan Meyer Institute, Austrian Academy of Science

Thesis title: [Optimization Studies and Performance Simulations for the Time-of-Flight System of PANDA](#)

Supervisor: Priv.-Doz Dr. Johann Marton

- Designing and developing the Barrel-TOF detector for the PANDA experiment
- Operation of precise timing detectors under strict requirements
- Particle detection, identification and data analysis in high energy physics
- Simulation studies for performance optimization using Geant4, Root and Virtual Monte Carlo within the framework "PandaRoot"
- Development of a dynamical tracking and event reconstruction algorithm for PANDA
- Extension of Monte Carlo based simulation frameworks

PhD internship

Feb 2017 - Jul 2017

Department of Physics and Astronomy, Uppsala University, Sweden

- Hyperon physics and data analysis
- Development of a dynamical tracking and event reconstruction algorithm for PANDA

Master internship

Jan 2013 - Oct 2013

Stefan Meyer Institute, Austrian Academy of Science

Thesis title: [Investigation of the prompt gamma ray emission for on-line monitoring in ion therapy](#)

Supervisor: Priv.-Doz Dr. Johann Marton

- Studies of dose delivery, Bragg peak position and connected parameters of prompt gamma rays
- Studies on photon scattering, absorption and detection
- Monte Carlo simulations with GATE (Geant4 Application for Tomographic Emission)

Internship student

May 2011 - Jul 2011

Institute of Atomic Physics, TU Vienna

- Experiments in low temperature physics
- Studies on high temperature super conductors

Internship student

Sep 2010

Max Planck Institute for Plasma Physics (Munich)

- Nuclear fusion studies at the ASDEX Upgrade
- Divertor Physics and Tokamak Edge Field
- Analysis of plasma-wall interaction products in the ASDEX Upgrade

EDUCATION

Member of the DkPI Doktoratskolleg for Particles and Interactions	Jun 2014 - June 2018
PhD in Technical Physics Technical University of Vienna	Jun 2014 - June 2018
Master in Technical Physics Technical University of Vienna	Mar 2011 - Mar 2014
Bachelor in Technical Physics Technical University of Vienna	Mar 2007 - Mar 2011
Secondary and high school Bundesrealgymnasium Krems	Sep 1998 - Jun 2006

- Austrian secondary education school type with emphasis on science

SKILLS

Technical Competences:	Particle and photon detection Fast timing with silicon photo multiplier (SiPM) and scintillators Trigger, tracking and reconstruction systems for particles Machine Learning: Multilayer Perceptron, Support Vector Machines
Software Experience:	Charged particle and photon propagation: Geant4, GATE, Litrani, Virtual Monte Carlo Data analysis: ROOT, MATLAB, Python Programming IDE: Eclipse, LabVIEW Text processing: Latex, Libre Office, PDF Editors, Microsoft Office Operating systems: Linux, Microsoft Windows, Solaris
Programming Languages:	C++, Python, MATLAB, LabVIEW, Latex, bash script, Fortran
Soft Skills:	Project management Independent acquire of knowledge and working Working well in teams, ability to represent teams and collaborations Supervision of undergraduate and graduate students

LANGUAGES

German	Native speaker
English	Fluent , daily work performed in English
Italian	Basic , high school certificate

PEER-REVIEWED JOURNAL PAPERS

1. D. Steinschaden, S. E. Brunner, H. Dichtl, H. Fuchs, D. Georg, A. Hirrtl, J. Marton and A. Pichler
Investigation of prompt γ ray emission for online monitoring in ion therapy,
J. Phys. Conf. Ser. **599** (2015) no.1, 012042. doi:10.1088/1742-6596/599/1/012042
2. K. Dutta, K. Kalita, K. Suzuki, D. Steinschaden and B. J. Roy,
Study of Preshower in the PANDA Target Spectrometer,
DAE Symp. Nucl. Phys. **60** (2015) 1044.
3. D. Steinschaden et al.,
The Barrel TOF detector for PANDA,
PoS EPS -HEP2015 (2015) 259.
4. B. Singh et al. [PANDA Collaboration],
Feasibility studies of time-like proton electromagnetic form factors at \bar{P} ANDA at FAIR,
Eur. Phys. J. A **52** (2016) no.10, 325 doi:10.1140/epja/i2016-16325-5 [arXiv:1606.01118 [hep-ex]].
5. B. Singh et al. [PANDA Collaboration],
Feasibility study for the measurement of πN transition distribution amplitudes at \bar{P} ANDA in $\bar{p}p \rightarrow J/\psi\pi^0$,
Phys. Rev. D **95** (2017) no.3, 032003 doi:10.1103/PhysRevD.95.032003 [arXiv:1610.02149 [nucl-ex]].
6. B. Singh et al. [PANDA Collaboration]
Technical Design Report for the Panda Forward Spectrometer Calorimeter,
arXiv:1704.02713 [physics.ins-det].
7. S. Zimmermann and K. Suzuki and D. Steinschaden and M. Chirita and G. Ahmed and K. Dutta and K. Kalita and A. Lehmann and M. Böhm and K. Schwarz and H. Orth and K.-Th. Brinkmann
The PANDA Barrel-TOF Detector at FAIR,
Journal of Instrumentation/12/08 - C08017, 2017
8. D. Steinschaden, on behalf of the PANDA Collaboration
Event Reconstruction and Simulation in PandaRoot for the PANDA Experiment,
J. Phys. Conf. Ser. unpublished

PRESENTATIONS AT INTERNATIONAL CONFERENCES

1. Investigation of prompt gamma ray emission for online monitoring in ion therapy, FAIRNESS, Vietri sul Mare 19/2014
2. Barrel time-of-flight detector for PANDA at FAIR, EPS-HEP 2015, Vienna 6/2015
3. PID based on relative time of flight methodes, LVII PANDA Collaboration Meeting, Mainz/ Germany 9/2016
4. Performance simulation of the Barrel Scintillator Tile Hodoscope for PANDA, Oepg Jahrestagung 2016, Vienna/Austria 9/2016
5. Event Sorting based on TOF Counter, LVIII PANDA Collaboration Meeting, GSI Darmstadt / Germany 12/2016
6. The Barrel Time-of-Flight detector of PANDA, HEP seminar, Uppsala/ Sweden 12/2016
7. Event Reconstruction and Simulation in PandaRoot for the PANDA Experiment, ACAT2017, Seattle/ USA 8/2017